Alma Mater Studiorum - Università di Bologna

# DOTTORATO DI RICERCA IN IL FUTURO DELLA TERRA, CAMBIAMENTI CLIMATICI E SFIDE SOCIALI

Ciclo 35

**Settore Concorsuale:** 02/C1 - ASTRONOMIA, ASTROFISICA, FISICA DELLA TERRA E DEI PIANETI

**Settore Scientifico Disciplinare:** FIS/06 - FISICA PER IL SISTEMA TERRA E IL MEZZO CIRCUMTERRESTRE

# RETRIEVAL OF ATMOSPHERIC TRACE GASES FROM DOAS/MAX-DOAS GROUND-BASED SPECTRA

**Presentata da:** Paolo Pettinari

**Coordinatore Dottorato**

Silvana Di Sabatino

**Supervisore**

Bianca Maria Dinelli

**Co-supervisore**

Tiziano Maestri

Elisa Castelli

**Esame finale anno 2023**

# Contents

# Acronyms

| | |
|---|---|
| ACE-FTS | Atmospheric Chemistry Experiment - Fourier Transform Spectrometer. |
| ACTRIS | Aerosol, Clouds and Trace Gases Research Infrastructure. |
| AKs | Averaging Kernels. |
| AMFs | Air Mass Factors. |
| ARPAE | Agenzia regionale per la prevenzione, l'ambiente e l'energia dell'Emilia-Romagna. |
| BAQUNIN | Boundary-layer Air Quality-analysis Using Network of Instruments. |
| BIRA-IASB | Royal Belgian Institute for Space Aeronomy. |
| BOREAS | Bremen Optimal estimation REtrieval for Aerosols and trace gaseS. |
| CCD | Charge-Coupled Device. |
| CF | Cloud Fraction. |
| CFCs | ChloroFluoroCarbons. |
| CINDI-2 | Cabaw Intercomparison of Nitrogen Dioxide measuring Instruments - 2. |
| CNR-ISAC | Consiglio Nazionale delle Ricerche - Istituto di Scienze dell' Atmosfera e del Clima. |
| CTM | Chemical Transport Model. |
| DOAS | Differential Optical Absorption Spectroscopy. |
| DOFs | Degrees Of Freedom. |
| ECO | Environmental Climate Observatory. |

| | |
|---|---|
| ENVISAT | ENVIronmental SATellite. |
| EO | Earth Observation. |
| EOS | Earth Observing Satellite. |
| ESA | European Space Agency. |
| FOV | Field Of View. |
| FRM4DOAS | Fiducial Reference Measurements for DOAS. |
| FTIR | Fourier Transform Infra-Red. |
| FWHM | Full Width at Half Maximum. |
| GASCOD/NG4 | Gas Analyser Spectrometer Correlating Optical Differences / New Generation 4. |
| GAW | Global Atmospheric Watch. |
| GPS | Global Positioning System. |
| Hg | Mercury. |
| I-AMICA | Infrastruttura di Alta tecnologia per il Monitoraggio Integrato Climatico-Ambientale. |
| IDEAS | Instrument Data Evaluation and Analysis Service. |
| IR | Infra-Red. |
| IUP | Institute of Environmental Physics. |
| LIDAR | LIgth Detection And Ranging. |
| LOS | Line Of Sight. |
| MAX-DOAS | Multi-AXis-DOAS. |
| MINDS | Multi-Decadal Nitrogen Dioxide and Derived Products from Satellites. |
| MIPAS | Michelson Interferometer for Passive Atmospheric Sounding. |
| MS-DOAS | Measurement Software-DOAS. |
| NASA | National Aeronautics and Space Administration. |

| | |
|---|---|
| NetCDF | Network Common Data Form. |
| OE | Optimal Estimation. |
| OMI | Ozone Monitoring Instrument. |
| PGN | Pandonia Global Network. |
| QA | Quality Assurance. |
| QA4EO | Quality Assurance for Earth Observation. |
| RADAR | RAdio Detection And Ranging. |
| RTM | Radiative Transfer Model. |
| S-5P | Sentinel-5 Precursor. |
| SCDs | Slant Column Densities. |
| SNR | Signal to Noise Ratio. |
| SPC | San Pietro Capofiume. |
| SZA | Solar Zenith Angle. |
| TM5-MP | Tracer Model version 5 - Massively Parallel. |
| TROPOGAS | TROPOspheric Gas Analyser Spectrometer. |
| TROPOMI | TROPospheric Ozone Monitoring Instrument. |
| USB | Universal Serial Bus. |
| UV | Ultra-Violet. |
| VCDs | Vertical Column Densities. |
| VIS | Visible. |

# Overview

The ground-based Differential Optical Absorption Spectroscopy (DOAS) technique is used to derive trace gases information from remote-sensing measurements of Visible (VIS) and Ultra-Violet (UV) diffuse solar spectra.

The Consiglio Nazionale delle Ricerche - Istituto di Scienze dell'Atmosfera e del Clima (CNR-ISAC), where I performed my PhD work, has several DOAS instruments: SkySpec-2D which is a new standard one, and several old custom-built systems. During my PhD, I worked on two of the mentioned custom-built instruments: the TROPOspheric Gas Analyser System (TROPOGAS), installed on the roof of the CNR-ISAC in Bologna since 2018, and the Gas Analyser Spectrometer Correlating Optical Differences / New Generation 4 (GASCOD/NG4), installed at the Environmental Climate Observatory (ECO) of the CNR-ISAC in Lecce since 2016. Moreover, I also worked on the new instrument SkySpec-2D, installed at the Giorgio Fea observatory in San Pietro Capofiume (SPC) since 1 October 2021.

In the first part of the PhD, I analyzed the zenith-sky spectra acquired by GASCOD/NG4 at ECO site in order to retrieve $NO_2$ and $O_3$ Vertical Column Densities (VCDs). From this analysis, I found out that although the retrieved $O_3$ VCDs do not contain any significant tropospheric signal, the $NO_2$ VCDs are affected by the anthropogenic emissions. Indeed, I found that the $NO_2$ VCDs are systematically lower during sundays, when the traffic around the ECO observatory is generally lower, and that they decrease with the wind speed measured at an altitude of 20 m, suggesting the presence of $NO_2$ local production. However, a further analysis highlighted the presence of a significant positive peak in the $NO_2$ VCDs during North-East (NE) wind conditions, the direction where the city of Lecce is located with respect to the ECO site. This result suggests that also the transport of $NO_2$ from Lecce significantly affects the $NO_2$ VCDs over the ECO observatory.

The retrieved $NO_2$ and $O_3$ VCDs were then used to study their seasonal variabilities. The results showed that the $NO_2$ monthly mean VCDs range between $3.5 \times 10^{15}$ during winter, and $7 \times 10^{15}$ molecules/cm$^2$ during summer, and that the $O_3$ monthly mean VCDs reach their maximum value of about

$1x10^{19}$ molecules/cm$^2$ during spring and start to decrease, until reaching their minimum of about $7.5x10^{18}$ molecules/cm$^2$, during autumn.

I assessed the quality of the retrieved data comparing them with satellite products measured by the TROPOspheric Monitoring Instrument (TROPOMI) and Ozone Monitoring Instrument (OMI). The results showed a good agreement, with satellite data underestimating the $NO_2$ and $O_3$ VCDs of about 30% and 3%, respectively, in agreement with the results found in literature. This exercise showed the potential of the ECO observatory both for air quality studies and satellite validation.

In the second part of the PhD, I worked within the frame of the Instrument Data Evaluation and Analysis Service (IDEAS) Quality Assurance for Earth Observation (QA4EO) project, funded by the European Space Agency (ESA), with the purpose to create the first Italian Multi AXis-DOAS (MAX-DOAS) measurement site, compliant to the Fiducial Reference Measurements for DOAS (FRM4DOAS) standards, in the Po Valley.

At this scope, I tried to exploit TROPOGAS. First of all, I performed a detailed characterization of the instrument to understand if it could meet all the FRM4DOAS standard requirements. Moreover, I changed its measurement and processing strategy according to the standard guidelines. Unfortunately, since the characterization highlighted that TROPOGAS has a Field Of View (FOV) of about 3.6°, which is wider than the required one, I chose to exploit the new instrument SkySpec-2D, fully compliant to the FRM4DOAS requirements.

As a first step, I assessed the SkySpec-2D's performances through two measurement campaigns. The first one took place on the roof of the CNR-ISAC in Bologna, during August 2021, in sinergy with TROPOGAS. The second one was held at the Boundary layer Air Quality-analysis Using Network of INstruments (BAQUNIN) facility, located on the roof of the La Sapienza University (Rome), during September 2021, when SkySpec-2D measured in sinergy with the well-calibrated Pandora#117 instrument.

Assessed the SkySpec-2D's good performances, my colleagues and I installed it in its permanent position at the Giorgio Fea observatory in SPC, where it is continuously measuring atmospheric spectra since the 1 October 2021. To process these spectra, I developed an automatic processing system that calibrates them, converts them into Network Common Data Form (NetCDF) files compliant to the FRM4DOAS requirements, and retrieves the $NO_2$ and $O_3$ VCDs from its zenith-sky spectra. Today, these NetCDF files are routinely delivered to the FRM4DOAS network where we are waiting for being officially included.

Its MAX-DOAS scans (at elevation angles different from zenith) have been exploited during my period abroad at the Institute of Environmental

Physics (IUP) of the University of Bremen, where one of the best DOAS research group is present. There, I used their retrieval algorithm called Bremen Optimal estimation REtrieval for Aerosols and trace gaseS (BOREAS) to retrieve $NO_2$ vertical profiles in the Po Valley from 1 October 2021 to 13 June 2022. These results have been compared with both satellite and in-situ data, providing high correlations. However, I found that the MAX-DOAS vertical profiles, due to their coarse vertical resolution, underestimate the $NO_2$ concentrations at the ground compared to in-situ data. Moreover, I also found that the tropospheric $NO_2$ VCDs measured by TROPOMI over the Po Valley are underestimated with respect to the ones derived from the MAX-DOAS profiles, due to the a-priori assumptions in the TROPOMI retrieval.

# Chapter 1

# Introduction

The Earth's atmosphere is the gas layer that sorrounds our planet, with its lower part heavily affecting our lives. Since the atmosphere is not a steady state system, monitoring its chemical composition and physical parameters is essential. In particular, since several studies [1, 2] demonstrated the correlation between the observed global warming and the rise of the so called green-house gases concentration due to anthropogenic activity, monitoring the atmospheric composition plays a crucial role.

The monitoring of the atmospheric chemical composition and its temporal evolution has several implications for both human life and health. For example, thanks to the collected data, the scientists understood that the temperature increase, observed over the globe, is highly correlated with the concentrations of some green-house gases, like carbon dioxide ($CO_2$) [4, 5], that are increasing as a consequence of the anthropogenic emissions. In particular, it was discovered that, although both the natural and anthropogenic green-house gases are present only in concentrations lower than 1% of the total (indeed, about 99% of the atmosphere is composed by molecular nitrogen ($N_2$) and molecular oxygen ($O_2$)), they can heavily affect the global radiation budget. This scientific knowledge immediately leads to practical applications such as political mitigation strategies. The assessment of their effectiveness would only be possible continuously monitoring the atmospheric composition and its state.

Another clear, practical example is represented by the discovery of the ozone hole [6], observed for the first time over the Antarctic region in the 1980s. In this case, data led to the discovery of the phenomenon. They also allowed the understanding of the chemical and physical processes involved and how to act to mitigate and solve the problem. In particular, the research directly led to the Montreal protocol in 1987 for regulating the ChloroFluoroCarbons (CFCs) emissions [7], responsible for the ozone hole. Nowadays,

the observations suggest that the ozone hole is reducing in size during the last decades [8].

Today it is also known that, although the presence of stratospheric $O_3$ is positive for protecting life on Earth from the high energetic Ultra-Violet (UV) radiation, its tropospheric presence, mainly due to human activity, is responsible for health diseases [9], increasing the risk of respiratory symptoms [10, 11]. Moreover, upper tropospheric $O_3$ acts as a green-house gas by absorbing long-wave terrestrial radiation [12, 13, 14].

Integrating measurements and models allowed us to understand better the chemical processes occurring under certain conditions. For example, now it is known that the tropospheric $O_3$ is not directly injected into the atmosphere by human activity, but is a secondary product of the interaction of $NO_x$, produced directly by combustions, with solar radiation [15].

Nitrogen oxides ($NO_x$), defined as group made of nitric oxide (NO) and $NO_2$, are released into the atmosphere from both natural and anthropogenic sources. Major $NO_x$ sources include fossil fuel combustion, which is particularly important in urban environments [16]; biomass burning; lightning; and oxidation of ammonia [17, 18]. Although combustion processes directly emit only small quantities of $NO_2$, they release nitrogen monoxide (NO), which rapidly (few minutes) forms $NO_2$ when reacting with ozone molecules. Nitrogen dioxide participates, among others, in catalytic cycles leading to tropospheric ozone ($O_3$) formation. It also acts as a catalyst for the stratospheric $O_3$ destruction [19] and contributes to the formation of secondary aerosols [20].

Together with the mentioned $NO_x$ and $O_3$, several other trace gases emitted by human activity negatively impact the planet. Therefore, monitoring the atmospheric chemical composition is crucial to assess the air quality, mainly in highly polluted regions, and to understand its link with human health. Po Valley, for example, is one of the most polluted regions in Europe due to the high industrialization and its particular weather conditions, related to the geography, that prevent air mixing mainly during winter.

## 1.1 Atmospheric structure

The Earth's atmosphere is composed by a lot of different gases with the molecular nitrogen ($N_2$, 78.1%) and molecular oxygen ($O_2$, 20.9%) being the most abundant ones. The remaining 1%, approximately, is composed by minor costituents such as, water vapor ($H_2O$), carbon dioxide ($CO_2$), ozone ($O_3$), methane ($CH_4$), carbon monoxide (CO), and other trace species. Below the approximate altitude of 100 km, $N_2$ and $O_2$, together with the noble

gases, are well mixed due to their long lifetime. Besides the gases, aerosols, composed by liquid droplets and solid particles, are present in the atmosphere too. In particular, the liquid droplets and ice crystals that form the clouds are consequence of the water vapor condensation, while other kinds of aerosol (for example desert dust or sea salt) are injected into the atmosphere by both natural and anthropogenic activities. Although the presence of such particles is minor and their distributions are highly variable in space and time, they play an important role in the physics of clouds and precipitation and in the global radiation budget, interacting through the scattering and absorption processes with the radiation.

The atmospheric temperature is characterized by spatial inhomogeneities both in the horizontal and in the vertical directions. However, the vertical inhomogeneities are dominant and the different vertical temperature gradients are used to define the atmospheric layers: troposphere, stratosphere, mesosphere and thermosphere. The transition zones between different layers are defined as the altitudes where the vertical temperature gradient ($\frac{dT}{dz}$), also called lapse rate, changes sign and are called: tropopause, stratopause, mesopause and thermopause. This information is summarized in Figure 1.1.

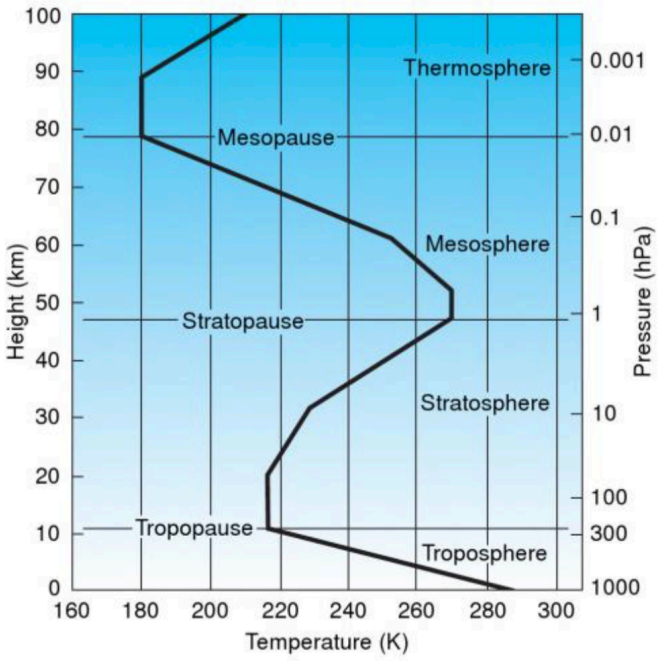


Figure 1.1: A typical midlatitude vertical temperature profile, as represented by the U.S. Standard Atmosphere (from [3]).

The troposphere is the lower part of the atmosphere. It extends from the ground to the tropopause. The altitude of the tropopause (on average about 10 km) varies with the season and latitude. In general, high (low) latitudes are characterized by a lower (higher) tropopause. As shown in Figure 1.1, the tropospheric lapse rate is negative (the temperature decreases with height by about -6.5°C/km) as a consequence of the tropospheric heating processes. Indeed, since the atmosphere is almost transparent to the Visible (VIS) Sun radiation, it reaches undisturbed the surface of the Earth where it is partly absorbed. This phenomenon contributes to increase the temperature of the Earth surface. The Earth surface on turn emits Infra-Red (IR) photons that are absorbed by the lower layers of the atmosphere increasing their temperature. The tropospheric negative lapse rate leads to atmospheric instability and convective motions that, linked to the abundant amount of water vapor present in the troposphere (most of water vapor in the atmosphere is located there), is responsible for the weather phenomena, as precipitations.

The stratosphere is the part of the atmosphere located between the tropopause and the stratopause, from about 10 to 50 km. The stratosphere is characterized by a positive lapse rate that prevents vertical motions and produces very stable and stratified conditions. This positive vertical temperature gradient is related to the ozone and molecular oxygen absorption of the UV solar radiation, fundamental for the development of life on the Earth. Indeed, the largest part of the atmospheric ozone (about 90%) is contained in the stratosphere, with a peak at about 25 km.

The mesosphere, within about 50 and 80 km, is the coldest atmospheric layer, characterized by a negative lapse rate of about -2°C/km. The air density is low, with oxygen, carbon dioxide and nitrogen present with proportion similar to the troposphere.

The outermost layer, the thermosphere, is characterized by a positive lapse rate due to the solar activity. The incoming UV radiation is able to create atoms and ions from the photo-dissociation of molecular oxygen and nitrogen. Due to the very low densities and vertical stable conditions, the molecular diffusion becomes dominant separating the different species according to their atomic or molecular weights.

## 1.2 Observation methods and platforms

The methods used to sound the atmosphere can be divided into two main categories: the in-situ and the remote-sensing techniques. Methods requiring the instrument to be directly in the region to sound, belong to the in-situ category. On the other hand, instruments that allow us to derive information on

an atmospheric region far from the instrument belong to the remote-sensing category. Both measurement approaches have some positive and negative aspects and for this reason it is important to exploit them in sinergy. Indeed, remote-sensing techniques can sound a larger atmospheric region, providing a global coverage in the particular case of satellite missions, without perturbing the region under investigation, as happens with the in-situ measurements. However, the in-situ data generally present a higher accuracy and higher spatial and temporal resolutions, which are particularly useful for detailed studies. The combination between in-situ instruments and mobile platforms such as balloons and airplanes, can be exploited to derive information on a larger region. One example is radiosoundings, where the vertical profiles of physical and chemical parameters are measured with an in-situ approach. The mentioned example highlights that considering only the instrument itself does not allow for a complete description of the measurement features because the hosting platform also has a significant impact. For this reason, the different platforms and their main features are described here.

- *Ground-based* instruments are characterized by several technical advantages. Indeed, they are accurate, stable and easy to maintain, being particularly suitable for studies that involve time series. However, they generally provide a poor spatial coverage. They are usually sensitive to the phenomena occurring close to the instrument, when the measurement is acquired in-situ, and representative of a more extensive area when dealing with remote-sensing instruments.

- *Balloon* platforms can be equipped with both in-situ and remote-sensing instruments to profile the atmospheric parameters up to the stratosphere (about 40 km). Even though this kind of information resolves the atmospheric vertical structure, the horizontal spatial coverage is poor, as the ground-based instruments.

- *Aircrafts* can be equipped with different kinds of instruments, both remote-sensing and in-situ. Unlike the balloons, the aircrafts cannot fly higher than 20 km but they can perform controlled flights, where interesting events occur. Indeed, due to the better spatial coverage with high spatial resolution, aircraft measurements are particularly suitable for analyzing specific events and validating satellite data.

- *Satellites*, equipped with remote-sensing instruments, have the advantage of providing almost global coverage, with differences related to their orbits which can be polar, geo-stationary and equatorial. Polar satellites orbit in low (600-800 km altitude) sun-synchronous orbits

that overpass both the poles (their trajectories do not pass precisely over the poles but close to them), provinding a good spatial coverage. However, these measurements are characterized by low temporal resolution. Indeed, the revisit time on a certain location is of the order of 28 days. The geo-stationary orbit is located on the equatorial plane at an altitude of 36,000 km. These geometrical features allow these satellites to orbit around the Earth with the same angular speed as the Earth's rotation. For this reason, geo-stationary satellites are fixed with respect to the Earth, allowing the monitoring of the same region with a high temporal resolution. However, this kind of orbit only provides a partial coverage of the planet, within a fixed longitude range and within the latitudes between 60° North and South. Equatorial satellites lie on planes which differ for a few degrees from the equatorial plane, at an altitude of about 300 km. These satellites allow covering all the equatorial regions with a better spatial coverage than the geo-stationary ones and with a better temporal resolution than the polar ones.

## 1.3 Principles of remote-sensing measurements

Remote-sensing instruments directly measure the radiations, often in the form of atmospheric absorption or emission spectra. These spectra are processed a-posteriori to infer information about atmospheric regions crossed by the acquired radiation, exploiting the knowledge of the physical processes involved in the interaction between matter and radiation. The remote-sensing instruments can be divided into two different categories: active and passive systems. Active systems, like RAdio Detection And Ranging (RADAR), LIgth Detection And Ranging (LIDAR), Global Positioning System (GPS), are equipped with both a transmitter and a receiver and measure the signal emitted by the transmitter, after interacting with the remote region to sound. Passive systems are equipped with only a receiver and measure the radiation emitted by different natural sources like the Sun, the Earth and the atmosphere itself. They exploit the fact that every object at a temperature higher than 0 K emits radiation. In particular, the radiation emitted by a theoretical black body is described by the Planck's law:

$$B_\lambda(\lambda, T) = \frac{2hc^2}{\lambda^5} \frac{1}{e^{\frac{hc}{\lambda K_B T}} - 1} \tag{1.1}$$

where $B_\lambda(\lambda, T)$ is the spectral radiance distribution, $h$ is the Planck constant, $c$ is the speed of light in the vacuum, $\lambda$ is the wavelength, $K_B$ is the

Boltzmann constant and $T$ is the temperature of the emitter black body. The Sun and the Earth can be approximated as black bodies with temperatures of about 5,800 K and 280 K, respectively. Figure 1.2 shows their corresponding emission curves.

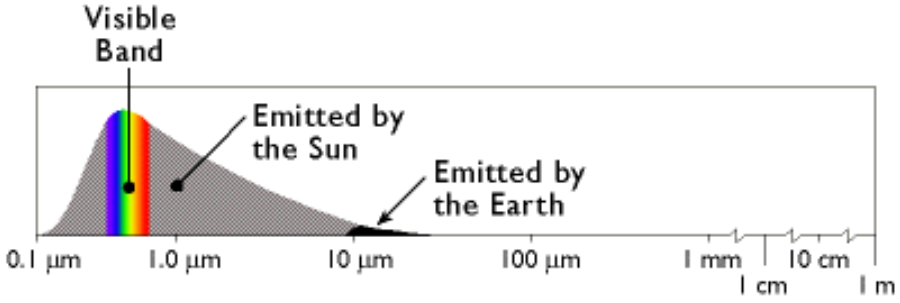


Figure 1.2: Black body emission spectra of the Sun and the Earth as a function of the wavelength. The visible band within the Sun emission is highlighted. Image from [21].

As Figure 1.2 shows, since the Sun and the Earth have very different temperatures, their black body emission spectra show important differences. The peak of the solar spectrum is in the VIS, around 0.5 $\mu$m, while the Earth emission is much weaker and peaks in the IR, around 10 $\mu$m.

When the solar radiation is measured, atmospheric scattering and absorption phenomena are exploited to retrieve information on aerosol and trace gases which interact with the photons. Figure 1.3 shows an example of solar absorption spectrum. It is evident that the solar spectrum, crossing the atmosphere, undergoes an attenuation due to the scattering, mainly at short wavelengths, and to absorption by atmospheric gases, mainly water vapor and carbon dioxide in the IR and ozone in the UV.

On the other hand, when IR Earth emission spectra are measured, information on the trace gases that can emit and absorb IR radiation are retrieved.

The choice of the spectral region depends on the final retrieval target. The more sensitive a specific spectral band is to the final target, the easier and more accurate the retrieval will be. However, other critical aspects affecting remote measurements must be considered. In general, since the absorption measurements usually exploit a bright source such as the Sun, the acquired spectra are characterized by a high Signal to Noise Ratio (SNR) compared to IR measurements, where the signal is much lower (see Figure 1.2). On the other hand, unlike IR spectra that are easily measurable in both daytime and

nighttime, being the result of the Earth emission, VIS measurements can be acquired only during daytime.

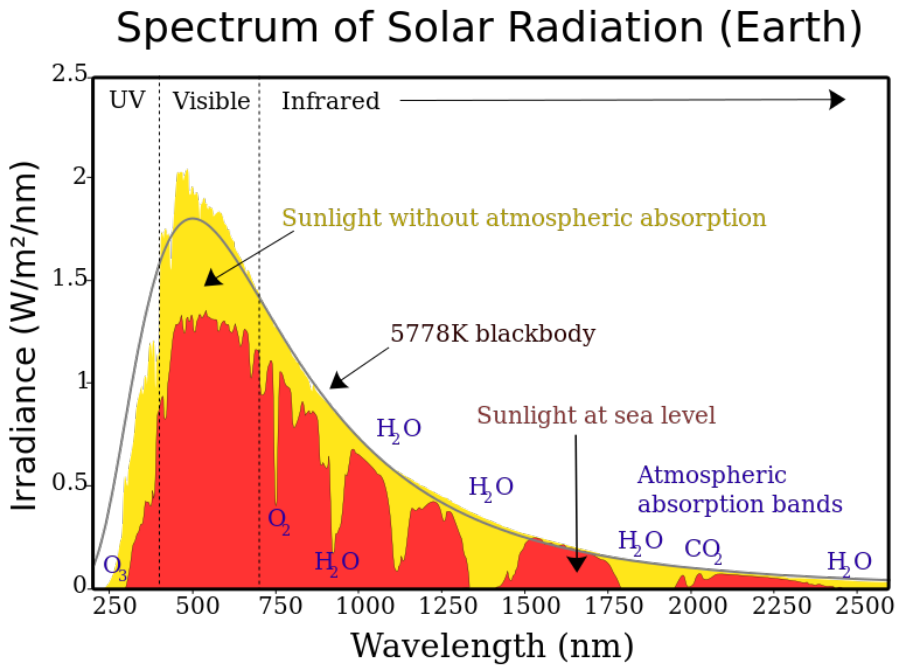


Figure 1.3: Black body solar spectrum (black line), solar spectrum measured at the top of the atmosphere without atmospheric absorption (yellow) and solar spectrum measured at the sea level (red). The main atmospheric gases responsible for the solar radiation absorption are indicated in blue. Image from `https://commons.wikimedia.org/wiki/File:Solar_spectrum_en.svg`.

Another critical aspect to consider when designing remote-sensing measurements is the instrument Line Of Sight (LOS). It is important because it strongly affects the sensitivity of the measurement to specific atmospheric parameters and because its knowledge is needed to understand correctly the physical processes affecting the measurement. Several examples of different adopted LOS exist for both satellite and ground-based devices. For example satellites can adopt limb emission strategies, useful to measure spectra sensitive to the different vertical atmopsheric layers, or nadir geometries that depend also on the properties of the Earth's surface and that can provide information with high horizontal spatial resolution but low vertical resolution.

Among the satellite missions we can list: the Atmospheric Chemistry Experiment - Fourier Transform Spectrometer (ACE-FTS) onboard SCISAT, which measures limb solar occultation spectra; the Michelson Interferometer

for Passive Atmospheric Sounding (MIPAS) onboard the ENVIronmental SATellite (ENVISAT), which measured the IR limb emission spectra; and the TROPospheric Ozone Monitoring Instrument (TROPOMI) onboard the Sentinel-5 Precursor (S-5P), which measures nadir spectra in the VIS, UV and part of the IR.

Ground-based remote-sensing instruments can acquire spectra at zenith and off-axis directions. Some of them can also measure directly the Sun, following its position. Each LOS is sensitive to different atmospheric portions; for example, off-axis measurements, acquired at low elevation angles with respect to the horizon, are mainly sensitive to the lower troposphere.

Among the ground-based remote-sensing devices, we can list the so called Differential Optical Absorption Spectroscopy (DOAS) passive instruments, that are used to retrieve trace gases concentrations from measured VIS and UV diffuse solar spectra, exploiting the DOAS technique [22]. This technique is well-known and widely used because allows to quickly derive trace gases information from measured spectra, as will be explained in Chapter 2. This retrieval strategy is quite different and easier compared to many others that usually require complex and time-consuming retrieval algorithms.

## 1.4 Importance of ground-based DOAS

The ground-based DOAS data are important and useful for two main reasons. They allow to perform scientific studies related to the atmospheric chemical composition and they provide important information for the validation of satellite products.

For the scientific studies, these measurements are able to provide long time series of trace gases Vertical Column Densities (VCDs), from zenith-sky spectra, and lower tropospheric vertical profiles, from Multi-AXis-DOAS (MAX-DOAS) scans, with a temporal resolution of a few minutes, hardly obtainable from satellite and in-situ measurements. Such information is useful to perform air quality studies over a certain region, to study in detail the temporal evolution of physical and chemical processes that occur within timescales of minutes or higher, and to improve the simulation capabilities of the Chemical Transport Models (CTMs) [23].

Although the ground-based DOAS measurements belong to the remote-sensing methods, as the satellite instruments, their different platforms and measurement geometries lead to different retrieved information. Indeed, satellite data are routinely processed to retrieve trace species' VCDs, even though with a lower spatial resolution and with a high revisit time over the same place. Moreover, satellite data are not sensitive to the lower atmo-

spheric layers and, hence, cannot be exploited to retrieve vertical profiles in the lower troposphere. For this reason, the two methods cannot be considered as alternatives but should be exploited in sinergy to study the atmospheric composition better.

The same principle is true when ground-based DOAS and in-situ data are compared. Indeed, the information retrieved from ground-based DOAS spectra cannot be derived from in-situ instruments, except when installed in balloon platforms. However, also in that case, the in-situ information will never be able to provide a temporal continuity, as ground-based DOAS does.

Ground-based DOAS data are also important for satellite validation because the final products retrieved from the two measurement strategies are similar. Indeed, satellite products are usually total VCDs, also derived from zenith DOAS spectra, and tropospheric VCDs that can be easily computed from the vertical profiles retrieved from the MAX-DOAS scans. As written before, balloon-borne instruments can perform similar measurements but with a poor temporal sampling.

Since satellite data are widely used, due to their almost complete global coverage and their availability over remote regions, the satellite validation is an important activity that allows to assess satellite data quality and the existence of possible biases.

Another important aspect of the ground-based DOAS instruments is that they are usually easy to move, making them particularly suitable to study specific local emissions like: volcanos, cities or plums produced by power-plants.

Their main negative aspect is represented by the lack of measurements during the night, when natural VIS and UV radiation is absent. However, this is partially true because also the solar light reflected by the moon can be exploited [24].

## 1.5 DOAS: state of the art

The classical DOAS technique [22] allows to infer atmospheric trace gases information from the measurement of atmospheric spectra in the VIS and UV spectral ranges. The first DOAS measurements date back to the 1920s, when the absorption of the UV radiation was exploited to perform atmospheric ozone ($O_3$) measurements [25]. In the last 100 years, new measurement strategies and analysis techniques have been developed, allowing to retrieve information on trace species, such as: stratospheric columnar contents [26], total VCDs [27] and vertical profiles in the lower part of the troposphere [28]. In particular, today, the main atmospheric species retrieved with this

technique are: nitrogen dioxide ($NO_2$), ozone ($O_3$), formaldehyde (HCHO), glyoxal (CHOCHO) and sulphur dioxide ($SO_2$).

The DOAS technique can be applied to atmospheric spectra acquired from different platforms, such as: satellite [29], airplane [30], ground [31], ship [32] and car [33], and from different measurement set-up exploiting both passive (sun) and active (lamps) light sources. However, since this thesis is related to the ground-based diffuse solar measurements, from here on the focus will be on this specific DOAS set-up.

Since the application of non-appropriate data processing guidelines can affect the measured spectra systematically, leading to important errors in the retrieved final results, in 2016 the European Space Agency (ESA) started the Fiducial Reference Measurements for DOAS (FRM4DOAS) activity. The project, in addition to the creation of a consistent network useful for the validation of satellite data, has the purpose to increase the data quality over a standard threshold, in order to avoid biased results. Therefore, a list of standard guidelines was drawn with the purpose to harmonize the ground-based DOAS measurements according to instrumental features and both measurement and processing standard practices. The main FRM4DOAS guidelines are reported in Table 1.1 and further information can be found in the following web page (`https://frm4doas.aeronomie.be`).

Table 1.1: Main FRM4DOAS guidelines for ground-based DOAS air quality observations.

| | |
|---|---|
| **INSTRUMENTAL GUIDELINES** | |
| **Spectral resolution (nm)** | $< 0.8$ (UV) / 1.5 (VIS) |
| **FOV (°)** | $< 1.5$ |
| **OPERATION GUIDELINES** | |
| **MAX-DOAS scans** | when SZA $< 85°$ |
| **Elevation angles during MAX-DOAS** | at least 1°, 2°, 3°, 5°, 10°, 30° |
| **Zenith spectra** | when SZA $< 94°$ |
| **Dark signal** | at least daily measurements |
| **Slit function** | at least once per year |
| **Horizon scans** | at least once per week |
| **DATA PROCESSING GUIDELINES** | |
| **Apply to spectra:** | spectral calibration<br>dark signal correction<br>non-linearity correction |
| **Average spectra** | until SNR $> 3000$ (VIS) / 4000 (UV) |

Before this PhD, the Consiglio Nazionale delle Ricerche - Istituto di Scienze dell' Atmosfera e del Clima (CNR-ISAC) owned several custom-built ground-based DOAS instruments for research purposes. However, none of

them was included into the validation network because did not meet the FRM4DOAS standard requirements. This situation was generally present in Italy where, differently from other European countries, no FRM4DOAS-compliant ground-based measurements were acquired. For this reason, one of the main purposes of this PhD work was to create, within the frame of an ESA project, the first Italian FRM4DOAS-compliant MAX-DOAS measurement site in the Po Valley.

The strategic importance of this reference station in the Po Valley has become further evident in the last period due to a remarkable decline in $NO_2$ concentrations in Northern Italy as a consequence of the lockdown period. Indeed, that moment has represented a unique opportunity to better understand the air pollution in this region.

This PhD thesis is organized as follows. The DOAS technique is explained in detail in Chapter 2. All the DOAS instruments used for this thesis are described in Chapter 3. Chapter 4 is focused on the characterization of the Environmental Climate Observatory (ECO) observatory in Lecce, exploiting the Gas Analyser Spectrometer Correlating Optical Differences / New Generation 4 (GASCOD/NG4) measurements. The work performed to create the first Italian FRM4DOAS-compliant MAX-DOAS site in the Po Valley is discussed in Chapter 5. In Chapter 6, the results regarding the $NO_2$ vertical profiles retrieved in the Po Valley are shown. The conclusions are drawn in Chapter 7.

# Chapter 2

# DOAS technique

The DOAS technique is a remote-sensing strategy used to derive trace gases information in the atmosphere exploiting the absorption of VIS and UV radiation. In this chapter, the technique will be described in detailed, focusing on the physical assumptions, the mathematical approximations used, and the atmospheric information that can be derived. More details on these topics can be found in reference [22].

## 2.1 DOAS principle

The DOAS technique is based on the classical absorption spectroscopy. Some molecules (e.g. $NO_2$ and $O_3$), contained in a gaseous medium, can absorb VIS and UV radiation that crosses the medium, in different regions of the electromagnetic spectrum depending on their energy levels.

Figure 2.1 schematically shows the physical phenomenon of the gas absorption. In absence of scattering processes, the absorption is mathematically described by the Lambert-Beer's law that can be written as:

$$I(\lambda) = I_0(\lambda)e^{-\sigma(\lambda)cL} \tag{2.1}$$

where $I_0(\lambda)$ is the incident intensity at the wavelength $\lambda$ of a light beam emitted by a radiation source and $I(\lambda)$ is the radiation intensity of the beam after crossing the absorbing medium of thickness $L$, where the absorber is present at a uniform concentration $c$. $\sigma(\lambda)$ is the absorption cross-section at the wavelength $\lambda$. This quantity, as a function of the wavelength, is linked to the molecular energy transitions and is a typical characteristic of each species. The quantity $\chi(\lambda) = \sigma(\lambda)cL$ is called optical thickness.

However, in general, the absorber concentration $c$ is not uniform in space.

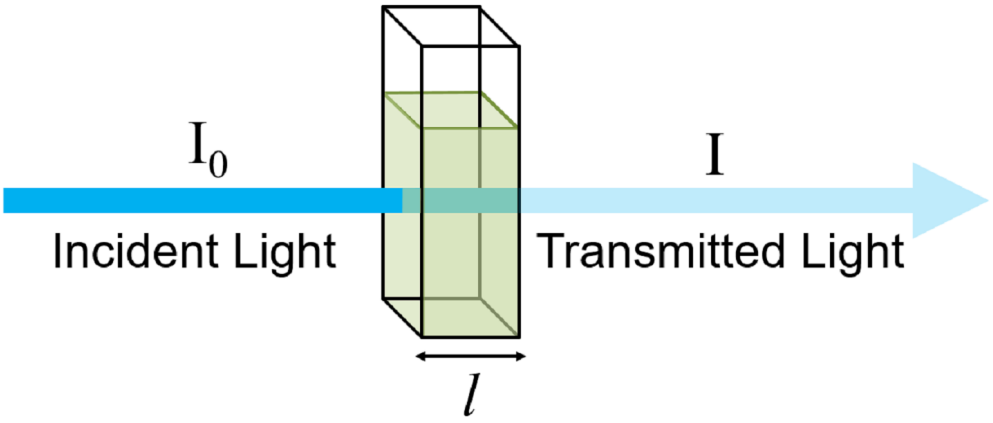


Figure 2.1: Attenuation of a light beam due to the molecular absorption.

In this case, the quantity $c$ is replaced by $\bar{c}$ that represents the mean concentration along the path $L$.

Using equation 2.1, the average trace gas concentration can be derived as:

$$\bar{c} = \frac{ln(\frac{I_0(\lambda)}{I(\lambda)})}{\sigma(\lambda)L} = \frac{\chi(\lambda)}{\sigma(\lambda)L} \tag{2.2}$$

where $\chi(\lambda)$ is the optical thickness of the layer crossed by the light, due to the absorber having cross-section $\sigma(\lambda)$.

In general, equation 2.2 can be used for absorption spectroscopic applications in the laboratory, where the quantity $I_0(\lambda)$, emitted by an active light source, can be easily measured. However, in most of the atmospheric applications that exploit the solar radiation, it is difficult to measure the input signal $I_0(\lambda)$ without the atmospheric contribution.

The optical thickness $\chi(\lambda)$ represents the attenuation of the light beam due to absorption. However, in atmospheric conditions, the attenuation of a light beam is a consequence of both absorption and scattering processes. This can be considered introducing in the Lambert-Beer equation 2.1 additional terms. Moreover, the instrument is not perfect and has a response function $A(\lambda)$ that modifies the measurement. Hence, according to these considerations, the new equation becomes:

$$I(\lambda) = A(\lambda)I_0(\lambda)e^{-L\left(\sum_j(\sigma_j(\lambda)\bar{c_j})+\epsilon_R(\lambda)+\epsilon_M(\lambda)\right)} \tag{2.3}$$

where $A(\lambda)$ includes all the instrumental effects and the total optical

thickness is composed by three different contributions: $\sigma_j(\lambda)\bar{c_j}$, $\epsilon_R(\lambda)$ and $\epsilon_M(\lambda)$. $\sigma_j(\lambda)\bar{c_j}$ is the absorption due to a specific gas $j$, while $\epsilon_R(\lambda)$ and $\epsilon_M(\lambda)$ represent the attenuation due to Rayleigh (by molecules) and Mie (by particles) scattering processes, respectively.

In order to precisely estimate the concentration of a trace gas in atmosphere, it is therefore necessary to know all the scattering factors affecting the light intensity. However, while the molecular absorption is made of narrow spectral features, the scattering and instrumental effects have a broad-band structure. Therefore, the attenuation of equation 2.3 can be divided in a broad-band and narrow-band contributions. Since the molecular absorption presents both narrow- and broad-band spectral features, the absorption cross-sections $\sigma_j(\lambda)$ can be written as:

$$\sigma_j(\lambda) = \sigma_{j0}(\lambda) + \sigma_j^{'}(\lambda) \tag{2.4}$$

where $\sigma_{j0}(\lambda)$ and $\sigma_j^{'}(\lambda)$ represent the broad- and narrow-band absorption cross-sections.

In this way, equation 2.3 can be written separating the broad- and narrow-band spectral structures affecting the optical thickness $\chi$:

$$I(\lambda) = I_0(\lambda)e^{-L\left(\sum_j(\sigma_j^{'}(\lambda)\bar{c_j})\right)}A(\lambda)e^{-L\left(\sum_j(\sigma_{j0}(\lambda)\bar{c_j})+\epsilon_R(\lambda)+\epsilon_M(\lambda)\right)} \tag{2.5}$$

The first exponential term in equation 2.5 represents the highly varying absorption, also called differential absorption, while the second exponential multiplied by $A(\lambda)$ accounts for all the slowly varying terms such as: broad-band absorption, Rayleigh and Mie scattering and instrumental effects dependent on the optical system. This equation is the basis of the DOAS technique that exploits the differential absorption to derive trace gases concentrations.

Since we need to separate broad- and narrow-band contributions, the DOAS method requires to measure a spectral range of a certain width. Indeed, the concepts of narrow- and broad-band absorptions are meaningless for monochromatic radiation and depend on the width of the considered spectral window.

The use of differential absorption over an extended spectral range leads to several advantages:

- since the instrumental effects usually present broad spectral characteristics without influencing the differential absorption, no continuous calibration of the optical properties is required.
- The use of an extended spectral range ensures the unique identification of a trace gas absorption.

- This technique enables to detecte weak absorptions related to low optical thicknesses.

In general, the DOAS technique can be applied to several and different measurement setups, each with specific advantages and disadvantages. The setups can be divided into two big different categories: the active and passive DOAS, according to the light source used, artificial or natural, respectively.

- In the active DOAS [31, 34], the average concentration of a trace species crossed by the light emitted by an artificial emitter to the spectrometer (receiver) is estimated. This method is similar to classical absorption spectroscopy, usually applied in the laboratory. However, the concentration of the gases that absorb VIS and UV radiation, is usually low in the atmosphere, leading to problems in their detectability. In this case, the only way to make the absorption signal detectable is to increase the path crossed by the light, increasing the distance between emitter and receiver or building a special system that allows multiple reflections before that the signal reaches the spectrometer.

- In the passive DOAS, the light sources are the sun, the moon and rarely the stars. The principle is the same; the Lambert-Beer equation 2.1 allows to estimate the gas absorption in the path crossed by the photons from the natural source of light to the spectrometer. However, the passive DOAS applied to solar measurements introduces the possibility to measure the scattered light, making the application of equation 2.1 less intuitive. Indeed, unlike the direct solar measurements, the atmospheric path crossed by the diffused light is not well defined but is a combination of different paths.

Since this thesis involves the DOAS diffuse solar measurements, the next sections 2.2, 2.4 and 2.5 will focus mainly on this specific application of the DOAS measurements.

## 2.2 Mathematical description

Equation 2.5 describes the monochromatic radiation that reaches the telescope of the instrument. However, in the mathematical treatment, it should be considered that the instrument has a finite spectral resolution, leading to a change in the spectrum shape. This effect can be included through a convolution of $I(\lambda)$ with the instrument response function $H(\lambda)$:

$$I^*(\lambda) = I(\lambda) * H = \int_{-\Delta\lambda}^{+\Delta\lambda} I(\lambda - \lambda^{'}) H(\lambda^{'}) d\lambda^{'} \tag{2.6}$$

In theory, the integration limits should be $-\infty$ and $+\infty$. However, since the instrument function $H(\lambda)$ can be usually approximated by a Gaussian function, the integration can be performed between $\pm\Delta\lambda$, being $\Delta\lambda$ the distance from the central frequency where $H(\lambda)$ is almost null. Applying equation 2.6 to equation 2.5 and combining $I_0(\lambda)$ and all the broad-band terms as $I_0^{'}(\lambda - \lambda^{'}, L)$, we have:

$$I^*(\lambda, L) = \int_{-\Delta\lambda}^{+\Delta\lambda} I_0^{'}(\lambda - \lambda^{'}, L) e^{-\int_0^L \sum_j (\sigma_j^{'}(\lambda - \lambda^{'}, p, T)\rho_j(l))dl} H(\lambda^{'}) d\lambda^{'} \tag{2.7}$$

where $\rho_j(l)$ represents the concentration of the $j^{th}$ gas along the path $L$ crossed by the photons and $\sigma^{'}(\lambda - \lambda^{'}, p, T)$ is the differential absorption cross-section of the $j^{th}$ gas that depends on the wavelength, atmospheric pressure and temperature. Equation 2.7 can be heavily simplified under the assumptions that $\sigma_j^{'}$ is independent from the pressure and temperature, $I_0^{'}(\lambda)$ is slowly variable with the wavelength ($I_0^{'}(\lambda - \lambda^{'}, L) \approx I_0^{'}(\lambda, L)$ in the spectral range between $\lambda - \Delta\lambda$ and $\lambda + \Delta\lambda$) and that the atmospheric molecules are responsible for weak absorptions in the VIS and UV spectral ranges. Under these assumptions and without reporting the whole mathematical procedure, equation 2.7 becomes:

$$ln\Big(\frac{I^*(\lambda, L)}{I_0^{'}(\lambda, L)}\Big) \approx \sum_j \bar{c_j} L ln\Big[\int_{-\Delta\lambda}^{\Delta\lambda} e^{-\sigma^{'}(\lambda - \lambda^{'})} H(\lambda^{'}) d\lambda^{'}\Big] \tag{2.8}$$

where $\bar{c_j}$ is the concentration of the $j^{th}$ gas averaged along the path crossed by the light.

As seen from the final equation 2.8, the Lambert-Beer law can be linearised under the assumptions of weak absorbers, which is usually satisfied in the atmosphere in the VIS and UV, and of smooth light source. However, when the DOAS technique is applied to direct or diffuse solar measurements, highly variable spectral structures (Fraunhofer lines, see Figure 2.2) are present in the solar spectrum and the approximation $I_0^{'}(\lambda - \lambda^{'}, L) \approx I_0^{'}(\lambda, L)$ introduces not-negligible errors. An analogous procedure, without the mentioned approximation, leads to a more general result:

$$ln\Big(\frac{I^*(\lambda, L)}{I_0^{'*}(\lambda, L)}\Big) \approx \sum_j \bar{c_j} L ln\Big[\frac{\int_{-\Delta\lambda}^{\Delta\lambda} I_0^{'}(\lambda - \lambda^{'}, L) e^{\sigma_j^{'}(\lambda - \lambda^{'})} H(\lambda^{'}) d\lambda^{'}}{\int_{-\Delta\lambda}^{\Delta\lambda} I_0^{'}(\lambda - \lambda^{'}, L) H(\lambda^{'}) d\lambda^{'}}\Big] \tag{2.9}$$

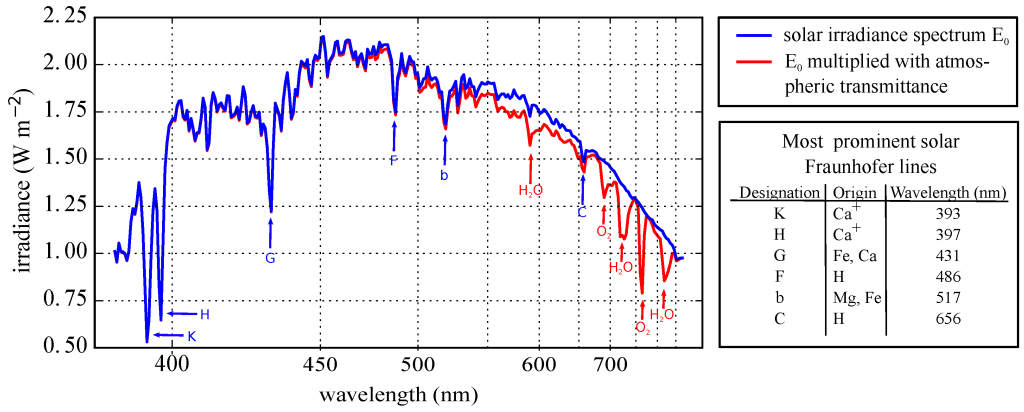


Figure 2.2: Fraunhofer lines in a solar spectrum marked by their designators. Image from [35].

where $I_0'^*(\lambda, L)$ is the input spectrum $I_0'$ convolved with the instrument function $H(\lambda)$. In the DOAS method, the equation 2.9 is usually used, with the right term approximated as in equation 2.8 and a correction called $I_0$ correction [36, 37] is then applied a posteriori to the differential absorption cross-sections $\sigma_j'$. The final form of the equation is:

$$ln\Big(\frac{I^*(\lambda, L)}{I_0'^*(\lambda, L)}\Big) \approx \sum_j \bar{c_j} L ln\Big[\int_{-\Delta\lambda}^{\Delta\lambda} e^{-\sigma'(\lambda-\lambda')} H(\lambda')d\lambda'\Big] \qquad (2.10)$$

Due to its linearity, Equation 2.10 allows to fit the concentrations of the $j$ gases integrated along the path ($\bar{c_j}L$), knowing their differential absorption cross-sections $\sigma'(\lambda)$, the instrumental function $H(\lambda)$, usually approximated as a Gaussian curve, and two spectra $I^*(\lambda, L)$ and $I_0^*(\lambda, L)$ convolved with the same instrument functions $H(\lambda)$. For this reason, a spectrum measured by the same instrument is usually used as a reference spectrum ($I_0^*(\lambda, L)$). It is usually acquired at the zenith around noon when the sun is high, and the optical path due to the differential absorption is minimum. Indeed, the more the Sun is high, the less the atmospheric path crossed by the photons in a zenith measurement configuration is, as shown in Figure 2.3. However, the absorption contribution in the reference spectrum is not negligible and should be estimated.

The concentrations of the $j$ absorbing gases integrated along the path crossed by the photons ($\bar{c_j}L$) are called Slant Column Densities (SCDs) and are defined as:

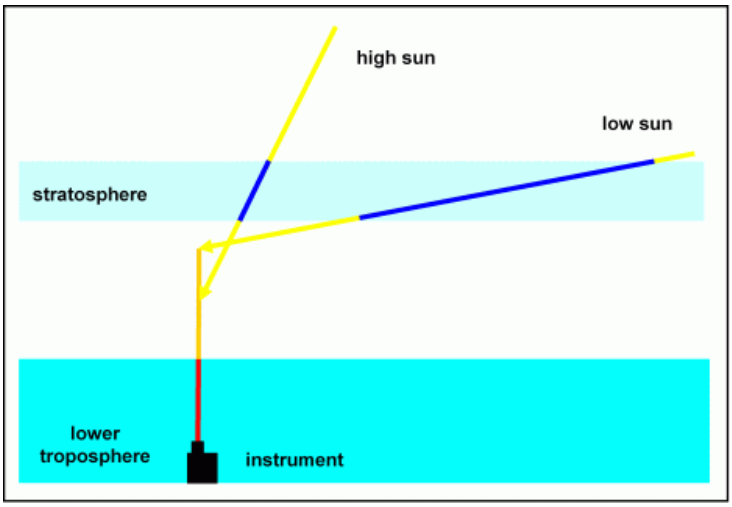


Figure 2.3: Observation geometry of zenith-sky measurements performed by a ground-based DOAS instrument. Image from `http://www.iup.uni-bremen.de/doas/maxdoas_instrument.htm`.

$$SCD = \int_0^\infty c(s)ds \tag{2.11}$$

where $c(s)$ is the gas concentration and the integration is performed along the photon's slant path.

## 2.3 QDOAS software

QDOAS (`https://uv-vis.aeronomie.be/software/QDOAS/`), developed by the DOAS UV-VIS team at the Royal Belgian Institute for Space Aeronomy (BIRA-IASB), is the software used in this thesis to retrieve the trace gases' SCDs from the measured VIS and UV diffuse solar spectra. According to equation 2.10, the DOAS retrieval is a linear problem. However, since the analysis is strongly dependent on the spectral calibration and possible misalignments between $I^*(\lambda, L)$ and $I_0^*(\lambda, L)$, QDOAS also gives the possibility to fit, together with the SCDs, some parameters that account for small wavelength shifts between the two spectra. Moreover, a offset between the two spectra is also fitted, in order to account for the stray-light and dark current effects. The stray-light is light present in the optical system not intended in the design and coming from a different source or the same source but following different paths. While the dark current is a signal generated inside the detector even when a real light source is not present. As a conse-

quence, the linearity of the equation is broken and the SCDs are fitted using a Marquardt-Levenberg algorithm [38] to the following equation:

$$ln\Big(\frac{I^*(\lambda-\Delta(\lambda))-offset(\lambda)}{I_0^*(\lambda)}\Big)+\sum_j(K_j(\lambda)SCD_j)+P(\lambda)=0 \qquad (2.12)$$

An example of a fit performed to estimate the $NO_2$ SCD is reported in Figure 2.4.

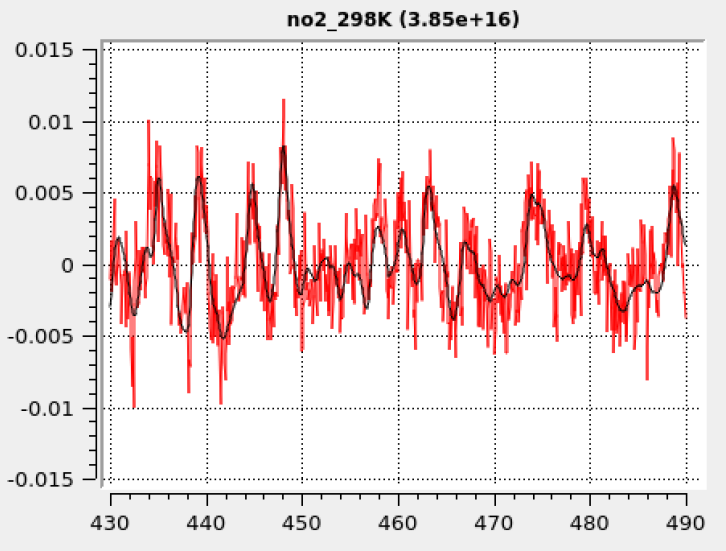


Figure 2.4: The black line represents the differential optical depth (only the differential absorption cross-section is considered) due to the $NO_2$ absoprtion, as a function of the wavelength in the x-axis (nm). The red line is the sum of the black line and the residual of the fit. The fitted $NO_2$ SCD is 3.85x$10^{16}$ molec/$cm^2$.

The new terms used in the QDOAS equation 2.12 are:

- $\Delta(\lambda)$ contains the shift and stretch parameters fitted by QDOAS to align $I^*(\lambda)$ and $I_0^*(\lambda)$ spectrally. $\Delta(\lambda)$ is expressed as:

$$\Delta(\lambda)=a+b(\lambda-\lambda_0)+c(\lambda-\lambda_0)^2 \qquad (2.13)$$

  where $a$, $b$ and $c$ are the fitted parameters, $\lambda$ is the wavelength and $\lambda_0$ is the central wavelength of the considered spectral range.

- $offset(\lambda)$ is the term used to account for all the instrumental sources of offset that can affect the measured spectra, such as the stray-light and dark current. In the QDOAS, the offset is expressed as:

$$offset(\lambda) = (a + b(\lambda - \lambda_0) + c(\lambda - \lambda_0)^2)\bar{I} \tag{2.14}$$

  where $a$, $b$ and $c$ are the fitted parameters, $\lambda_0$ is the central wavelength and $\bar{I}$ is the average intensity of the spectrum.

- $P(\lambda)$ accounts for all the broad-band spectral structures (broad-band absorption, Rayleigh and Mie scattering) and is parametrized as a polynomial of degree up to 5 (customizable by the user).

- $K_j$ are the terms containing the differential absorption cross-sections of the $j$ absorbing gases convolved with the instrumental function $H(\lambda)$. However, one of the $K_j$ required by QDOAS does not contain the absorption cross-section of an actual gas but a synthetic cross-section used to account for the Ring effect. This effect is caused by the inelastic scattering, affecting part of the photons, that undergo a wavelength change of a few nanometers [39]. QDOAS accounts for this effect through the additional Ring cross-section computed according to the approach described in [40, 41].

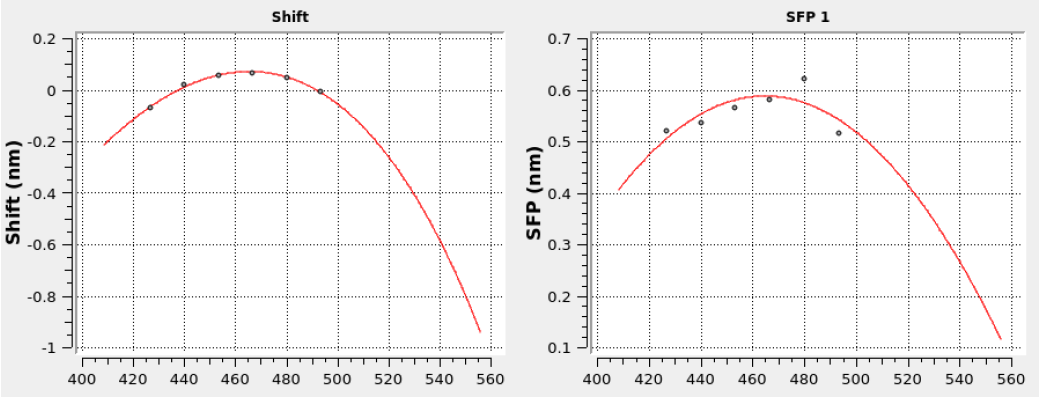


Figure 2.5: Shift (left) and instrumental function width (right), as a function of the wavelength (nm), fitted by QDOAS during the calibration of the $I_0$ spectrum with respect to the high resolution solar reference atlas. The discrete dots are the values computed during the calibration procedure. The red curves, which fit the dots, are the functions used to represent the shift and instrumental function for the QDOAS analysis.

As previously mentioned, QDOAS is able to spectrally align $I^*(\lambda)$ to the reference spectrum $I_0^*(\lambda)$. However, before that, ensuring that $I_0^*(\lambda)$ is spectrally well calibrated is essential. For this purpose, QDOAS calibrates the reference spectrum $I_0^*(\lambda)$ according to the high resolution solar reference atlas described in [42]. The calibration is performed through an iterative process that stops when a good match between the two solar spectra is found. The calibration is also useful to estimate the spectral resolution of the measured spectra. Indeed, during the iterative steps, the high resolution solar reference atlas is continuously convolved with Gaussian functions (representing the instrumental function) having different widths. At the end of the process, the best estimates of shift and stretch, evaluated according to equation 2.13 and of the Gaussian width related to the spectral resolution, are computed (see Figure 2.5). The calibration procedure is very important in order to avoid misalignments between the two measured spectra and the absorption cross-sections, and also to properly estimate the instrumental function $H(\lambda)$, used to convolve the exponential terms containing the differential absorption cross-sections (see equation 2.10).

## 2.4 Zenith-scattered light SCDs

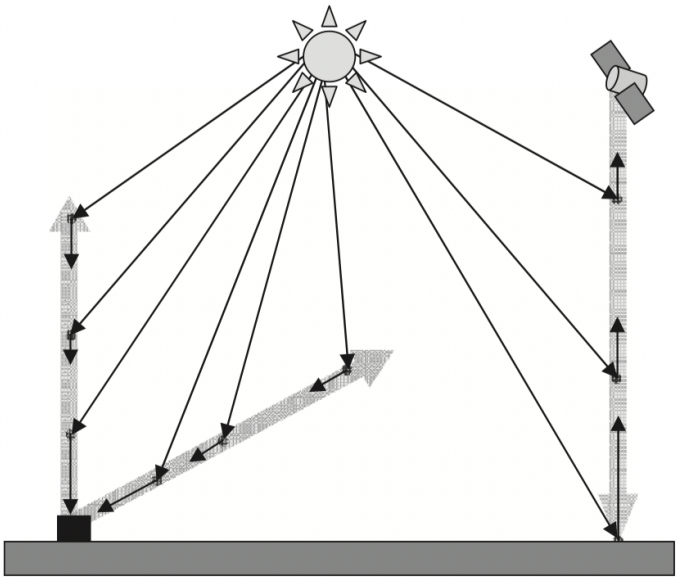

Figure 2.6: Example of undefined atmospheric paths in DOAS measurements of diffuse solar light. Image from [22].

The definition of SCD (equation 2.11) is an easy concept if the path of the radiation in the atmosphere is well defined, as in the case of direct solar measurements. However, the concept becomes less intuitive when the measurement involves diffuse solar light because the actual path of the radiation collected by the instrument is always a combination of several paths, as shown in Figure 2.6, due to the different scattering patterns.

In this case, a more general definition of the SCD is more appropriate:

$$SCD = \frac{\chi'(\lambda)}{\sigma'(\lambda)} \tag{2.15}$$

where $\chi^{'}$ is the differential optical thickness and $\sigma^{'}$ the differential absorption cross-section. In order to precisely understand what a zenith-sky measurement represents, when acquired in clear-sky conditions, the molecular absorption and the Rayleigh scattering phenomena must be taken into account. Neglecting multiple scattering processes, the radiation measured by a ground-based instrument can be described as the solar light, attenuated along its slant path from the top of the atmosphere to the vertical above the instrument, which is scattered towards the ground in the instrument direction and which is attenuated in its vertical path before reaching the detector. However, the scattering of the slant solar beam into the vertical direction can happen at different heights. The most probable altitude where the scattering occurs depends on the Solar Zenith Angle (SZA) and is a compromise between the Rayleigh scattering probability, which increases in the lower atmosphere where the density is higher, and the solar beam intensity which increases with altitude. According to these considerations and taking into account only one of all the possible paths, the radiation $I_S(\lambda, z)$ reaching the instrument due to only Rayleigh scattering processes can be expressed as:

$$I_S(\lambda, z) = \sigma_R(\lambda)\rho(z)I_0(\lambda)e^{-\sigma_R(\lambda)\int_z^\infty \rho' A(z',\theta)dz}e^{-\sigma_R(\lambda)\int_0^z \rho(z')dz'} \tag{2.16}$$

where $\sigma_R$ is the Rayleigh scattering cross-section, $\rho(z)$ is the air density, $z$ is the altitude where the scattering occurs, $A(z', \theta)$ is the geometrical factor that accounts for the slant path and $\theta$ is the SZA. The first and second exponential terms represent the Rayleigh scattering in the slant and vertical paths, respectively. Including the absorption processes, the radiation due to only one possible path is:

$$I_S^A(\lambda, z) = I_S(\lambda, z)e^{-\sigma_A(\lambda)\int_z^\infty C(z')A(z',\theta)dz}e^{-\sigma_A(\lambda)\int_0^z C(z')dz'} \tag{2.17}$$

Taking into account that the total radiation reaching the detector, due to both scattering and absorption and only to scattering processes, is the

integral over all the possible paths of $I_S^A(\lambda, z)$ and $I_S(\lambda, z)$, respectively, the SCD for an undefined path is:

$$SCD = \frac{1}{\sigma(\lambda)} ln\left(\frac{\int_{paths} I_S^A(\lambda, z)dz}{\int_{paths} I_S(\lambda, z)dz}\right) \tag{2.18}$$

The SCD expressed in equation 2.18 is the quantity that can be retrieved from zenith-sky measurements. This equation can also be written making explicit all the SCDs $S'$ relative to the different paths:

$$SCD = \frac{1}{\sigma(\lambda)} ln\left(\frac{\int_{paths} I_S(\lambda, z)e^{-\sigma(\lambda)S'}dz}{\int_{paths} I_S(\lambda, z)dz}\right) \tag{2.19}$$

From equation 2.19, we can notice that, if the terms $S'$ do not change (direct solar measurements case, where the path is unique and well defined), the exponential term in the numerator can be moved in front of the integral and the equation becomes the Lambert-Beer law of equation 2.1. On the other hand, if diffuse solar measurements are considered, the equation can be simplified for a weak absorber ($e^x \approx 1 + x$, for $-\epsilon < x < \epsilon$). Therefore, the numerator of the logarithm in the equation 2.19 can be written as:

$$\begin{aligned}
&\int_{paths} I_S(\lambda, z)e^{-\sigma(\lambda)S'}dz \approx \int_{paths} I_S(\lambda, z)(1 - \sigma(\lambda)S')dz = \\
&= \int_{paths} I_S(\lambda, z) - \sigma(\lambda) \int_{paths} I_S(\lambda, z)S' = \left(\int_{paths} I_S(\lambda, z)\right)(1 - \sigma(\lambda)\bar{S}) \approx \\
&\approx \left(\int_{paths} I_S(\lambda, z)\right)e^{-\sigma(\lambda)\bar{S}}
\end{aligned} \tag{2.20}$$

where:

$$\bar{S} = \frac{\int_{paths} I_S(\lambda, z)S'}{\int_{paths} I_S(\lambda, z)} \tag{2.21}$$

Equations 2.20 and 2.21 show that equation 2.18 can be written as the Lambert-Beer law, with the SCD $\bar{S}$ which is the intensity-weighted average of all the slant columns relative to the different paths.

In general the SCDs, retrieved with the DOAS technique from zenith-sky measurements, need to be converted into the VCDs representing the gas concentrations integrated along the vertical direction. This can be done using the Air Mass Factors (AMFs) that mathematically link the SCDs to the VCDs and that are defined as:

$$AMFs = \frac{SCDs}{VCDs} \tag{2.22}$$

For a direct solar measurement, since the radiation path is well defined, the AMF plays the role of a geometrical factor between the slant and the vertical column. More complexities arise dealing with diffuse solar measurements, where the AMFs contain all the physical processes summarized in equation 2.21 and need to be properly simulated by a radiative transfer code. Indeed, although zenith-sky measurements and processing methods are straightforward to implement, the errors on the simulated AMFs can be very high, leading to high errors in the final VCDs. In particular, the AMFs depend on the input profiles, mainly the trace gas of interest, the aerosol content, the SZA and the surface albedo.

In this thesis, the AMFs for the conversion of the SCDs to VCDs from zenith-sky measurements are simulated with the SCIATRAN Radiative Transfer Model (RTM) [43], which can account for all the significant radiative transfer processes. As input for the simulations, standard trace gases, vertical temperature and pressure profiles available in the SCIATRAN code, which account for monthly and latitudinal variations are used. Moreover, no presence of aerosol and a constant surface albedo of 0.3 are used for the simulations. For each scenario, the AMFs are simulated for a discrete set of SZA values. Then they are interpolated to the SZA value relative to the SCD to be converted. However, it must be taken into account that the real AMFs can strongly differ from the simulated ones, introducing an important source of error [44, 45]. In particular, the way the profile of the target trace gas, used as input for the simulations, impacts on the computed AMFs will be shown in Section 4.1.4.

## 2.5 MAX-DOAS technique

The results of this thesis are obtained also exploiting the MAX-DOAS technique, which allows to retrieve the tropospheric vertical profiles of trace gases and extinction coefficient due to aerosol. In this case, the diffuse solar spectra are measured at different elevation angles (see Figure 2.7) to obtain information from different atmospheric layers.

This measurement strategy can be implemented for different azimuth directions to derive spatial inhomogeneities of trace gases concentrations. Since all the measurements in a scan are used to retrieve one vertical profile, particular attention must be paid to the measurement time, which should not be too long.

There are several and different strategies for the retrieval of vertical profiles from MAX-DOAS measurements. Here, I describe one of them, focusing on the method adopted by the retrieval algorithm used in this thesis.

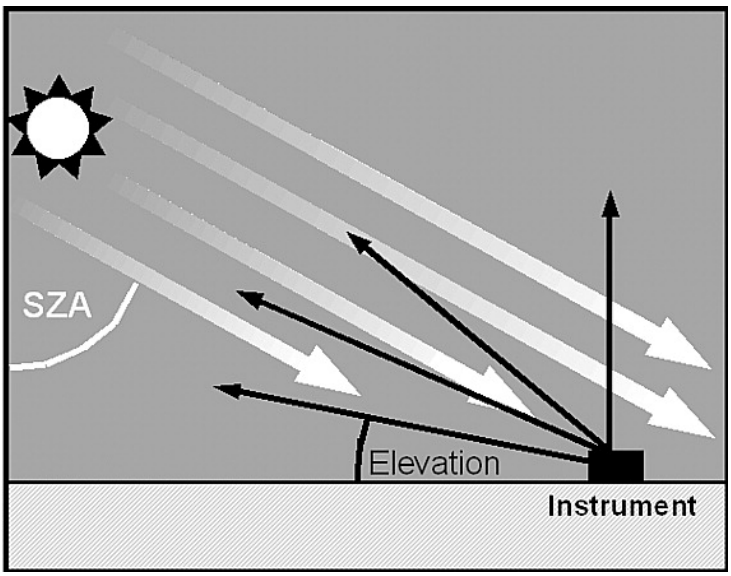


Figure 2.7: Measurement geometry during MAX-DOAS scans. Image from [46].

The first part of the analysis of the MAX-DOAS measurements involves the retrieval of the SCDs with the QDOAS software, as explained in section 2.3. In particular, all the not-zenith spectra acquired in a scan must be analyzed using as a reference spectrum the zenith spectrum relative to the same scan. During this step, in addition to the SCDs of the target gas, it is essential to retrieve also the SCDs of $O_4$, an oxygen dimer, which presents absorption lines in the VIS and UV. Indeed, $O_4$ is a well-mixed species, approximately constant in space and time, and its SCDs can be used to infer scattering properties of the atmosphere due to aerosol.

Unlike the estimate of the VCDs discussed in section 2.4, the retrieval of vertical profiles needs a retrieval algorithm which uses the estimated $O_4$ and target species SCDs as input. The complete retrieval is performed with the following steps:

- *Retrieval of aerosol extinction profile.*

  In this step, the $O_4$ SCDs are used as input, to retrieve the aerosol extinction profile. The retrieval starts with an a-priori extinction profile and converges iteratively to the solution. The process stops when the

estimated aerosol extinction profile leads to $O_4$ SCDs, simulated by a forward model, equal, within a certain threshold, to the measured ones.

- *BOX-AMFs simulation.*

  The aerosol extinction profile, retrieved in the previous step, is used as input for the SCIATRAN RTM to simulate the BOX-AMFs. The BOX-AMFs are defined as the AMFs (see equation 2.22), with the only difference that the AMFs are representative of the whole atmospheric column, because link the total SCDs to the total VCDs, while the BOX-AMFs are resolved in altitude and each of them links the VCD within a certain atmospheric layer to the SCD in the same layer. As the AMFs, they depend on scattering processes, due to the aerosol, the surface albedo (mainly the BOX-AMFs relative to the lower layers), the SZA and the wavelength. For these simulations, the same input parameters used for the AMFs, described in section 2.4, are adopted. The only difference is that, in this case, the aerosol content, derived from the previous step exploiting the $O_4$ SCDs, is considered.

- *Retrieval of target species vertical profile.*

  At this step, the vertical profile of the target gas is retrieved. As in the first step, the process is iterative and starts with an a-priori profile. The retrieval uses the trace gas SCDs, estimated by QDOAS, as input. The process stops when the estimated vertical profile, combined with the BOX-AMFs simulated in the previous step, leads to SCDs equal, within a certain threshold, to the measured ones.

# Chapter 3

# MAX-DOAS instruments

A DOAS instrument is a spectrometer that measures atmospheric spectra in the VIS and UV spectral ranges. This kind of measurement can be performed in different ways (active or passive measurements, direct or diffuse solar measurements) and with instruments mounted in different platforms. In particular, the MAX-DOAS instruments are equipped with a moving telescope, linked via optical fiber to the spectrometer, in order to allow measurements at different elevation and azimuth angles. This chapter focuses on the three ground-based MAX-DOAS instruments used during this thesis: the TROPOspheric Gas Analyser Spectrometer (TROPOGAS), the GASCOD/NG4 and the SkySpec-2D. In particular, I exploited their measurements to create the first Italian FRM4DOAS-compliant MAX-DOAS site, to study the pollution around Lecce and to validate satellite data. While the SkySpec-2D is an instrument developed by Airyx GmbH (`https://airyx.de/wp-content/uploads/2021/03/SkySpec-all_2021-03-09.pdf`), TROPOGAS and GASCOD/NG4 are two research-grade custom-built systems developed in the 90s at CNR-ISAC.

## 3.1 SkySpec-2D

SkySpec-2D is a MAX-DOAS instrument developed by Airyx GmbH (`https://airyx.de/wp-content/uploads/2022/05/SkySpec-2D_v250.pdf`), fully compliant to the FRM4DOAS guidelines (see Table 1.1), which allows to measure VIS and UV fast and reliable atmospheric spectra. Its design allows to measure both direct and diffuse solar light at all the desired elevation angles and viewing directions.

### 3.1.1 Instrument description

The SkySpec-2D is made of three different components: the telescope, a box containing two spectrometers, and a pc needed to run the instrument.

#### Telescope

The telescope, shown in Figure 3.1, is the part of the instrument used to collect the incoming radiation and is the only part which can be placed outdoor.

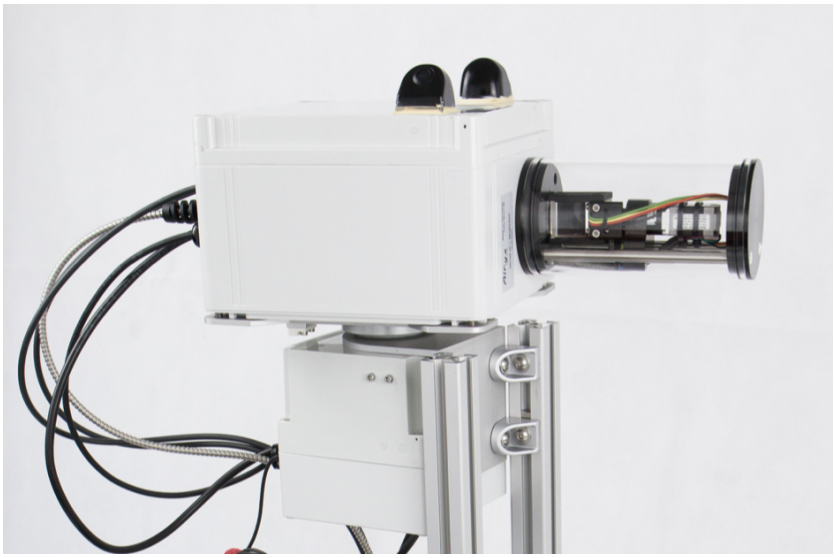

Figure 3.1: SkySpec-2D telescope.

It is made of a white box, where most of the electronics is contained, and a quartz cylindrical tube where the light is collected. The whole telescope can rotate thanks to a stepper motor which allows to cover azimuth angles from 0° to 180°. Another stepper motor, that allows to change the measurement elevation angle, rotating a prism from 0° to 180°, is present inside the quartz tube. When operated together, the rotating systems enable to acquire spectra, within a Field Of View (FOV) of about 0.3°, at every zenith and azimuth angle. In order to ensure a good quality of the pointing direction and to allow measurements also in not stable environments (for example ships), the rotating prism is also equipped with an elevation sensor that immediatly corrects its position, with an accuracy of 0.1°.

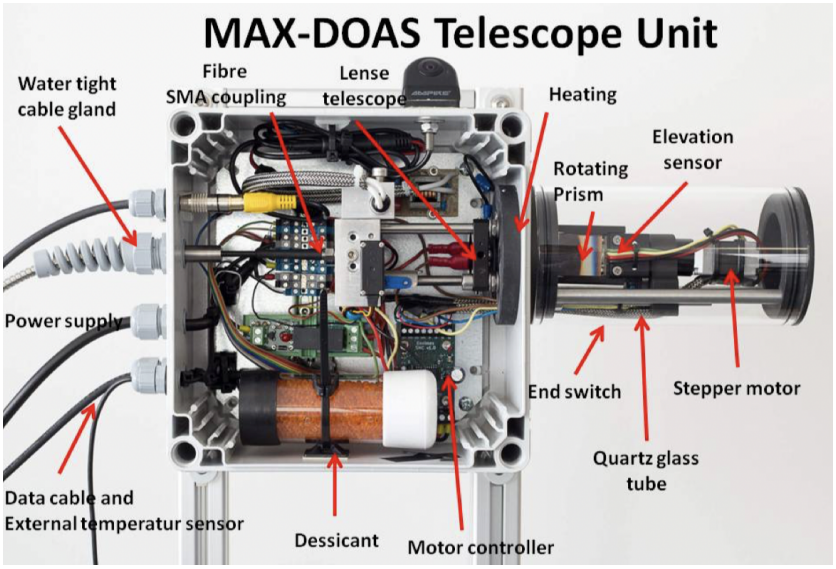


Figure 3.2: Components of the SkySpec-2D telescope.

In Figure 3.2, most of the telescope components are shown. The incoming radiation is reflected by the rotating prism to the lens and is propagated to the box, placed indoor, that contains the two spectrometers, through an optical fiber. The quartz tube is heated to prevent condensation on the optical components, which could affect the measurements quality. Information on the weather conditions is recorded by two cameras (not indicated in Figure 3.2), mounted on the top of the telescope, and a temperature and humidity sensor. Silica gel is placed inside the telescope to avoid high humidity in the electronic components. Moreover, a Mercury (Hg) lamp is integrated into the telescope to perform wavelength calibration measurements.

### Spectrometer

As alredy mentioned, the telescope is linked to the spectrometer box (see Figure 3.3), placed indoor, through an optical fiber. The box contains two spectrometers that are able to produce simultaneously, for a single measurement, two different spectra, one in the VIS (400-550 nm) and one in the UV (300-400 nm) spectral ranges, acquired with a spectral resolution of about 0.6 nm. Each spectrometer is equipped with a Charge-Coupled Device (CCD) sensor composed by 2048 pixels, where all the values that compose the spectrum are measured. Both the spectrometers are kept at a fixed temperature of 20° C, with deviations lower than 0.05° C, and are able to record spectra with an instrumental stray-light lower than 0.05% and a noise in the measured spectrum counts, estimated for a sum of 1000 spectra around noon,

of the order of $10^{-4}$. Since the spectrometers are sensitive to humidity, the only connection with the external air is through a tube filled with humidity absorbing silica gel to prevent the income of water vapor. This connection is necessary to compensate for changes in ambient pressure. To be sure that the air inside the box is dry and does not cause condensation on the spectrometers, a package of silica gel is also present within the spectrometer unit box.


Figure 3.3: SkySpec-2D spectrometer box.

### Laptop

A laptop, connected to the spectrometer box via an Universal Serial Bus (USB) cable, is used both to save the measurements and to drive the acquisition through the Measurement Software-DOAS (MS-DOAS). The MS-DOAS software, provided by Airyx GmbH, generates several windows that allow to interactively drive the SkySpec-2D (acquire measurements, change elevation and azimuth measurement angles and so on...) and to check if problems occur during the automatic acquisitions. Indeed, MS-DOAS gives also the possibility to create scripts, exploiting a list of existing commands, that allow to perform automatic MAX-DOAS measurements.

The MS-DOAS gives the possibility to save spectra computed as the sum of several single spectra, in order to increase the SNR. The number of co-added spectra represents the number of single spectra that are summed up in order to obtain the final saved spectrum. Both the total exposure time, which is the total time of the acquisition, and the single exposure time, which is

the time required to acquire a single spectrum, can be set by the user. From now on, we will always refer to the total exposure time as "total integration time" and to the measurement time of a single spectrum as "exposure time". It is possible and useful to make the MS-DOAS software automatically set the exposure time in order to prevent the saturation of the CCD sensor.

### 3.1.2 Acquired spectra

Each spectrum is saved into a binary file together with further useful information: the viewing elevation angle, the viewing azimuth angle, the number of co-added spectra, the exposure time and the total integration time. The viewing elevation and azimuth angles provide information on the telescope pointing direction. The number of co-added spectra, the exposure time and total integration time are not independent and provide information on the SNR of the spectrum.

The saved spectrum is measured in counts for each pixel of the CCD sensor. For this reason, it will need to be calibrated both in wavelength and in counts a-posteriori.

### 3.1.3 Spectra processing

The measured spectra, saved in binary files, are then processed by a python tool, developed during this thesis. It reads the binary files, calibrates the spectra and writes them into Network Common Data Form (NetCDF) files, two for each day (one for VIS and one for UV). The calibration procedure exploits the calibration spectra that are measured every night, when atmospheric spectra cannot be acquired. The final NetCDF files are created according to the FRM4DOAS standard guidelines (`https://frm4doas.aeronomie.be/ProjectDir/L1_format_20220407_v3.14d.pdf`). The python tool processes one day of measurements at a time and repeats all the following procedures for each day.

- *Spectral calibration*

  The spectra are calibrated in wavelength using Hg spectra, that are acquired automatically during the night. The Hg lamp is useful to perform spectral calibrations because produces flat spectra with high emission peaks at well-known wavelengths, as shown in Figures 3.4 and 3.5 in the UV and VIS, respectively. Since not even the Hg spectra are calibrated, they are shown in Counts with respect to the 2048 pixels of the CCD sensor.

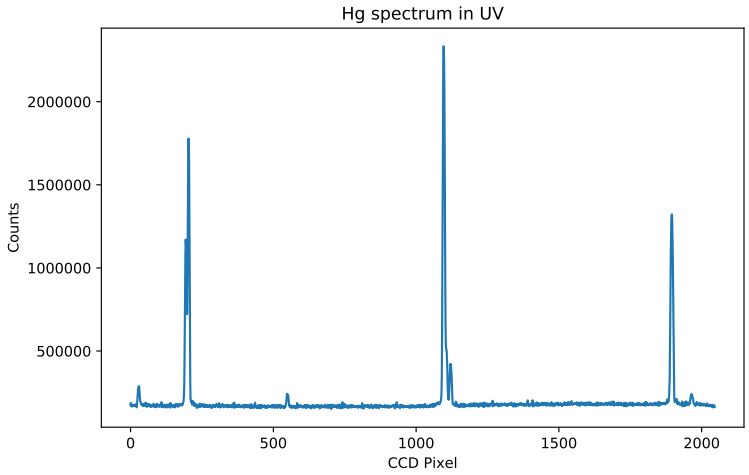


Figure 3.4: Hg lamp spectrum in the UV acquired with a total integration time of 60 s, exposure time of 0.35 s and 167 co-added spectra during the night on 10 February 2022.

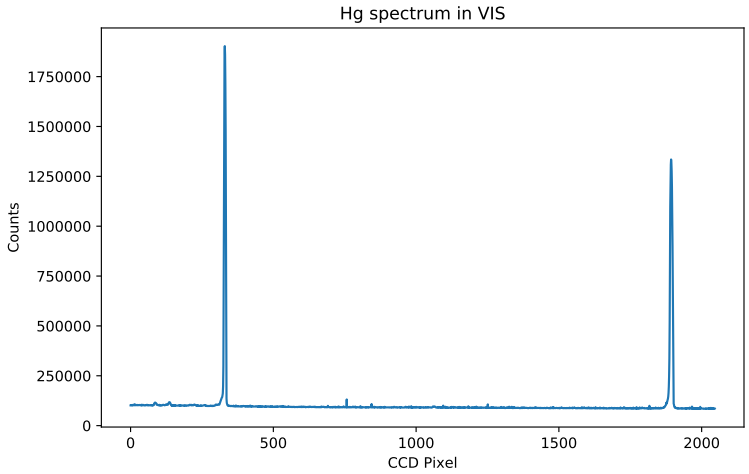


Figure 3.5: Hg lamp spectrum in the VIS acquired with a total integration time of 60 s, exposure time of 0.28 s and 214 co-added spectra during the night on 10 February 2022.

The spectral calibration consists of creating a mathematical relation which links each pixel of the CCD sensor to a wavelength value; in particular, the relation is not linear and we approximate it with, at

least, a 2-degree polynomial. In order to do that, we need to measure at least three emission peaks, located at known wavelengths, that are used to fit the polynomial coefficients. In the case of UV spectra, the spectral calibration is performed using a 3-degree polynomial relation because four high emission peaks are present (see Figure 3.4) at the wavelengths of 312.6, 313.1, 365.0, 404.7 nm.

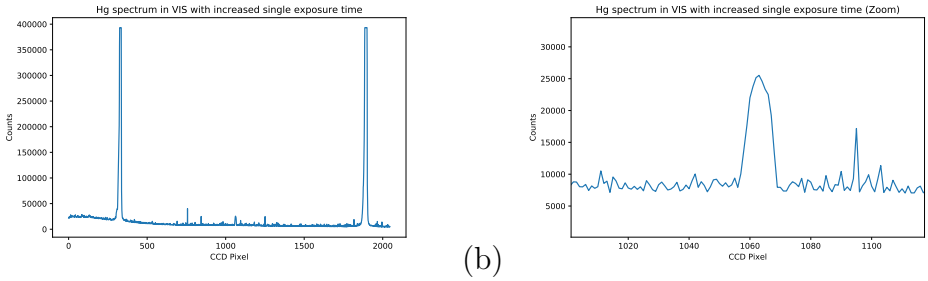


(a) (b)

Figure 3.6: Hg lamp spectrum in the VIS (a) and its zoom (b) acquired with a total integration time of 60 s, exposure time of 10 s and 6 co-added spectra during the night on 10 February 2022.

A different story is the calibration of the VIS spectra, since, as shown in Figure 3.5, only two high Hg emission peaks are present. In reality, one less intense emission peak, that can be detected increasing the exposure time, is present in the VIS. Figure 3.6a shows the Hg emission spectrum in the VIS acquired with an exposure time of 10 s. The two high peaks are saturated and a third low peak starts to be detectable around the pixel 1060, more visible in the zoom in Figure 3.6b. Therefore, the three peaks needed to calibrate the spectra in the VIS must be obtained from two different Hg lamp measurements, acquired with different exposure times. These three peaks occur at the known wavelengths of 435.8, 491.6, 546.0 nm.

- *Counts calibration*

  All the other calibration measurements, performed during the night, are used to correct the counts of the spectra. Indeed, although the DOAS method does not require the spectra to be radiometrically calibrated, some instrumental effects must be corrected. In particular, the offset and dark current must be removed from the measured spectra and the effect of the sensors' non-linearity must be corrected. The sum of offset and dark current is present in every measured spectrum and represents the number of counts generated by the detector when the sensor is not illuminated.

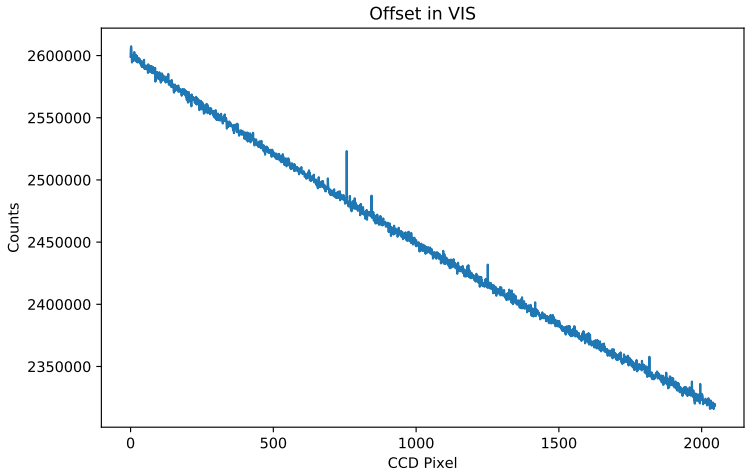


Figure 3.7: Offset spectrum in the VIS acquired with a total integration time of 60 s, exposure time of 0.01 s and 6000 co-added spectra during the night on 10 February 2022.

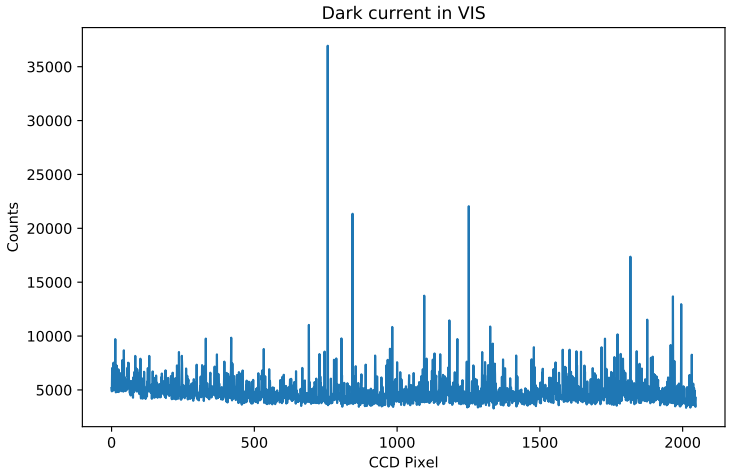


Figure 3.8: Dark current measurement in the VIS acquired with a total integration time of 60 s, exposure time of 10 s and 6 co-added spectra during the night on 10 February 2022. Since this is the measurement, it still contains the offset contribution.

The offset is a signal independent on the exposure time and is present in all the single spectra that are summed up to create the final saved

spectrum. The dark current, present in all the single spectra, is not constant but it linearly increases with the exposure time. The offset and dark current are measured during the night preventing light from reaching the sensor. In particular, the offset is measured with a very low exposure time to make the dark current contribution negligible. On the other hand, since the dark current depends on the exposure time, that is always different, it cannot be directly measured. Therefore, a dark spectrum is measured with a high exposure time and the offset, previously estimated, is removed. Since the dark current increases linearly with the exposure time, the measured value is scaled, according to the exposure time of the considered atmospheric spectrum and then removed. Examples of offset and dark current spectra in the VIS are provided in Figures 3.7 and 3.8.

The offset and dark current are removed from the measured Hg spectra too. The sensor non-linearity does not need to be routinely measured because it is a sensor's feature, represented by a 5-degree polynomial. The two sets of polynomial's coefficients, one for VIS and the other for UV sensors, are provided by the Airyx company. During the calibration procedure, it must be considered that the number of the co-added spectra in the measured calibration spectra is not equal to the number of co-added spectra relative to the atmopsheric spectrum considered. For this reason, we apply all the corrections to every single spectrum after properly scaling the calibration spectra. At the beginning, the constant offset is subtracted; then, the spectra values are corrected for the non-linearity (which depends on the spectrum values). In the end, the dark current signal, properly scaled for the exposure time of the atmospheric spectrum and corrected for the non-linearity, is subtracted from the atmospheric spectrum.

- *NetCDF file creation*

  All the calibrated spectra and relative information acquired in a day are saved into two NetCDF files (one for the VIS and the other for the UV channels). The name of these NetCDF files follows the FRM4DOAS naming convention and contains the affiliation, the location of the station, a unique identification number provided by the FRM4DOAS community, the information of the VIS channel (1, 2 is for UV), the day and UTC time for the start and the end of atmospheric measurements, and the version. An example of NetCDF file, containing VIS spectra acquired in San Pietro Capofiume (SPC) on 30 June 2022, is "$ESA-FRM4DOAS-L1-CNR.ISAC-SAN.PIETRO.CAPOFIUME-$

$1695 - 1 - 20220630T030848Z - 20220630T192541Z - fv001.nc$".

## 3.2 TROPOGAS

In this section, the TROPOGAS description and characterization are provided. TROPOGAS is a research-grade custom-built instrument developed at the CNR-ISAC and installed on the roof of the CNR-ISAC, in Bologna, since 2018. During this thesis, I exploited its spectra for a measurement campaign, described in Section 5.2.2, with the purpose to assess the SkySpec-2D's performances.

I avoid to describe in detail the TROPOGAS spectra processing because the adopted approach is very similar to the one already explained in Section 3.1.3.

### 3.2.1 Instrument description

TROPOGAS measures zenith and off-axis atmospheric scattered spectra with a spectral resolution of about 0.4 nm in the UV and 0.5 nm in the VIS on the roof of the CNR-ISAC, in Bologna, since 2018. Differently from SkySpec-2D, it can measure one spectrum at a time in a customizable spectral range contained from 300 and 600 nm. As SkySpec-2D, TROPOGAS is made of three different components: the telescope, the spectrometer and the computer. In the core of the spectrometer (Figure 3.9b), the radiation is measured by a cooled (at -20°C to reduce the thermal noise and dark current) CCD sensor. The CCD sensor is a matrix of 7 x 1024 pixels. Each spectrum is simultaneously recorded in the seven arrays (bins) made of 1024 pixels, each of them representing a wavelength. The TROPOGAS spectrometer is coupled with an Alt-Azimuth platform (Figure 3.9a), developed and implemented at CNR-ISAC in collaboration with the Evora University, with an optical fiber, and it is used for off-axis and zenith-sky measurements of diffuse solar radiation. The Alt-Azimuth platform is a small telescope with a mirror lens and both azimuth and zenith movements. The computer (Figure 3.9b) drives the instrument for the spectra acquisition. Every acquired spectrum is the average of a fixed number of 36 spectra, each of them acquired with the same exposure time, from 0 to 3 s, automatically estimated to prevent the saturation of the CCD sensor. Its design will not be explained in detailed because is similar to the SkySpec-2D's one. Anyway, more details on the system can be found in [47].

(a) 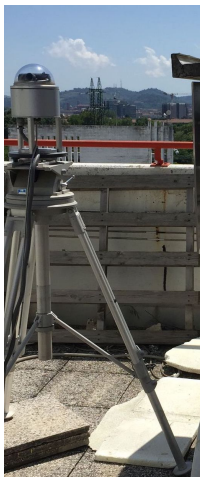 (b) 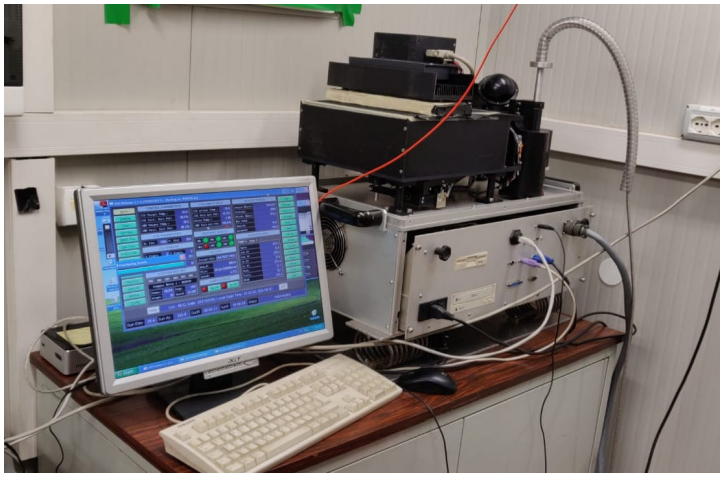

Figure 3.9: Telescope (a) and spectrometer and computer (b) of the TROPOGAS, installed on the roof of the CNR-ISAC in Bologna.

### 3.2.2 Characterization

In the frame of an ESA project, TROPOGAS was initially supposed to become the first ground-based MAX-DOAS instrument, in Italy, compliant to the FRM4DOAS requirements. For this reason, I performed a full characterization of TROPOGAS to assess if it could meet all the FRM4DOAS guidelines. While the acquisition and processing guidelines are easily met updating its measurement and analysis strategy, other instrumental features, such as the SNR and the FOV dimension, needed to be assessed. Indeed, since TROPOGAS is a custom-built instrument, many technical features were not reported.

#### SNR assessment

For the SNR assessment, I decided to use a quartz-iodine lamp, mounted inside TROPOGAS, which has the feature to emit very smooth spectra. I measured 50 quartz-iodine spectra with the same exposure time, so that the differences among them were only due to the noise. However, I realized that, for reasons not clear yet, not null systematic differences sometimes exist. For this reason, I decided to compute a running average over 15 points of the wavelength grid and subtract it to each spectrum in order to obtain 50 spectra having zero mean. At first, I computed the mean noise of the whole spectrum with respect to the number of averaged spectra. For this goal, I averaged a fixed number of zero-mean spectra from two different spectra datasets. Then, I computed the difference between them, in order to remove

the residual systematic oscillations, due to the high spectral variability. I estimated the mean noise, related to a certain number of averaged spectra, as the standard deviation of this difference.

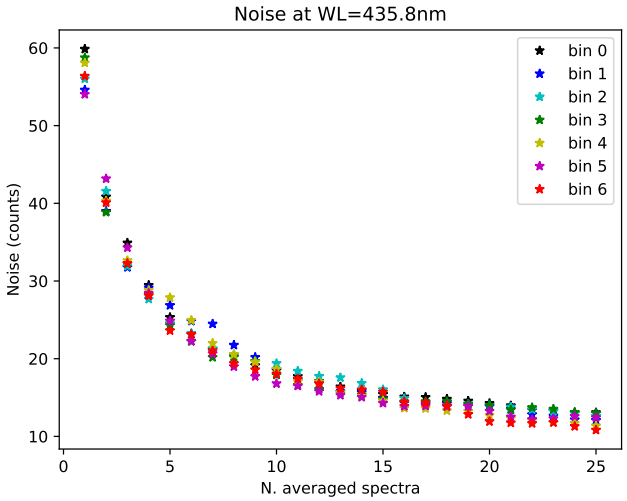


Figure 3.10: Estimated noise in the spectral band centered at 435.8 nm with respect to the number of the averaged spectra, for all the 7 bins of the CCD sensor.

Figure 3.10 shows the estimated mean noise of a spectrum with respect to the number of the averaged spectra and for all the 7 bins that compose the CCD sensor. It is clear that the noise decreases with the square root of the number of averaged measurements, as it should be.

At the end, I also computed the noise, of a not-averaged spectrum, as a function of the spectrum values, measured in counts. For each spectral point (each wavelength), I estimated the noise as the standard deviation of all the same points of the 50 zero-mean spectra. Figures 3.11 and 3.12 show the noise and SNR, respectively, as a function of the spectrum counts. According to the results, although the noise increases with the counts, it rises slower than the counts themselves, leading to an increase of the SNR with the counts. This means that the convenient exposure time to measure a spectrum is the one that leads to high counts without reaching the saturation of the CCD sensor, which corresponds to 65,535 counts. Considering that the minimum SNR in the visible, required by FRM4DOAS, is 3,000, and assuming to be able to measure the spectra with counts higher than 30,000, the minimum SNR in a single spectrum is about 500, as shown in Figure 3.12. Since the SNR increases with the square root of the averaged spectra, I decided to

update the measurement strategy averaging 36 single spectra for each saved final spectrum. In this way, the SNR of every saved spectrum will be about 3,000.

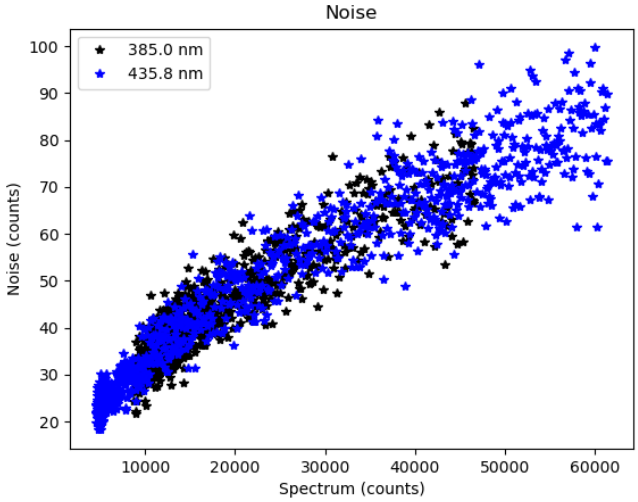


Figure 3.11: Estimated noise in the spectral band centered at 435.8 and 385 nm with respect to spectrum values (counts).

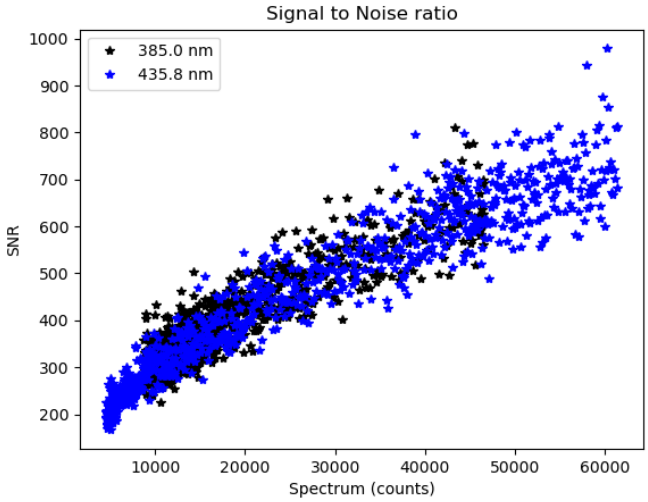


Figure 3.12: Estimated SNR in the spectral band centered at 435.8 and 385 nm with respect to spectrum values (counts).

### FOV assessment

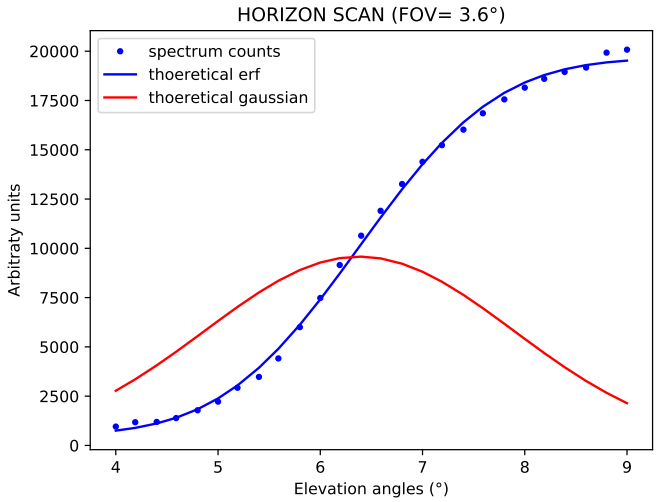


Figure 3.13: Horizon scan used to estimate the TROPOGAS FOV. The blue dots represent the signals, in arbitrary unit, measured at 440 nm for different elevation angles. The blue line is the error function (ERF) used to fit the data. The red line is a Gaussian and represents the derivative of the ERF function (blue line). Its FWHM is used to estimate the FOV, reported in the title.

The FOV has been estimated performing some horizon scans. In particular, I measured the signals at 440 nm for different elevation angles close to the horizon. I chose a clear day so that a strong contrast between land and sky was present.

The blue dots in Figure 3.13 represent the signals, in arbitrary unit, measured at 440 nm for different elevation angles. It is evident that the signal is low for low elevation angles, when only land is detected by the instrumental FOV. Increasing the elevation angle, part of the FOV starts to cross the sky and the signal increases until the elevation angle is big enough and all the signal reaching the FOV comes from the sky. The blue dots are fitted by the function $S$ (blue line):

$$S = A[ERF((x - x_0)/B) + 1] + C \tag{3.1}$$

where $ERF$ is the error function, the integral function of a Gaussian curve, and $A$,$B$,$C$ and $x_0$ are fitted parameters. The Gaussian curve, derivative of equation 3.1 is plotted in red. Its Full Width at Half Maximum

(FWHM) is the FOV estimate and is computed as:

$$FWHM = 2\sqrt{ln(2)}B \tag{3.2}$$

The estimated TROPOGAS FOV is 3.6°. Since the FOV required by FRM4DOAS standard is 1.5°, TROPOGAS does not meet this requirement. This is one of the reasons why my colleagues and I chose to exploit SkySpec-2D to create the first MAX-DOAS site, compliant to the FRM4DOAS standards, in Italy. This work will be illustrated in Chapter 5.

## 3.3 GASCOD/NG4

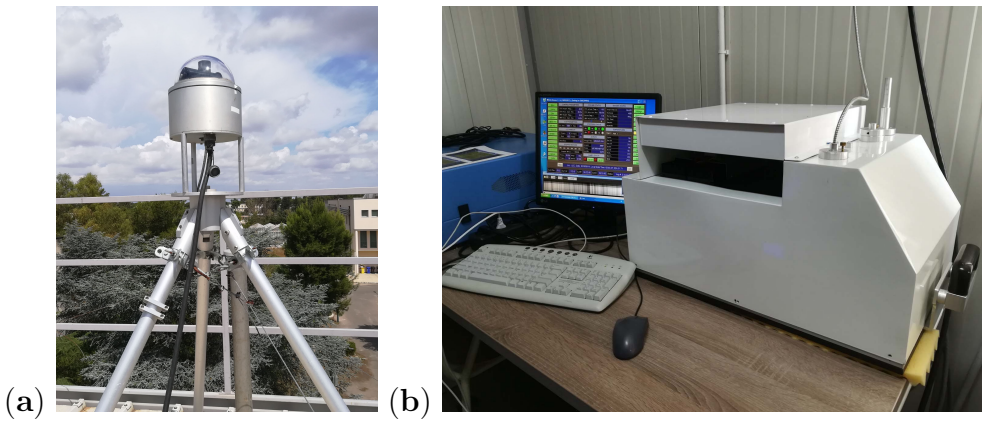

(**a**) (**b**)

Figure 3.14: Telescope (a) and spectrometer and computer (b) of the GASCOD/NG4, installed at the ECO observatory at the CNR-ISAC in Lecce.

The GASCOD/NG4 instrument (Figure 3.14) is part of the GASCOD family [48]. This series of instruments was initially developed at CNR-ISAC in the early 90s and improved over the years in collaboration with the University of Evora (Portugal) [26]. Its functioning and design are similar to TROPOGAS, described in Section 3.2. Indeed, also GASCOD/NG4 can measure one spectrum at a time in a customizable spectral range between 300 and 800 nm and with a mean spectral resolution of 0.5 nm. A detailed description of the mechanical and electronic components together with the adopted optical layout and the explanation of the measurement principles adopted in the most recent versions of these instruments is available in [26, 49].

In the frame of the Infrastruttura di Alta tecnologia per il Monitoraggio Integrato Climatico-Ambientale (I-AMICA) project (`http://www.i-amica.it`), since 2016 the meteo-climatic ECO observatory in Lecce (Italy) was

equipped with the GASCOD/NG4 for the measurement of zenith and off-axis diffuse solar spectra. The ECO observatory (40.34°N 18.12°E; 36 m a.s.l.) is located about 4 km (W-SW) from the urban area (about 95,000 inhabitants), about 10 km from the South Adriatic sea and can be classified as an "urban background" site [50, 51]. The site is located about 30 and 80 km from the two most important industrial centers of the Apulia Region (Brindisi and Taranto, respectively). The ECO observatory is a regional station of the Global Atmospheric Watch (GAW) network [52]. The spectrometer was located on a shelter on the roof of the CNR-ISAC building, 12 m above the street, inside the university campus. At the ECO observatory, detailed ancillary meteorological data (wind characteristics, temperature, relative humidity and pressure) and in-situ $NO_2$ and $O_3$ concentrations are measured by an automatic weather station (Vaisala WXT520), located 20 m above the ground, and a gas analyzer described in [52], respectively.

# Chapter 4

# Analysis of $NO_2$ and $O_3$ total columns over Lecce

This chapter is based on the following paper: Pettinari P., Donateo A., Papandrea E., Bortoli D., Pappaccogli G. and Castelli E.: Analysis of $NO_2$ and $O_3$ Total Columns from DOAS Zenith-Sky Measurements in South Italy, Remote Sensing, 2022, 14, 5541.

*This study was performed thanks to all the coauthors. Daniele Bortoli developed the GASCOD/NG4 system, the instrument used to measure the zenith-sky spectra for the retrieval of the $NO_2$ and $O_3$ VCDs. He also wrote the instrument description. Antonio Donateo and Gianluca Pappaccogli provided the DOAS spectra and all the ancillary data (meteorological and in situ $NO_2$ and $O_3$ concentrations) used in this study. Moreover, they described the ECO measurement site at the CNR-ISAC of Lecce (Italy), where the measurements took place. Elisa Castelli, Enzo Papandrea and I performed most of the analysis and writing work. In particular, I set up the DOAS analysis to retrieve $NO_2$ and $O_3$ SCDs and VCDs and performed the investigation presented in the results. Elisa Castelli filtered out the data heavily affected by aerosol and clouds, wrote the section describing the filtering method and helped during the investigation. Enzo Papandrea provided the overpasses data of TROPOMI and Ozone Monitoring Instrument (OMI) satellites over ECO observatory, he wrote the section describing the criteria used for the comparison with satellite data and he helped during the investigation. All the coauthors revised the paper before its publication and contributed to its final form.*

Two of the most important trace gases for atmospheric chemistry and physics are nitrogen dioxide ($NO_2$) and ozone ($O_3$). Since they are important pollutants in urban areas, investigations on them have been carried out worldwide, focusing on their temporal development and interrelations with chemical mechanisms. In this chapter, the $NO_2$ and $O_3$ total VCDs retrieved from zenith-sky spectra acquired by the MAX-DOAS instrument GASCOD/NG4 (described in Section 3.3), located at the ECO observatory of the CNR-ISAC, near Lecce, are presented. The analysis of the total VCDs, in synergy with in-situ data, allowed to assess with a high level of detail the potential of this observatory, which is part of the GAW program.

## 4.1 Retrieval strategy

The first step consisted in fitting the SCDs from the measured zenith spectra with the QDOAS software, described in section 2.3. Then, the total VCDs were calculated by dividing the SCDs, corrected for the absorption present in the reference spectrum, by the corresponding AMFs simulated by the SCIATRAN RTM, as described in section 2.4. After the filtering process, the results of our analysis provided a total of 81,310 $NO_2$ and $O_3$ total VCDs retrieved in 592 days between March 2017 and November 2019. On average, 137 total VCDs have been retrieved each day.

### 4.1.1 SCDs fit

Zenith-sky spectra, acquired by the GASCOD/NG4, were analyzed by the QDOAS software in order to retrieve the $O_3$, $NO_2$ and tetraoxygen ($O_4$) SCDs. The automatic acquisition system of GASCOD/NG4 acquires the spectra in different spectral windows and continuously during the day. The system saves the data into binary files containing, for each spectrum, the information regarding the measured spectral range, day and time of acquisition and SZA. Those files are pre-processed to spectrally calibrate the measurements and to make them compliant with the QDOAS input file format. The analysis reported in this work was performed in the spectral interval 470-510 nm, exploiting the spectra acquired in the spectral window centered at 486 nm (see Figure 4.1). In this spectral region, absorption features of $NO_2$, $O_3$ and $O_4$ are present. $O_4$ SCDs are essential because they can be used to detect aerosol and clouds that can alter the $NO_2$ and $O_3$ SCDs.

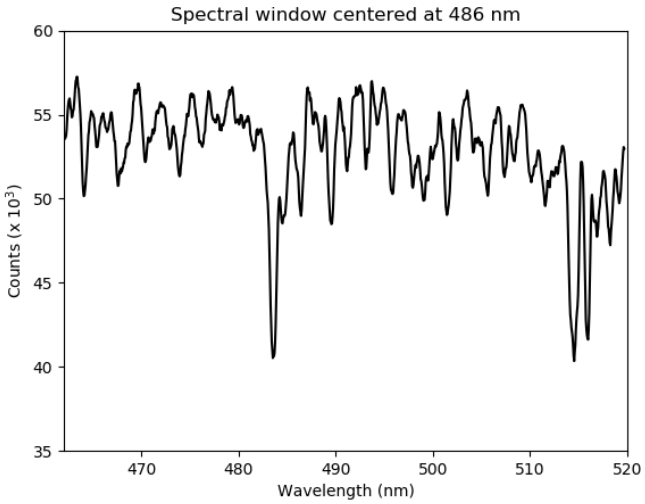


Figure 4.1: Zenith spectrum acquired at 11:27 UTC of 27 November 2018 by GASCOD/NG4 in the spectral window centered at 486 nm in counts. It was not radiometrically calibrated, since the DOAS analysis does not require it.

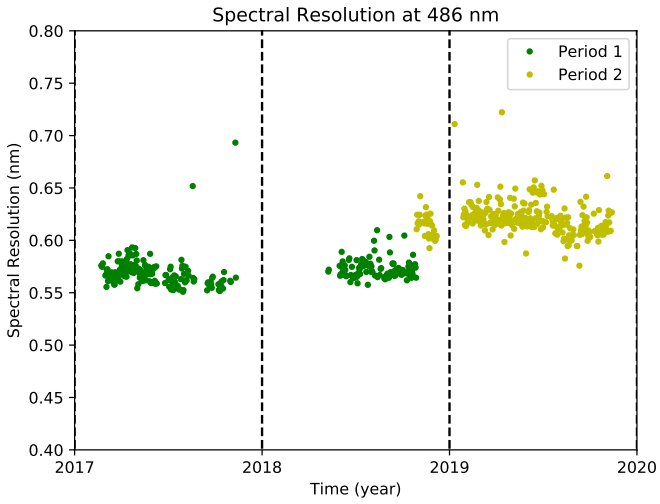


Figure 4.2: Instrument's spectral resolution in the spectral window centered at 486 nm and for all the measurement period. Each color identifies a period characterized by a time-constant spectral resolution.

The QDOAS settings used for the analysis follow as much as possible the FRM4DOAS community requirements. At first, all the spectra were an-

alyzed with a fixed reference spectrum. However, I realized that, due to several maintenance interventions voted to improve the instrument performance (high SNR), the dispersion parameters, applied to the spectral images reaching the CCD sensor, slightly changed, resulting in the modification of the GASCOD/NG4 spectral resolution (see Figure 4.2).

The spectral resolution was evaluated by QDOAS during the automatic calibration procedure. The differential method at the basis of the DOAS technique requires the spectral resolutions of reference and analyzed spectra to be as similar as possible.

Hence, I decided to divide the analysis into two different periods (see the colours in Figure 4.2), each of them with a fixed reference spectrum, as reported in Table 4.1.

Table 4.1: Reference spectra in the two different periods used for QDOAS analysis. The method to estimate the $NO_2$ and $O_3$ contributions contained in the reference spectra will be explained in section 4.1.3

| **Period** | beginning-28/10/2018 | 29/10/2018-end |
|---|---|---|
| **Day ref.** | 06/07/2017 | 11/07/2019 |
| **SZA ref.** | 17.62° | 18.13° |
| **$NO_2$ Ref. (molec/cm$^2$)** | $4.3\times10^{15}$ | $6.1\times10^{15}$ |
| **$O_3$ Ref. (molec/cm$^2$)** | $7.1\times10^{18}$ | $1.3\times10^{19}$ |

QDOAS gives also the possibility of performing the analysis with respect to daily reference spectra, automatically selected around noon time. However, I decided to use only two fixed reference spectra for two main reasons:

- The use of daily reference spectra would have introduced daily biases in the retrieved total VCDs, due to the uncertainty in the knowledge of the true contributions of the reference spectra. According to the adopted methodology, I expected biases only between the two analysis periods.

- The two fixed reference spectra, acquired in summer at noon, are affected by a minimum gas absorption due to the almost vertical position of the sun.

Table 4.2: Main QDOAS settings used for $NO_2$ and $O_3$ SCDs analysis.

| | |
|---|---|
| **Wavelength Range** | 470–510 nm |
| **Polynomial** | Order 3 |
| **Offset** | Constant |
| **Cross sections** | |
| $NO_2$(220 K) | from [53]. $I_0$ correction ($10^{17}$) applied |
| $NO_2$(294 K) | from [53]. Orthogonalized to $NO_2$ (220 K) with $I_0$ correction ($10^{17}$) |
| $O_3$(223 K) | from [54]. $I_0$ correction ($10^{20}$) applied |
| $O_3$(293 K) | from [54]. Orthogonalized to $O_3$ (223 K) with $I_0$ correction ($10^{20}$) |
| $O_4$(293 K) | from [55] |
| $H_2O$(298 K) | from [55] |
| Ring | Generated according to [40, 41], using the solar atlas in [42] |

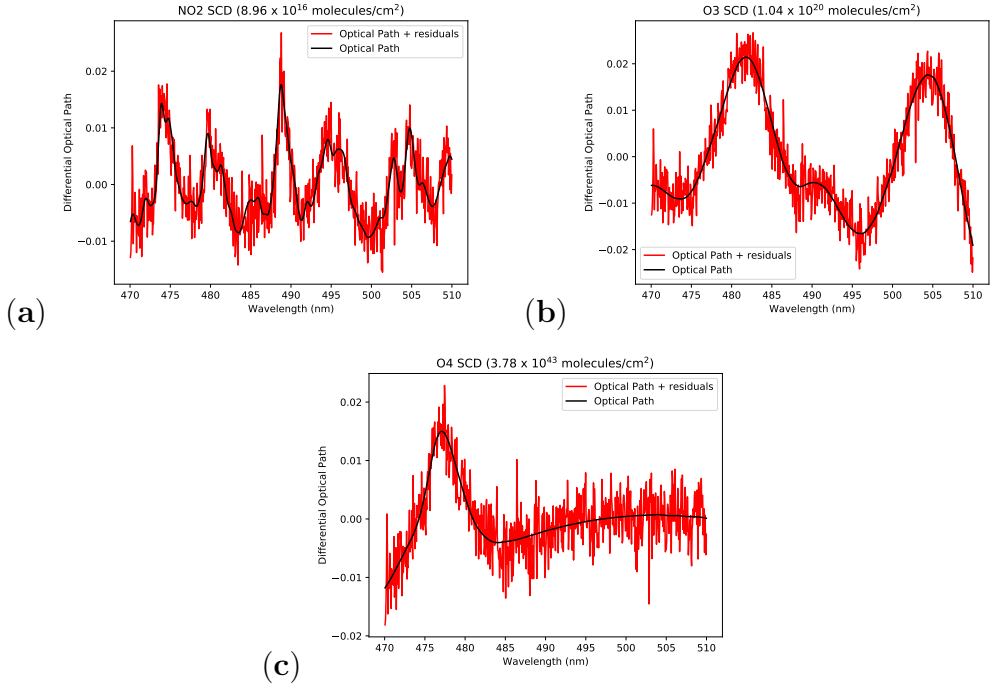


Figure 4.3: Examples of differential optical paths due to $NO_2$ (**a**), $O_3$ (**b**) and $O_4$ (**c**) absorption, fitted by QDOAS for a spectrum acquired on 6 July 2017 at 19:11 UTC when the SZA was 89.3°. SCDs values are reported in the plots' titles.

All the other analysis settings are reported in Table 4.2. A constant offset between the analyzed and reference spectra and an order-3 polynomial were fitted simultaneously with $NO_2$, $O_3$, $O_4$ and $H_2O$ absorption cross-sections. The ring effect is considered as an additional cross-section, as described in

section 2.3. Since $NO_2$ and $O_3$ cross-sections depend on temperature, the absorption signature for each of the gases was fitted by two cross-sections at different temperatures. Moreover, $NO_2$ and $O_3$ theoretical cross-sections were corrected applying the $I_0$ correction mentioned in section 2.2, as suggested in [37] .

An example of the differential optical paths, due to the $NO_2$, $O_3$ and $O_4$ absorption, fitted by QDOAS, is reported in Figure 4.3. In this case, the $NO_2$, $O_3$ and $O_4$ spectral signatures are well defined compared to the fit residuals because the path crossed by the radiation in the analyzed spectrum (measured at a high solar zenith angle) is much longer than the one relative to the reference spectrum (measured with a low solar zenith angle; see Table 4.1).

Before calculating the total VCDs, the SCDs retrieved by QDOAS were filtered twice: first, SCDs were filtered out based on the QDOAS flag that certified whether the fit was successful and on the $\chi^2$ of the fit. Then, a second filter was applied to exclude data heavily contaminated by clouds. The remaining SCDs were then processed to compute the total VCDs.

### 4.1.2 Clouds and aerosol data filtering

Since SCDs are path-integrated quantities, variations in the light path due to scattering by particles produce biased SCDs and, thus, VCDs. However, as demonstrated by [46], $O_4$ SCDs can be used to infer information on particles' optical depths and vertical distribution. The $O_4$ concentration in the atmosphere is well-known (its absorption is proportional to the square of the partial pressure of molecular oxygen) and constant. $O_4$ SCDs variations depend on the light path, and its behavior as a function of SZA is thus known. Variations in this behavior from the expected one are proxies of particle presence. In this study, we used $O_4$ SCDs to filter clouds/aerosol-contaminated measurements. The $O_4$ SCDs' behavior with respect to SZA can be modeled using a RTM, e.g., SCIATRAN. However, in several cases, as reported in [56], the simulated $O_4$ SCDs can differ (as a bias and not in the behavior) from the measured ones. For this reason, to filter the data, we decided to use only the measured $O_4$ SCDs. The data were used to build histograms, binning the $O_4$ SCDs in 2°-wide SZA bins. For each SZA bin, data falling outside 90% of the maximum frequency were filtered out. It should be mentioned that, using this filtering procedure, particle-contaminated spectra may still be present. Indeed, this method aims at filtering only spectra heavily contaminated by particles to remove strong oscillations from the final dataset. The $O_3$ and $NO_2$ SCDs identified as particle-contaminated were removed from the subsequent analysis. In the end, a total of 16.6% of the measurements were filtered

out.

### 4.1.3 Reference contributions

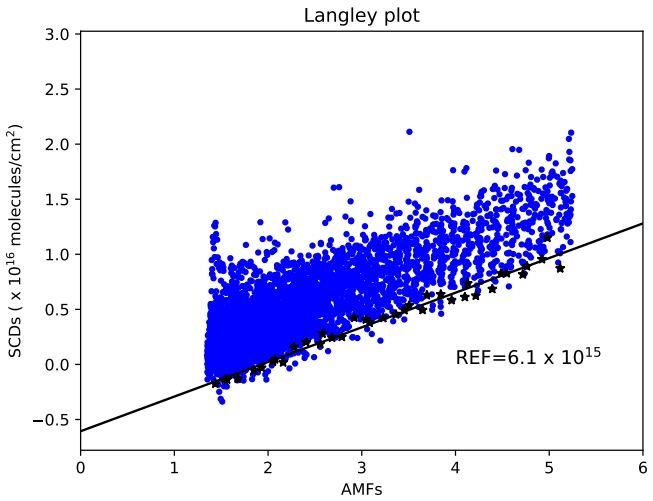


Figure 4.4: Langley plot used to estimate the contribution of the reference spectrum acquired at 11 July 2019 to the $NO_2$ SCDs. The blue dots are all the $NO_2$ SCDs relative to March 2019. Black stars are the low SCDs, fitted by the black line, which were used to estimate the intercept.

Since the absorber amounts in the two reference spectra used for the QDOAS analysis cannot be considered negligible as they would be with spectra measured outside the atmosphere, the SCDs estimated by QDOAS must be corrected by adding the reference contributions that can be estimated using the Langley plot method [57]. According to it, the SCDs, retrieved for a certain period, were plotted against the simulated AMFs. In the hypothetical case that the true absorber total VCDs remain constant in time, the intercept of the line, which fits the SCDs, represents the reference contribution, and the slope represents the constant total VCD value related to the observed SCDs. However, the assumption of a constant vertical content is not easy to satisfy, especially close to an urban area, such as the ECO measurement site. For this reason, we assumed that, in a Langley plot, the lowest SCDs over a certain period refer to the same minimum vertical content, when the contribution comes mainly from the stratosphere. This means that the minimum SCDs can be linearly fitted in order to estimate the intercept, as reported in

Figure 4.4. The $NO_2$ and $O_3$ estimated SCDs in the two selected reference spectra are reported in Table 4.1.

### 4.1.4 Systematic errors affecting the total VCDs' diurnal variability

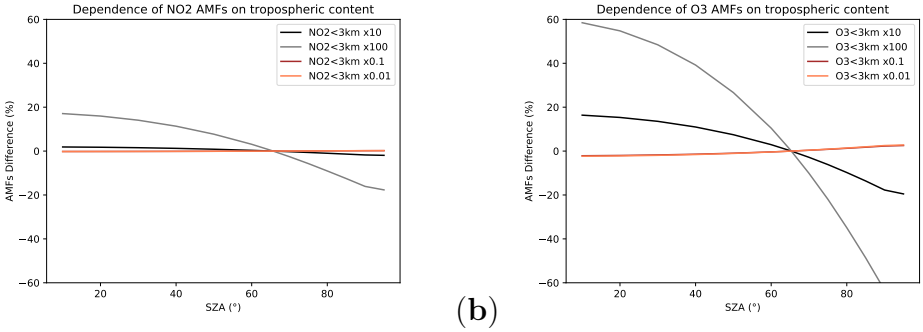


(**a**) (**b**)

Figure 4.5: Percentage differences between AMFs computed using perturbed input profiles and standard profiles, for $NO_2$ (a) and $O_3$ (b). The AMFs simulated with standard profiles were the ones used to convert the SCDs into total VCDs.

The estimate of the diurnal variability of trace gases total VCDs derived from zenith-sky DOAS measurements is a hard task because the systematic errors, mainly in the estimated reference contributions and in the simulated AMFs, have a not-negligible impact. The errors in the $NO_2$ and $O_3$ reference contributions were estimated as $2x10^{15}$ and $2x10^{18}$ molecules/cm$^2$, respectively. These values were computed as the spread coming from reference estimates performed considering different periods. This error has a higher impact on the retrieved total VCDs relative to low AMFs (around noon) than the ones with high AMFs (sunrise or sunset). This artifact contributes to create a not-real diurnal variability in the total VCDs. For this reason, the assessment of the reference contributions, discussed in Section 4.1.3, is a sensitive part of the analysis. The errors in the simulated AMFs lead to a similar problem. Actually, the input parameter which most affects the simulated AMFs is the vertical profile of the target gas used in the RTM. This effect can be seen in Figure 4.5a for $NO_2$ and Figure 4.5b for $O_3$, where the percentage differences between AMFs simulated with modified input profiles and standard profiles (the input for simulating the used AMFs) are plotted against the SZA. The changes in the input profiles were obtained by increasing (multiplying to 10 or 100) or decreasing (dividing by 10 or 100) the tropospheric contents below

3 km. The plots show that the AMFs did not change significantly when $NO_2$ and $O_3$ tropospheric contents were decreased. This means that the tropospheric content in the used profiles is low, and the relative AMFs are mainly representative of the stratosphere. On the other hand, an increase in the tropospheric content led to important differences in the AMFs. In particular, the AMFs changed differently for low and high SZAs, contributing to create a not-real diurnal variation in the total VCDs. Since this effect can heavily affect the diurnal behavior of $NO_2$ and $O_3$ total VCDs, I tried to make some considerations for the diurnal variabilities without focusing on the absolute values.

## 4.2 Results

### 4.2.1 Diurnal variability

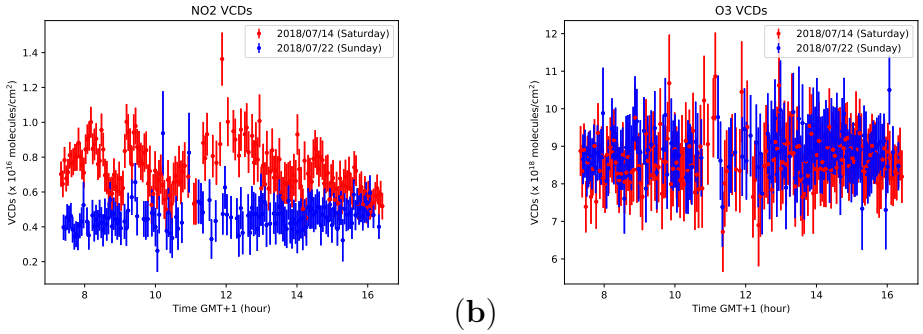


(a) (b)

Figure 4.6: $NO_2$ (a) and $O_3$ (b) total VCDs during the days 2018/07/14 (red) and 2018/07/22 (blue). The error bars represent the total VCDs random errors derived from the SCDs fitted by QDOAS.

Although, as mentioned in Section 4.1.4, the $NO_2$ and $O_3$ diurnal trends are affected by important systematic errors, Figure 4.6a clearly shows that significant day-to-day differences in the $NO_2$ total VCDs exist. In particular, it is evident how the $NO_2$ total VCDs were higher and less constant on 14 July 2018 (Saturday) with respect to 22 July 2018 (Sunday), when the traffic was generally lower. This result highlights the clear presence of the tropospheric contribution to the retrieved $NO_2$ total VCDs. On the other hand, the $O_3$ total VCDs retrieved in the same two days were not affected by any significant difference (see Figure 4.6b), suggesting that the $O_3$ total VCDs are less sensitive to the tropospheric variability. These first considerations will be further demonstrated in Sections 4.2.2 and 4.2.3.

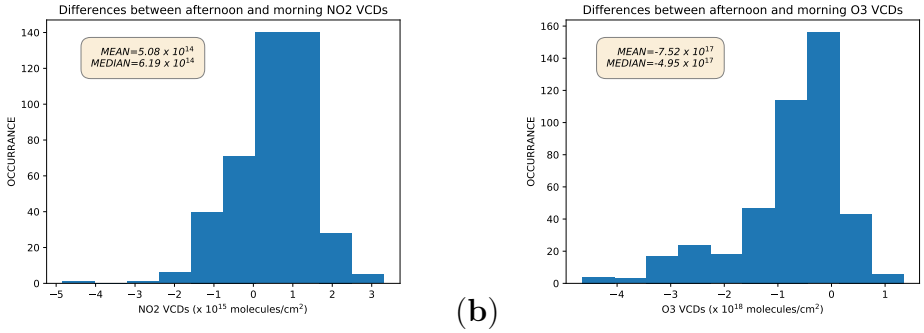


(**a**) (**b**)

Figure 4.7: Histogram of the differences computed as $NO_2$ (a) and $O_3$ (b) total VCDs in the afternoon minus the total VCDs in the morning. For each day, the total VCDs representative of morning and afternoon were computed as the mean total VCDs in the SZA range between 60° and 90°.

In Figure 4.7a, we can see that, for most days, the $NO_2$ total VCDs in the afternoon are higher than the ones in the morning; the median and mean differences are 6.2x$10^{14}$ and 5.1x$10^{14}$ molecules/cm$^2$, respectively. These differences were computed as the mean $NO_2$ total VCDs in the SZA range between 60° and 90° in the afternoon minus the same quantity in the morning. The same fixed SZA range, used to compute the mean total VCDs in the morning and afternoon, avoids the results being affected by the systematic effects, due to the AMFs, as discussed in Section 4.1.4. This diurnal increase is in agreement with the stratospheric chemical processes that involve $NO_2$, where, during daytime, $N_2O_5$ is photolyzed into $NO_2$ and $NO_3$. A slight and linear diurnal increase in $NO_2$ total VCDs is indeed found in not-polluted areas, such as over Table Mountain, California, from direct solar spectra [57], and in Zugspitze, Germany, from solar Fourier Transform Infra-Red (FTIR) measurements [58]. Thus, this analysis suggests that the diurnal variability of the $NO_2$ total VCDs over the ECO observatory is the result of both contributions related to the stratospheric chemistry and to the tropospheric pollution due to the anthropogenic activity. The same analysis, performed for the $O_3$ total VCDs (Figure 4.7b), shows that, differently from the $NO_2$, the $O_3$ columns decrease during most days. The median and mean differences between afternoon and morning are -5x$10^{17}$ and -7.5x$10^{17}$ molecules/cm$^2$, respectively.

### 4.2.2 Total VCDs vs day of the week

Since the results shown in Figure 4.6a suggest the presence of an important tropospheric signal in the $NO_2$ total VCDs, data were analyzed while taking

into account the day of the week, in order to see if significant differences due to the different anthropogenic activity (mainly traffic) between weekends and working days exist. For this purpose, I computed the daily mean total VCDs in the time range between 8:00 and 16:00 local time. These average data were then used for the computation of a 7-day moving mean, in order to filter out the day-to-day variability. For each day, I calculated the difference between the daily mean total VCD and the 7-day running average, derived around the considered day. This operation was performed for each day for which data are present for all 7 days around it (±3). These differences were used to compute the mean anomaly for all the seven days of the week. The $NO_2$ and $O_3$ total VCDs mean anomalies are plotted against the days of the week in Figure 4.8a.

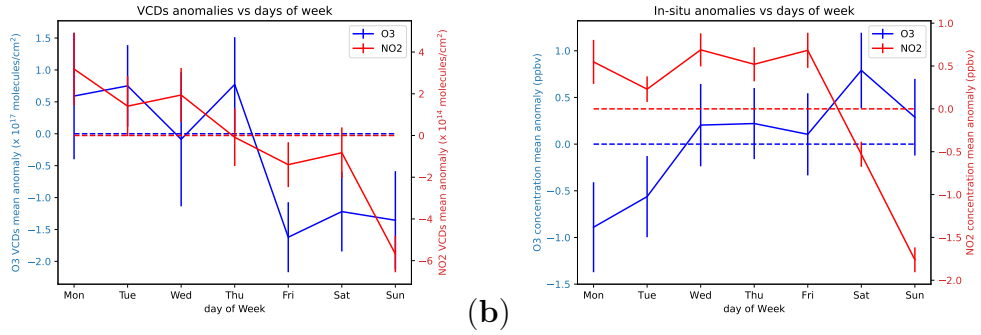


(**a**) (**b**)

Figure 4.8: Mean anomalies of $NO_2$ and $O_3$ total VCDs (a) and in-situ concentrations (b) in each day of the week. The error bars represent the standard deviations of the mean. The dashed lines represent the conditions with a null anomaly.

$O_3$ total VCDs anomalies are higher during working days, decreasing during the weekends. However, these anomalies are not highly significant because they have similar magnitudes compared to the large error bars. On the other hand, $NO_2$ total VCDs present a significant negative anomaly of about -6x$10^{14}$ molecules/cm$^2$ for Sunday, confirming the presence of anthropogenic signal. In order to better understand and to make the obtained results more significant, the same procedure was applied to the $NO_2$ and $O_3$ concentrations measured in-situ by the gas analyzer installed at ECO observatory. The $NO_2$ results in Figure 4.8b are in agreement with the weekly variability observed for the $NO_2$ total VCDs, indicating important $NO_x/NO_2$ production due to traffic, as also reported for other cities [59, 60]. On the other hand, the $O_3$ in-situ measurements reveal a slight increasing trend over the week, in contrast with the $O_3$ total VCDs weekly trend. However, the

high error bars, compared to the $O_3$ in-situ anomalies, highlight again the low significance of the results.

### 4.2.3 $NO_2$ total VCDs vs wind at 20 m

In this subsection, the results regarding the correlation between the retrieved $NO_2$ total VCDs and the wind speed and direction measured at an altitude of 20 m at the ECO observatory are shown.

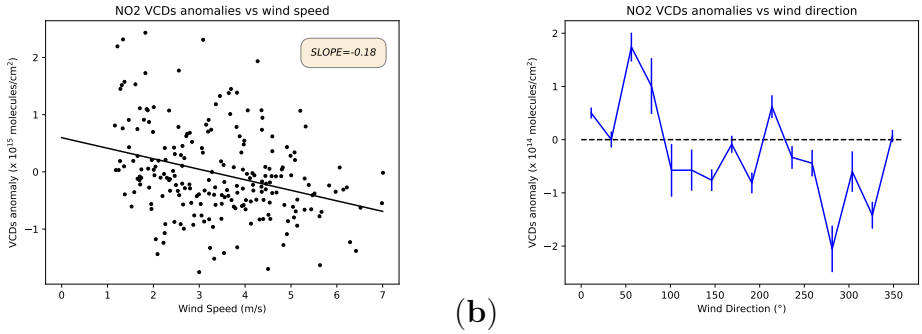


(**a**) (**b**)

Figure 4.9: $NO_2$ total VCDs anomalies with respect to the wind speed (a) and wind direction (b) measured at 20 m. In figure (b), the wind directions are indicated clockwise with 0° representing the North. Lecce is located in the northeast direction, where the peak is found.

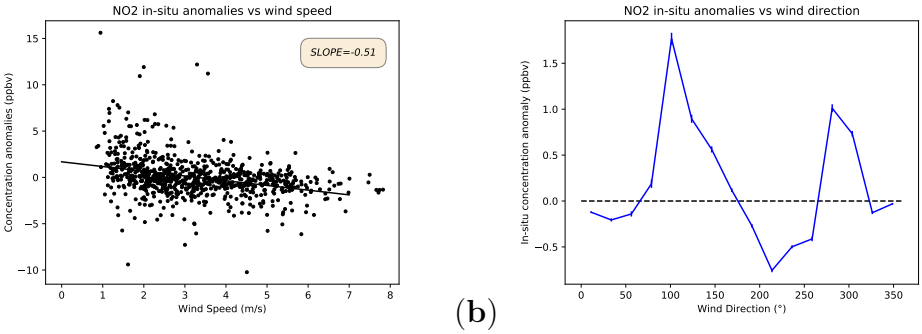


(**a**) (**b**)

Figure 4.10: $NO_2$ in situ concentrations anomalies with respect to the wind speed (a) and wind direction (b) measured at 20 m.

Figure 4.9a shows the $NO_2$ total VCDs anomalies, computed as described in Section 4.2.2, with respect to the diurnal mean wind velocities estimated in the same time range. Even though data are scattered and the correlation

is low, the negative slope of the fitting line (-0.18 molecules s $m^{-1}cm^{-2}$) confirms that the retrieved $NO_2$ total VCDs contain a tropospheric signal, consequence of the anthropogenic emissions, and states that one of the main causes of polluted days at ECO observatory is the local production. On the other hand, no plot with $O_3$ total VCDs is reported in this section because no correlation was found with the wind speed at 20 m altitude. This result confirms again the lack of $O_3$ tropospheric signal.

Figure 4.9b shows the $NO_2$ total VCDs mean anomalies with respect to the wind direction. It highlights that, together with $NO_2$ local production, a transport contribution from the city of Lecce exists as well. Indeed, the peak around 50° (about NE) corresponds to the direction where the city is located with respect to the ECO observatory. As in Section 4.2.2, the same analysis was also performed with $NO_2$ in-situ data. Figure 4.10a shows that the $NO_2$ in situ concentrations anomalies decreased with the wind speed, with a slope of -0.51 ppbv s $m^{-1}$. This result is in agreement with the one obtained for the $NO_2$ total VCDs, even though the slopes are quite different. It must be taken into account, indeed, that these two quantities are hardly comparable.

The analysis of $NO_2$ in-situ concentration anomalies in relation to the wind direction (Figure 4.10b) shows completely different results compared to the ones obtained for the $NO_2$ total VCDs in Figure 4.9b. The peak found for the total VCDs and located around 50°, in the direction of Lecce, is not present in the in-situ concentrations. However, two new peaks, around 100° and 290°, appeared. This discrepancy probably occurs because since $NO_2$ total VCDs are sensitive to the transport in the whole boundary layer, they are affected by a long-range transport and the signal coming from the city of Lecce is detectable. On the other hand, since in-situ concentrations are representative of a smaller spatial radius, the two peaks in Figure 4.10b are probably consequence of the presence of streets around the ECO observatory.

### 4.2.4 Seasonal variability

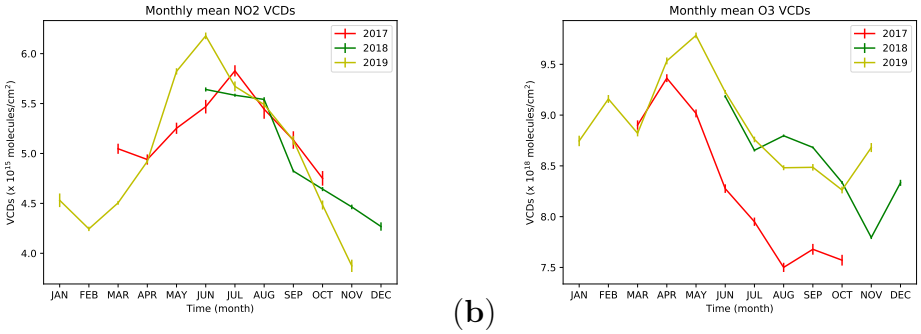


(a) (b)

Figure 4.11: Monthly variability of $NO_2$ (a) and $O_3$ total VCDs (b) in the three analyzed years. The error bars represent the standard deviations of the monthly mean values.

Figure 4.11 shows the $NO_2$ (a) and $O_3$ (b) monthly averages of the total VCDs retrieved in the years 2017, 2018 and 2019. Monthly averages were computed using only data acquired within the SZAs range between 60° and 80° to mitigate the systematic effects derived from AMFs simulations, as shown in Figure 4.5.

The $NO_2$ monthly mean total VCDs ranged between $3.5x10^{15}$ and $7x10^{15}$ molecules/cm$^2$. All the three years were characterized by similar behavior: the $NO_2$ total VCDs increased during spring, reaching the maximum value around June and July, and then started to decrease at the end of summer. Although the dataset does not contain much information for the winter periods, we can clearly notice that the decrease continued until November (2018, 2019) or December (2018). During March, the $NO_2$ total VCDs started to increase (2019). This behavior is typical of the stratospheric $NO_2$ seasonal cycle in the middle latitudes, as reported in [61], which is related to the number of sunlit hours. Further, the $O_3$ total VCDs seasonal variability is mainly driven by processes occurring in the stratosphere, where most of the $O_3$ is present. Its monthly mean VCDs ranged between $7.5x10^{18}$ and $1.0x10^{19}$ molecules/cm$^2$. The values started to increase during autumn, reaching the maximum around spring, and then rapidly decrease during summer.

The DOAS measurements reveal that the $O_3$ total VCDs in 2017 are systematically lower than in all the other years, with differences of the order of $1x10^{18}$ molecules/cm$^2$ (see Figure 4.11b). This discrepancy cannot be fully explained by the systematic errors in the reference spectra contributions because such a difference is also present between data acquired in 2017 and

2018, which were analyzed with respect to the same reference spectrum. This result was partially confirmed by OMI data. Indeed, I have verified that OMI $O_3$ total VCDs in 2017 are also lower than the ones in 2018 during the months from June to October. As an example, after computing the averages $O_3$ total VCDs for August 2017 and 2018 from OMI data, I found that the mean value in 2018 is higher than that of 2017 by about 16 D.U., which corresponds to about $4.3x10^{17}$ molecules/cm$^2$. This is more or less half of the difference that I found in the DOAS $O_3$ total VCDs (see Figure 4.11b).

## 4.3 Comparison with satellite data

### 4.3.1 Selection of coincident satellite data

The OMI $NO_2$ Standard Products (OMNO2) V4.0 [62] were downloaded from the National Aeronautics and Space Administration (NASA) Goddard Earth Sciences Data and Information Services Center (`https://search.earthdata.nasa.gov/search?q=OMNO2_003`). They contain $NO_2$ SCDs (total amount along the average optical path from the sun into the atmosphere and then toward the satellite), the $NO_2$ total VCDs, the stratospheric and tropospheric VCDs, AMFs, scattering weights for calculation of AMFs and other ancillary data. The $NO_2$ column content included in the data was derived using the DOAS technique on the UV-VIS hyperspectral earthshine radiance measurements in the range 400-470 nm, where $NO_2$ has a strong, structured absorption feature. More details can be found in [62]. In the OMI product files, the effective Cloud Fraction (CF) for each ground pixel is reported. I used these values to discriminate between clear and cloudy measurements, indicating with $qa = 1 - CF$, the quantifier which ranges from 0 (cloudy) to 1 (clear).

For the considered periods, TROPOMI offline (OFFL) products (`http://doi.org/10.5270/S5P-s4ljg54`), available in the NetCDF format, were considered. They were downloaded using the Copernicus Data Hub (`https://s5phub.copernicus.eu/dhus`), with the help of a bash script which exploits the capability of the "open data protocol" interface for accessing the Earth Observation (EO) data stored on the archive. These products contain the $NO_2$ total column content, derived using the DOAS method applied to the UV-VIS backscattered solar radiation measurements in the 405-465 nm wavelength range [63]. In the TROPOMI product files, each ground pixel has a "quality assurance value" (hereafter reported as qa) associated with it, a continuous variable, which can assume continuous values from 0 (no output) to 1 (everything is fine). According to [63], the users should use

a qa threshold of 0.75 to be sure that clouds, scenes covered by snow/ice, errors and problematic retrievals are removed. However, it is also possible to consider a qa threshold of 0.50, if the purpose is to select good quality retrievals with clouds or snow/ice in view.

The overpass times of OMI and TROPOMI are similar, being 13:45 and 13:30 local time, respectively. For each satellite overpass, all the pixels located within a radius of 20 km around the position of the station were selected. The 20 km radius was chosen in order to produce a robust analysis, considering the available satellite pixels/day in a homogeneous scene (the pixels are only over land and at the ground level). This criterion led to selecting for TROPOMI, for each day, a maximum number of 51 pixels before the 6 August 2019, as the ground pixel size was 7 km x 3.5 km, and 64 afterwards, as the along-track pixels' size was reduced from 7 to 5.5 km. Due to the higher size of the OMI ground pixel (13 km x 24 km), no more than six OMI pixels could be selected for each day. For this comparison exercise, all satellite data which had a quality flag lower than 0.5 were filtered out. More conservative quality filtering, with a threshold of 0.75, could also have been implemented. However, I have verified that the comparison results were not significantly affected.

### 4.3.2 Results

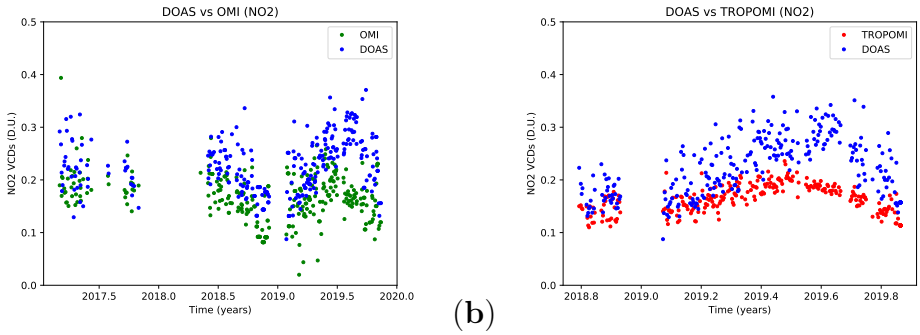


(**a**) (**b**)

Figure 4.12: $NO_2$ total VCDs measured by GASCOD/NG4 (blue dots in both panels), OMI (green line in the panel (a)) and TROPOMI (red line in the panel (b)) over the ECO observatory. DOAS measurements are time averages in a 3-h time bin around satellite overpass, and satellite data are the averages of all the coincidences within a 20 km radius.

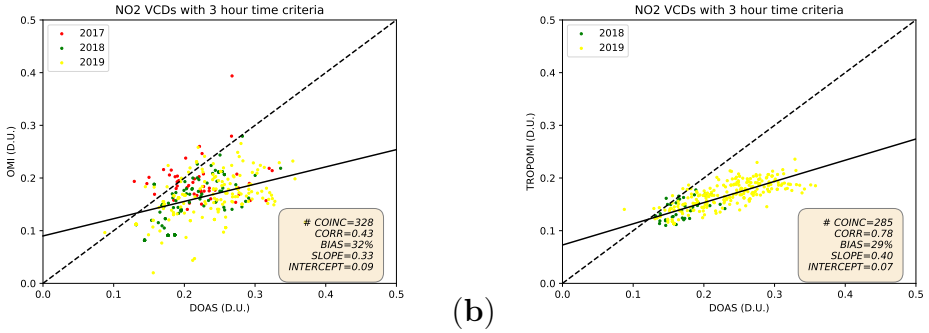


Figure 4.13: Scatterplot of $NO_2$ total VCDs measured by GASCOD/NG4 versus OMI (a) and TROPOMI (b). DOAS data were averaged in a 3-h time bin around satellite overpass and are compared with the mean satellite total VCDs in the same time bin and within a radius of 20 km from the ECO observatory.

Figure 4.12 reports the mean $NO_2$ total VCDs, computed in a 3-h time bin around the satellite overpass time, measured by GASCOD/NG4 (blue dots), and the corresponding OMI (green line in the panel (a)) and TROPOMI (red line in the panel (b)) $NO_2$ total VCDs averaged within the 20 km radius. We can observe overall good agreement, both in the absolute values and in the ability to capture the seasonality. The same averaged $NO_2$ total VCDs are used in the scatterplots of Figure 4.13.

The $NO_2$ total VCDs retrieved from GASCOD/NG4 are, on average, 32% higher than OMI and 29% higher than TROPOMI. This positive bias is also evident in the timeseries in Figure 4.12. Moreover, the two scatterplots show that important differences exist between OMI, which provides more scattered $NO_2$ columns, and TROPOMI. In particular, DOAS results are in a better agreement with TROPOMI, with a correlation coefficient of 0.78 compared to 0.43 found with OMI. The estimated linear regression slopes confirm that both satellite measurements underestimate the high values of $NO_2$ total VCDs detected by GASCOD/NG4. A similar result was found in [64], where the $NO_2$ total VCDs measured by TROPOMI and a ground-based Pandora instrument in Boulder (Colorado) are compared. They showed that very good agreement exists during low-pollution conditions and that TROPOMI underestimates the $NO_2$ total VCDs by about 30% in the presence of high $NO_2$ concentrations. The authors of [64] performed a comparison among different measurement sites, and they found that the TROPOMI underestimation is more pronounced in the most polluted cities. In [65], both OMI and TROPOMI $NO_2$ products are compared with the ones measured by a ground-based MAX-DOAS instrument in the Jing-Jin-Ji region (China).

This study revealed that both OMI and TROPOMI underestimate the $NO_2$ total columns by about 30% to 50%, in this highly polluted region. In accordance with the cited literature, our comparison showed good agreement during low polluted conditions.

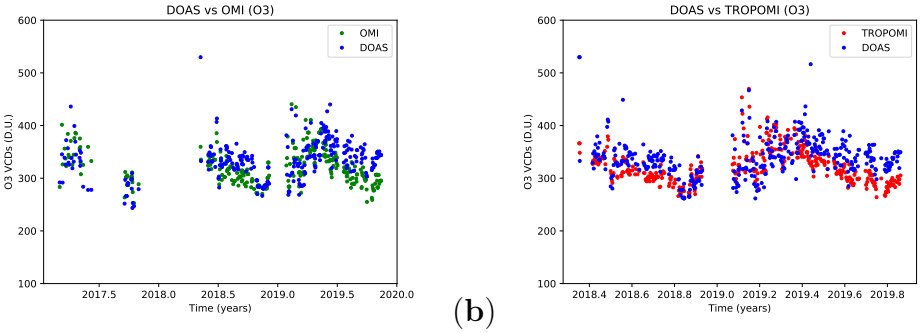


(a) (b)

Figure 4.14: $O_3$ total VCDs measured by GASCOD/NG4 (blue dots in both panels), OMI (green line in the panel (a)) and TROPOMI (red line in the panel (b)) over the ECO observatory. DOAS measurements are time averages in a 3-h time bin around satellite overpass, and satellite data are the averages of all the coincidences within a 20 km radius.

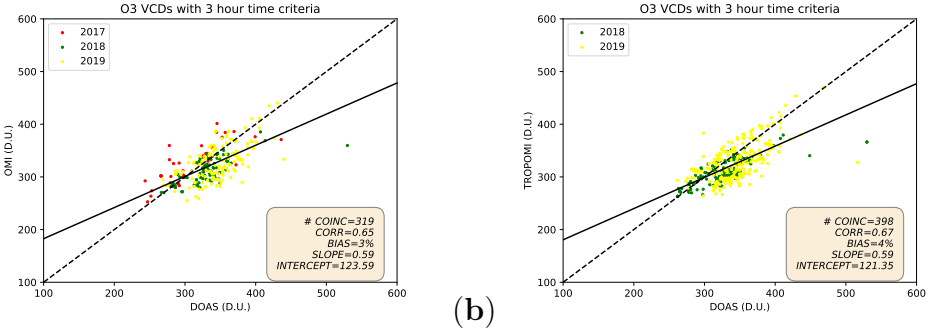


(a) (b)

Figure 4.15: Scatterplot of $O_3$ total VCDs measured by GASCOD/NG4 versus OMI (a) and TROPOMI (b). DOAS data were averaged in a 3-h time bin around satellite overpass and are compared with the mean satellite total VCDs in the same time bin and within a radius of 20 km from the ECO observatory.

The same comparison was performed for $O_3$ total VCDs, and the results are presented in Figure 4.14 and Figure 4.15. General good agreement in magnitude and seasonality occurred also in the $O_3$ total VCDs, with correlation coefficients of 0.65 and 0.67 with respect to OMI and TROPOMI,

respectively. The percentage biases found in both the $O_3$ comparisons (3 and 4%) are lower than the ones found for $NO_2$ (about 30%), showing better agreement. Other validation results revealed a lower mean bias between ground-based and satellite $O_3$ total VCDs, in the order of 1-2% [66, 67]. However, these values, obtained for latitude bands, came with high standard deviations (4-5%) that justify the higher biases in local regions.

Table 4.3: Statistical parameters of the comparisons between ground-based DOAS and satellite total VCDs for different spatial criteria for the selection of satellite data.

| | **$NO_2$** | | | | | | $O_3$ | | | | | |
|---|---|---|---|---|---|---|---|---|---|---|---|---|
| | **OMI** | | | **TROPOMI** | | | **OMI** | | | **TROPOMI** | | |
| **RADIUS (km)** | **20** | **10** | **5** | **20** | **10** | **5** | **20** | **10** | **5** | **20** | **10** | **5** |
| **COINCIDENCES** | 328 | 99 | 28 | 285 | 270 | 260 | 319 | 74 | 23 | 398 | 394 | 372 |
| **CORRELATION** | 0.43 | 0.51 | 0.45 | 0.78 | 0.78 | 0.76 | 0.65 | 0.50 | 0.49 | 0.67 | 0.68 | 0.66 |
| **BIAS (%)** | 32 | 28 | 24 | 29 | 28 | 27 | 3 | 4 | 2 | 4 | 4 | 4 |
| **SLOPE** | 0.33 | 0.39 | 0.47 | 0.40 | 0.39 | 0.39 | 0.59 | 0.43 | 0.55 | 0.59 | 0.62 | 0.62 |
| **INTERCEPT (D.U.)** | 0.09 | 0.08 | 0.07 | 0.07 | 0.08 | 0.08 | 124 | 179 | 143 | 121 | 111 | 111 |

I also verified the robustness of the comparison between ground-based DOAS total VCDs and satellite measurements because they do not significantly depend on the spatial radius chosen to compute the averages around the ECO observatory, as summarized in Table 4.3. Indeed, similar and very stable results were found for the comparisons with TROPOMI. On the other hand, the comparisons with OMI revealed less stable statistical parameters, partially justified by the important decrease in coincidences with the chosen radius.

Table 4.4: Statistical parameters of the comparisons between ground-based DOAS and satellite total VCDs with a spatial radius of 20 km and for different seasons.

| | $NO_2$ | | | | | | | | $O_3$ | | | | | | | |
|---|---|---|---|---|---|---|---|---|---|---|---|---|---|---|---|---|
| | **OMI** | | | | **TROPOMI** | | | | **OMI** | | | | **TROPOMI** | | | |
| **SEASONS** | **WIN** | **SPR** | **SUM** | **AUT** | **WIN** | **SPR** | **SUM** | **AUT** | **WIN** | **SPR** | **SUM** | **AUT** | **WIN** | **SPR** | **SUM** | **AUT** |
| **COINCIDENCES** | 27 | 96 | 90 | 115 | 31 | 80 | 69 | 105 | 26 | 88 | 91 | 114 | 35 | 91 | 146 | 126 |
| **CORRELATION** | 0.67 | 0.25 | 0.08 | 0.49 | 0.62 | 0.70 | -0.03 | 0.74 | 0.93 | 0.62 | 0.54 | 0.44 | 0.94 | 0.65 | 0.59 | 0.60 |
| **BIAS (%)** | 17 | 25 | 34 | 38 | 14 | 25 | 37 | 30 | -3 | -1 | 7 | 5 | -4 | 0 | 7 | 8 |
| **SLOPE** | 0.53 | 0.17 | 0.06 | 0.46 | 0.31 | 0.31 | -0.01 | 0.37 | 0.91 | 0.45 | 0.40 | 0.21 | 0.91 | 0.39 | 0.38 | 0.34 |
| **INTERCEPT (D.U.)** | 0.06 | 0.14 | 0.17 | 0.05 | 0.09 | 0.10 | 0.19 | 0.07 | 41 | 197 | 181 | 227 | 44 | 214 | 189 | 183 |

It must be mentioned that the systematic errors described in Section 4.1.4 could be responsible for some of the positive biases found in the comparison results. Indeed, taking into account Figure 4.5 and considering that OMI and TROPOMI overpass Lecce at around noon, the systematic effect due to the AMFs would lead to an overestimation of the retrieved total VCDs, mainly when the SZAs around noon are low (summer) and when high $NO_2$

and $O_3$ tropospheric concentrations are present. This theory is confirmed in Table 4.4, where all the statistical parameters for the four different seasons are reported. Indeed, it is evident that the $NO_2$ and $O_3$ biases have seasonal behavior, increasing during summer and decreasing in winter. However, due to the low number of coincidences, mainly during winter, these statistical parameters are less stable and robust than the ones reported in Table 4.3.

The results of this chapter have highlighted that the $NO_2$ tropospheric contribution significantly affects the $NO_2$ total VCDs, while the $O_3$ total VCDs contain no tropospheric signals. This explains why the $O_3$ comparison with respect to satellite data showed better agreement compared to the $NO_2$ one. Indeed, satellite measurements are less sensitive to the lower part of the atmosphere.

# Chapter 5

# Towards a FRM4DOAS site in the Po Valley

This chapter is based on the following paper: Pettinari P., Castelli E., Papandrea E., Busetto M., Valeri M. and Dinelli B.M.: Towards a New MAX-DOAS Measurement Site in the Po Valley: $NO_2$ Total VCDs, Remote Sensing, 2022, 14(16), 3881.

*This study was performed thanks to all the coauthors, as part of the project IDEAS-QA4EO WPs-2250-2251: "DOAS-BO: Towards a new FRM4DOAS-compliant site" SERCO-IDEAS-QA4EO-BO/SUB27-IDEAS-QA4EO-Quality Assurance For Earth Observation-QA4EO/SER/SUB/27, Instrument Data quality Evaluation and Assessment Service-Quality Assurance for Earth Observation (IDEAS-QA4EO) contract funded by ESA-ESRIN (n. 4000128960/19/I-NS).*

*Elisa Castelli and Massimo Valeri were the project administrators. Together with Enzo Papandrea, they conceptualized this study and organized the measurement campaigns that will be illustrated in this chapter. With the help of Elisa Castelli and Enzo Papandrea, I mainly worked on the instrumental set-up, the formal data analysis and on the manuscript writing. Maurizio Busetto gave an important practical contribution, indeed he installed the SkySpec-2D in its final location, at the "Giorgio Fea" observatory in San Pietro Capofiume. Bianca Maria Dinelli's comments were important to reach the final form of the paper and moreover, she supervised the whole PhD work.*

## 5.1 Project overview

The purpose of the project is to create the first Italian FRM4DOAS-compliant MAX-DOAS measurement site in the Po Valley, which is the most industrialized and polluted area of Italy; here, high mountains surround the Po basin, preventing pollution from dispersion, especially in wintertime. DOAS measurements, not compliant with the standards, were performed in the framework of a few campaigns [68, 34, 69] and from two DOAS/MAX-DOAS instruments, developed at CNR-ISAC and located in the Emilia Romagna Region: one at Monte Cimone and the other in Bologna. The instrument located in Bologna is the TROPOGAS (described in section 3.2), that is measuring diffuse solar spectra on the roof of the CNR-ISAC building since 2018.

The need for DOAS measurements satisfying Quality Assurance (QA) criteria motivated, in the frame of the Instrument Data Evaluation and Analysis Service (IDEAS) Quality Assurance for Earth Observation (QA4EO) service DOAS-BO ESA project, the assessment of the performances of the TROPOGAS spectrometer (see section 3.2.2) with respect to FRM4DOAS requirements and the update of its measurement configuration and data analysis to follow the FRM4DOAS standards as much as possible. In May 2021, the CNR-ISAC institute acquired a new MAX-DOAS system in the context of the Italian funded project "Sviluppo delle Infrastrutture e Programma Biennale degli Interventi del Consiglio Nazionale delle Ricerche - Potenziamento Infrastrutturale: progetti di ricerca strategici per l' ente. Progetto 32-ASSE NORD Pianura Padana Mt. Cimone, Bologna, San Pietro Capofiume". The chosen system is the SkySpec-2D instrument (described in section 3.1), which is fully compliant with FRM4DOAS requirements. For this reason, in the end, SkySpec-2D was chosen to achieve the project's goal. The selected location for this system is the "Giorgio Fea" meteorological observatory at SPC, Bologna, in the middle of the Po Valley and far from cities and local polluted hot spots. That position is representative of the background pollution in the Po Valley and makes these measurements suitable for satellite validation.

The two projects mentioned above create opportunities to:

- re-enforce the Italian know-how on DOAS/MAX-DOAS techniques, following the legacy of the CNR-ISAC institute;
- re-enforce the observational potential of the Po Valley infrastructure through the acquisition of a ground-based remote-sensing instrument compliant with the ESA reference standards that can be used for both satellite validation and scientific studies of air quality in one of the most polluted European regions.

In this chapter, the work carried out to set up the new MAX-DOAS measurement site at SPC in the Po Valley is described. To assess its performances, the SkySpec-2D system was employed in an inter-comparison campaign with the research-grade custom-built TROPOGAS spectrometer in Bologna in August 2021. Then, at the beginning of September 2021, the instrument took part in a second inter-comparison campaign at the Boundary-layer Air Quality-analysis Using Network of Instruments (BAQUNIN) [70] super-site at La Sapienza University in Rome, where the Pandora#117 instrument, fiducial reference instrument for satellite validation, is located. Finally, at the end of September 2021, the SkySpec-2D was installed at its final location at the "Giorgio Fea" observatory.

Here, the results of the inter-comparison campaigns and the first results of $NO_2$ total VCDs obtained in a nine-month period by the SkySpec-2D at SPC are shown. Comparisons with collocated TROPOMI and OMI satellite data are also reported. For the comparisons, the $NO_2$ total VCDs, retrieved from zenith-sky MAX-DOAS measurements (SkySpec-2D and TROPOGAS), from sun direct Pandora#117 measurements, and from satellite measurements are considered.

## 5.2 Analysis method

### 5.2.1 Retrieval of the $NO_2$ total VCDs from zenith DOAS measurements

Here, the general analysis steps performed to estimate the $NO_2$ total VCDs from the measurements acquired by the two MAX-DOAS instruments during both the measurement campaigns are described.

#### SCDs fit

The zenith-sky spectra measured by the two CNR-ISAC MAX-DOAS systems (TROPOGAS and SkySpec-2D) were analyzed with the DOAS technique to retrieve $NO_2$ total VCDs. In the first step, $NO_2$ SCDs were estimated by the QDOAS software from the measured zenith-sky spectra. In this step, all the measurements acquired by each of the two MAX-DOAS instruments were analyzed with respect to a fixed reference spectrum, chosen at low SZA (around noon), in order to avoid high atmospheric absorption. Details on the QDOAS processing will be shown in sections 5.2.2 and 5.2.3.

### Reference contribution estimate

The reference contribution was estimated with the same method reported in Section 4.1.3. Also in this case, its estimated uncertainty is 2 x $10^{15}$ molecules/cm$^2$.

These results, for both TROPOGAS and SkySpec-2D in the two measurement campaigns, will be shown in Sections 5.2.2 and 5.2.3.

### Filtering of data affected by aerosol and clouds

As reported in Section 4.1.2 for data acquired in Lecce, the filtering method exploits the retrieved $O_4$ SCDs. However, here I decided to adopt a different strategy. In particular, this filtering is based on an iterative process that exploits the information coming from the $O_4$ SCDs and $NO_2$ total VCDs retrieved in the current iteration. This type of filtering is applied to zenith measurements only. The first step consists of dividing all the $O_4$ SCDs into 3°-wide SZA bins and computing the $O_4$ SCD median value for each bin. Since most of the days during the campaigns were sunny, we assume that all these median values correspond to clear-sky conditions. At this point, to classify clear and cloudy data, we need to define, for each SZA bin, a maximum distance from the $O_4$ SCD median value. In this way, data with $O_4$ SCDs which fall outside the chosen range are filtered out. This threshold is estimated through an iterative process. In the first step, the criterion is very stringent, leading to a low number of clear-sky data. During every iteration, the $O_4$ range, in each SZA bin is increased, leading to more clear-sky data. The process, in each SZA bin, stops when an important difference arises between the retrieved $NO_2$ total VCDs labeled as clear and cloudy. In this way, we are confident to be filtering out the $NO_2$ total VCDs labeled as cloudy that are systematically biased compared to the clear-sky ones. Final filtering results for both TROPOGAS and SkySpec-2D instruments, in the two measurement campaigns, will be reported in Sections 5.2.2 and 5.2.3.

### AMFs simulation

The AMFs used to convert the SCDs into total VCDs were simulated with SCIATRAN, adopting the same method used for the analysis at the ECO observatory in Lecce, as described in section 2.4.

### 5.2.2 Bologna inter-comparison campaign

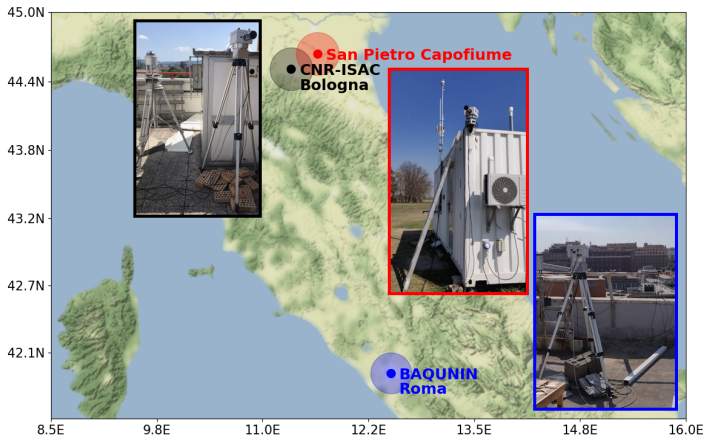


Figure 5.1: Location of the CNR-ISAC in Bologna (black), of the SPC "Giorgio Fea" observatory (red) and of the BAQUNIN super-site in Rome (blue). Photos of the instruments in the three locations are also shown.

The inter-comparison campaign between SkySpec-2D and TROPOGAS was performed on the roof of the CNR-ISAC headquarter (Lat: 44.52°N, Lon: 11.34°E, Altitude: 39 m a.s.l., 25 m a.g.l., Figure 5.1) within the CNR campus (Via Gobetti 101, Bologna, Italy) located in the city suburbs. The measurement site is classified as urban background. The A14 motorway, the Bologna (BLQ) international airport, and the city center are located 0.8 km to the north, 2.6 km to the west and 1.7 km to the south, respectively. The SkySpec-2D vs TROPOGAS campaign was held from 4 August to 2 September 2021. The period was characterized by generally stable and sunny weather. Both the instruments used a measurement configuration compliant to the FRM4DOAS guidelines.

The TROPOGAS analysis was performed using a fixed reference spectrum (measured on 11 August 2021 at 29.10° SZA). We decided to analyse the TROPOGAS spectra using the absorption cross-section at 298 K. This choice is in agreement with the results in [71], where the authors state that, in polluted European regions, the effective temperatures representing $NO_2$ total column are estimated to be about 270-280 K. QDOAS set-up is reported in Table 5.1.

The SkySpec-2D analysis set-up is reported in Table 5.2. This set-up is almost the same used for TROPOGAS apart from the larger spectral interval used.

Table 5.1: QDOAS settings for TROPOGAS $NO_2$ SCDs calculations in visible spectral range; "orto." means that the cross-sections are orthogonalized with respect to another cross-section at a different temperature.

| | **$NO_2$ VIS** | **Ref. Cross-Section** |
|---|---|---|
| Calibration spectral range | 455-495 nm (6 points) | |
| Retrieval spectral range | 460-490 nm | |
| Considered XS | $NO_2$ 298 K | from Van Daele [46] |
| | $NO_2$ 220 K | from Van Daele [46] |
| | (orto. to $NO_2$ 298 K) | |
| | $O_3$ 223 K | from Bogumil [47] |
| | $O_4$ | from Herman [48] |
| | Ring | computed according to [49] |
| | $O_3$ 293 K | from Bogumil [47] |
| | (orto. to $O_3$ 223 K) | |
| | Glyoxal | from Volkamer [50] |
| | $H_2O$ | from Herman [48] |
| Other fits | Polynomial deg. 5 | |
| | linear offset order 1 | |

Table 5.2: QDOAS settings for SkySpec-2D $NO_2$ SCDs calculations in visible spectral range; "orto." means that the cross-sections are orthogonalized with respect to another cross-section at a different temperature. The $NO_2$ cross-sections used for the measurement campaigns in Bologna and Rome are labeled with (a) and (b), respectively.

| | **$NO_2$ VIS** | **Ref. Cross-Section** |
|---|---|---|
| Calibration spectral range | 420-500 nm (6 points) | |
| Retrieval spectral range | 430-490 nm | |
| Considered XS | (a) $NO_2$ 298 K | from Van Daele [46] |
| | (a) $NO_2$ 220 K | from Van Daele [46] |
| | (a) (orto. to $NO_2$ 298 K) | |
| | (b) $NO_2$ 254.5 K | from Van Daele [46] |
| | $O_3$ 223 K | from Bogumil [47] |
| | $O_4$ | from Herman [48] |
| | Ring | computed according to [49] |
| | $O_3$ 293 K | from Bogumil [47] |
| | (orto. to $O_3$ 223 K) | |
| | Glyoxal | from Volkamer [50] |
| | $H_2O$ | from Herman [48] |
| Other fits | Polynomial deg. 5 | |
| | linear offset order 1 | |

In this case, we also chose to fit the $NO_2$ SCDs using the cross-section at

298 K in order to be consistent with the TROPOGAS analysis. Moreover, for consistency reasons, the fixed reference spectrum used in the SkySpec-2D analysis was chosen as much as possible in close time coincidence with the one used for the TROPOGAS analysis (measured on 11 August 2021 at 29.38° SZA). The Langley plot analysis applied to TROPOGAS and SkySpec-2D SCDs provides the reference contributions of $4.5\text{x}10^{15}$ molecules/cm$^2$ (see Figure 5.2a) and $9.7\text{x}10^{15}$ molecules/cm$^2$ (see Figure 5.3a), respectively. Although the two chosen reference spectra are close in time, the two reference contributions are different due to the high temporal variability in $NO_2$ total VCDs occurring in the central hours of that day.

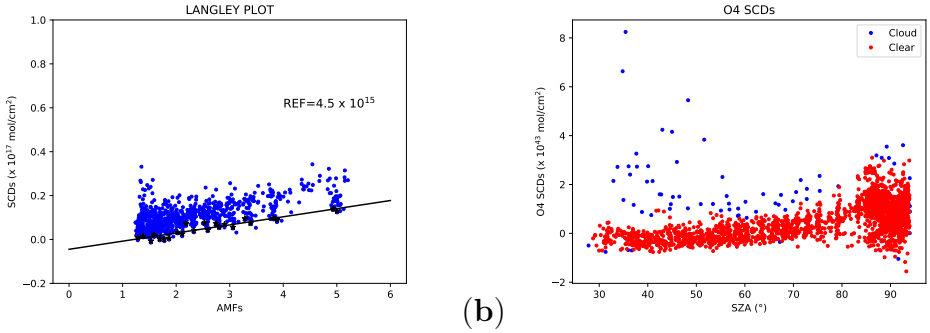


(**a**) (**b**)

Figure 5.2: (a) Langley plot and (b) $O_4$ SCDs data filtering for TROPOGAS during the Bologna inter-comparison campaign. Results for $NO_2$ cross-sections at 298 K.

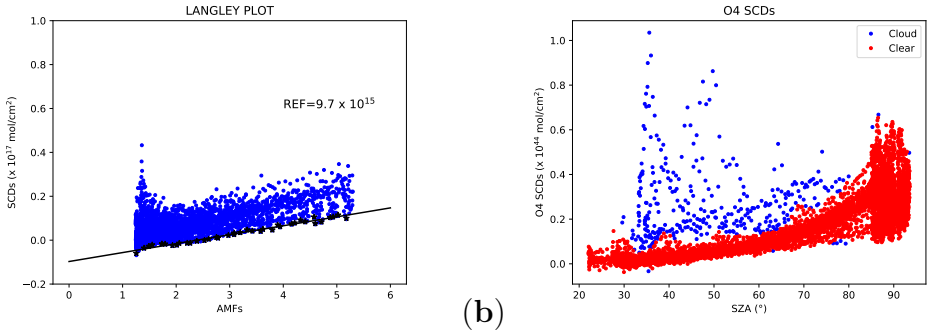


(**a**) (**b**)

Figure 5.3: (a) Langley plot and (b) $O_4$ SCDs data filtering for SkySpec-2D during the Bologna inter-comparison campaign. Results for $NO_2$ cross-sections at 298 K.

At the end of the filtering process, 94% of data, acquired by TROPOGAS, were marked as not heavily contaminated by clouds, as can be seen in Fig-

ure 5.2b, while the SkySpec-2D clear-sky make up 96% of the observations (Figure 5.3b). For comparison with satellite data, the TROPOGAS and SkySpec-2D total VCDs were averaged in a time interval of ±60 min centered on the satellite overpass time. This high averaging time-range was applied to improve statistical significance, since TROPOGAS exposure times are higher than those for SkySpec-2D, leading to fewer measured spectra in a given amount of time.

### 5.2.3 BAQUNIN inter-comparison campaign

The SkySpec-2D vs Pandora inter-comparison campaign was performed at the physics department of La Sapienza University (Lat: 41.90° N, Lon: 12.52° E, Altitude: 75 m a.s.l., Figure 5.1), part of the BAQUNIN super-site [70]. Since the super-site has among its primary objectives the validation of satellite products, best practices and QA procedures were applied. The campaign was held in the time period from 6 to 21 September 2021. The weather was sunny for the majority of the days, allowing the collection of good quality spectra.

In contrast with the analysis method described for the campaign in Bologna, we decided to analyze the data, acquired during the measurement campaign in Rome, using the cross-section at 254.5 K, in order to be as consistent as possible with the Pandora analysis. Indeed, for the Pandora processing, the $NO_2$ cross-section used was corrected for the effective temperature which, during the measurement campaign, was estimated to be on average around 270 K. Regardless, for completeness, the impact of the different cross-section temperatures on the final SkySpec-2D total VCDs will be shown.

For the BAQUNIN campaign, the fixed reference spectrum used in the analysis was chosen on a clear-sky day according to the pictures recorded by the SkySpec-2D cameras (spectrum measured on 12 September 2021 at 37.89° SZA). The Langley plot, reported in Figure 5.4a, shows an estimated reference contribution of $1.0 \times 10^{16}$ molecules/cm$^2$.

The zenith SCDs were further processed to remove the heavily cloud-contaminated measurements. The filtering based on using $O_4$ SCDs excludes 5% of the observations (Figure 5.4b). For comparison with satellite data, the SkySpec-2D total VCDs are averaged in a ±15 min time interval centered on the satellite overpass time.

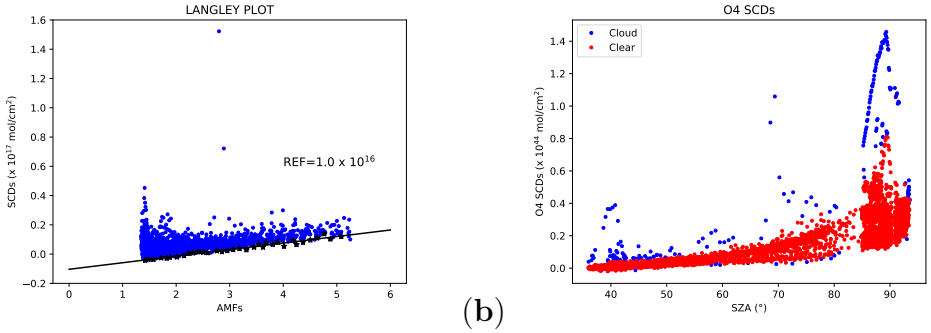


(a) (b)

Figure 5.4: (a) Langley plot and (b) $O_4$ SCDs data filtering for SkySpec-2D during the BAQUNIN inter-comparison campaign. Results for $NO_2$ cross-sections at 254.5 K.

## 5.3 Correlative data

### 5.3.1 Pandora data

During the BAQUNIN campaign, the SkySpec-2D and the Pandora#117 operated in close coincidence. The Pandonia Global Network (PGN) centrally processes the spectra acquired by the Pandora instruments. The Pandora#117 data were directly downloaded from the PGN website (`https://www.pandonia-global-network.org/`). We used the most updated version of the data for $NO_2$ ($rnvs3p1-8$). We considered only Pandora retrievals with a data quality flag value of 0 or 10, corresponding to the so-called assured high-quality data [72]. We will restate here that for the Pandora data analysis, the effective temperature of the $NO_2$ profile is estimated during the fit. The average value of the retrieved effective temperature during the campaign corresponds to about 270 K. For comparison with satellite data, the Pandora#117 total VCDs were averaged in a time interval of $\pm 15$ min centered on the satellite overpass time.

### 5.3.2 TROPOMI and OMI satellite data

For S-5P TROPOMI, we used the offline $NO_2$ products [73, 74]. For OMI, we used the Multi-Decadal Nitrogen Dioxide and Derived Products from Satellites (MINDS) [75], which have been developed with the aim to be consistent data records currently spanning about 15 years. At the moment, the MINDS archive covers the period from 1 October 2004 to 1 October 2021. For this reason, no comparison with OMI data after September 2021 was performed.

During this work, for both satellites, we used the $NO_2$ summed total column, which is the sum of the tropospheric and stratospheric VCDs. This product is described by the data provider as the best physical estimate of the $NO_2$ total vertical column and recommended for comparison to ground-based total column observations [63]. For TROPOMI, we used only products with a combined QA value higher than 0.75 in order to remove cloudy spectra, parts of the scenes covered by snow/ice, errors and problematic retrievals [74]. Since a quality flag is not available for OMI, we used only data having the inverse of the cloud fraction greater than 0.75, as suggested in [76].

For the comparison with ground-based products, the satellite data were averaged over a circle centred on the ground site. For this, we used a 5 km radius for TROPOMI and 20 km radius for OMI, due to its lower spatial resolution.

## 5.4 Results

### 5.4.1 Bologna inter-comparison campaign

The comparison between products from two MAX-DOAS instruments with different characteristics and processed with the same analysis method is useful for the assessment of the instruments' performances. Indeed, the only contribution to the bias coming from the processing method is due to the uncertainties in the estimated references that is about 2 x $10^{15}$ molecules/$cm^2$, as written in Section 5.2.1. This motivated the TROPOGAS versus SkySpec-2D comparison. Figure 5.5 shows $NO_2$ filtered total VCDs retrieved from 4 to 30 August 2021 by SkySpec-2D and TROPOGAS and averaged over 5 min intervals. We observe a generally good agreement between the two ground-based instruments considering both the absolute total VCDs values and their behavior during the day: the average difference is about 9%, with SkySpec-2D-retrieved total VCDs higher than the TROPOGAS ones. Zooming on the days 5 and 6 August (Figure 5.6), we can appreciate how good the agreement is between the two instruments in reproducing the $NO_2$ variations during the day.

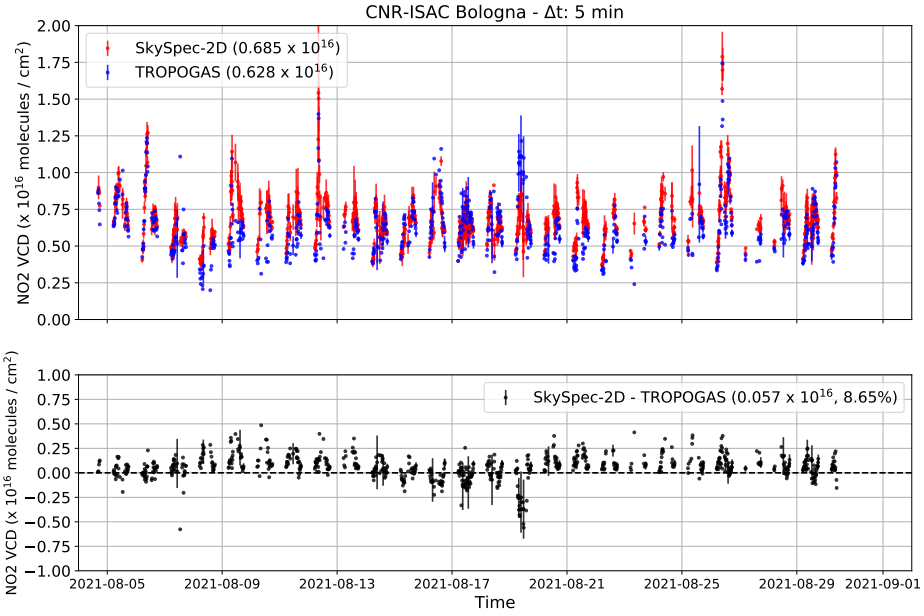


Figure 5.5: $NO_2$ total VCDs from TROPOGAS (in blue) and SkySpec-2D (in red), averaged in 5 min intervals, during the Bologna inter-comparison campaign, with average values reported (upper panel). The panel below shows the differences, with the mean absolute and percentage values reported.

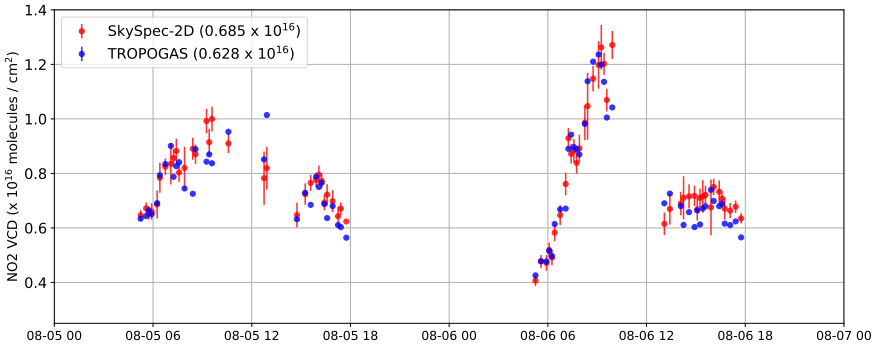


Figure 5.6: Zoom of Figure 5.5 onto days 5 and 6 August 2021.

Considering again data averaged over 5 min intervals, the agreement between the two instruments, over the whole campaign period, is characterized by a correlation coefficient of 0.77, as can be seen from the scatterplot in Figure 5.7.

Since most of the measurements acquired during the campaign in Bologna are related to AMFs lower than 4 (see Figure 5.2a and Figure 5.3a), the

reference contribution errors will affect most of the final $NO_2$ total VCDs, for each instrument, with at least 0.5 x $10^{15}$ molecules/cm$^2$. From these considerations, the bias found between SkySpec-2D and TROPOGAS (0.57 x $10^{15}$ molecules/cm$^2$) is fully consistent with the reference contribution errors. On the other hand, the errors in the AMFs (identical for both instruments) and in the SCDs (random errors), from the fit, do not contribute to the systematic bias. Part of the discrepancies found between SkySpec-2D and TROPOGAS $NO_2$ total VCDs are also due to the instrumental differences, such as different FOVs and integration times.

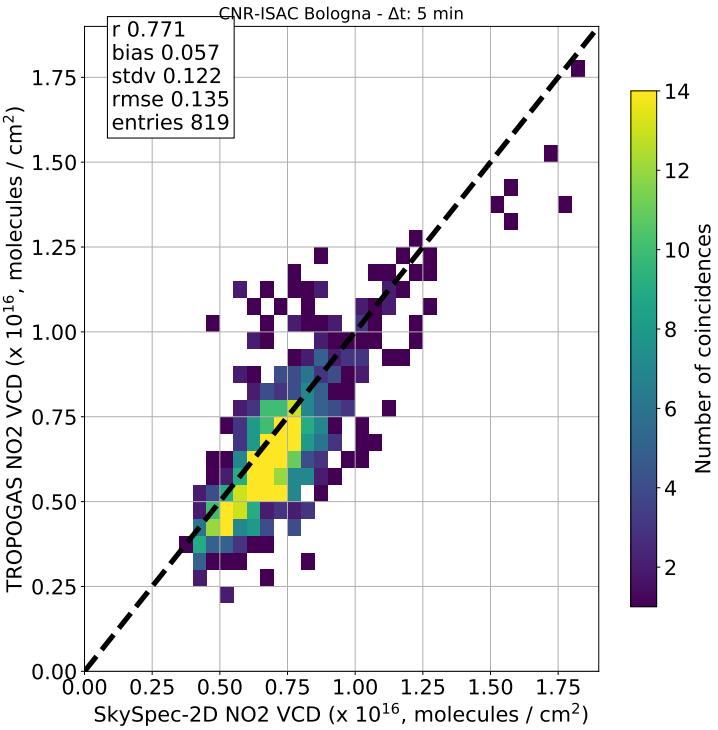


Figure 5.7: Scatterplot of $NO_2$ total VCDs retrieved from TROPOGAS and SkySpec-2D during the Bologna inter-comparison campaign and averaged in 5 min intervals.

The comparison with satellite data shows good results: in Figure 5.8, the comparison between S-5P TROPOMI $NO_2$ total VCDs and ground-based instrument retrievals averaged in a time interval of 60 min around the TROPOMI overpass time is reported. The average difference between satellite and ground-based results is about -15% with respect to SkySpec-2D and -3% with respect to TROPOGAS.

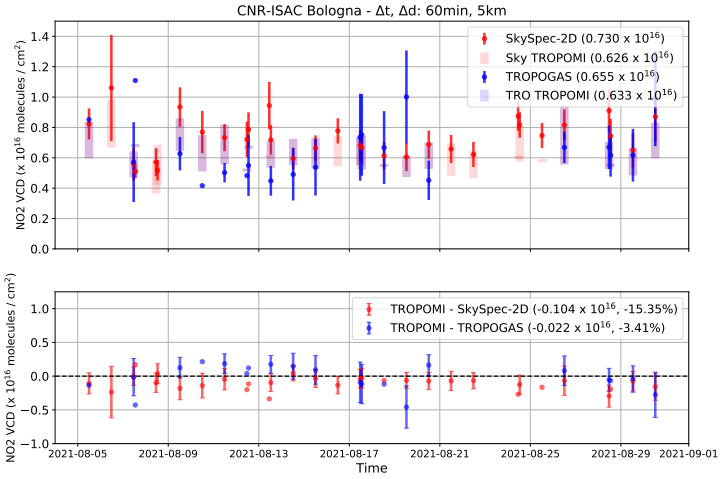


Figure 5.8: $NO_2$ total VCDs, averaged in 60 min intervals around the satellite overpass, from TROPOGAS (in red) and SkySpec-2D (in blue) versus TROPOMI (red and blue shadows, respectively) during the Bologna inter-comparison campaign. The TROPOMI shadows represent the mean values within the 5 km radius with standard deviations.

Also the biases between TROPOMI and SkySpec-2D (-1 x $10^{15}$ molecules/cm$^2$) and between TROPOMI and TROPOGAS (-0.2 x $10^{15}$ molecules/cm$^2$) are entirely consistent with the reference contribution errors. Indeed, the TROPOMI overpass always occurs around noon, when the AMFs are lower than 2, leading to an error, propagated to the final $NO_2$ total VCDs, of at least 1 x $10^{15}$ molecules/cm$^2$. The spatial and temporal mismatches between satellite and ground-based acquisitions are responsible for the observed spread.

The comparison with OMI data was performed using the same time criterion (60 min) and a relaxed spatial coincidence criterion (20 km), to include a significant number of satellite data. The bias is of the order of -22% with respect to SkySpec-2D and -12% with respect to TROPOGAS.

### 5.4.2 BAQUNIN inter-comparison campaign

Although the SkySpec-2D series of instruments are included in the FRM4DOAS network, to quantify the performances of our instrument we compared its measurements to the reference fiducial instrument Pandora#117. To evaluate the quality of the products of the SkySpec-2D instrument in the frame of satellite validation, we also compared the SkySpec-2D and Pandora#117 $NO_2$ total VCDs to similar products retrieved from the S-5P TROPOMI and the Earth Observing Satellite (EOS)-Aura OMI observations.

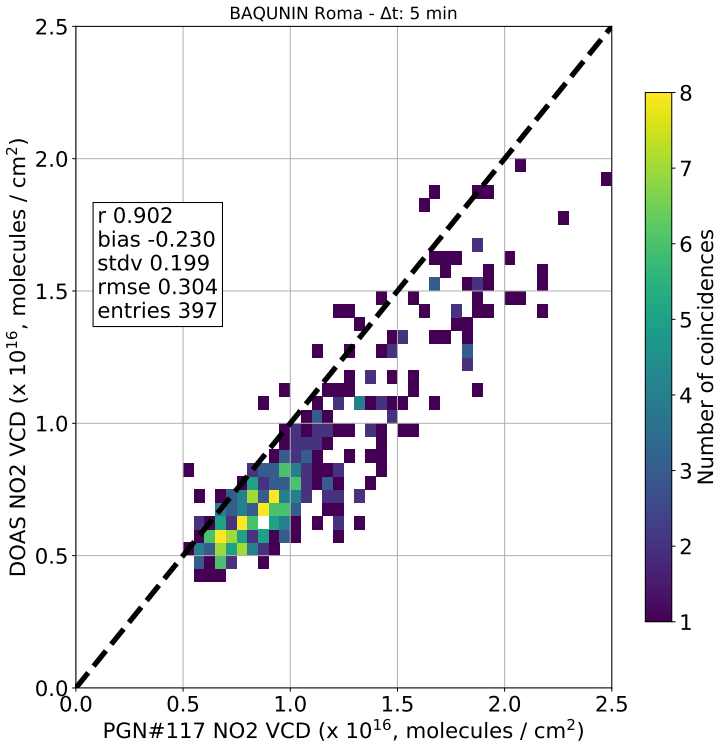


Figure 5.9: Scatterplot of $NO_2$ total VCDs retrieved from SkySpec-2D ($NO_2$ cross sections at 254.5 K) and Pandora#117 during the BAQUNIN intercomparison campaign. Data are averaged in 5 min intervals.

The differences between the two ground-based datasets were evaluated considering the entire period of the measurement campaign. The two datasets were averaged on 5 min intervals. The plots in Figure 5.9 and Figure 5.10 show the scatterplot and daily distributions of $NO_2$ total VCDs, respectively, retrieved by the two instruments. We observe an extremely high correlation between the two datasets (0.902). SkySpec-2D correctly reproduces all the features of the $NO_2$ distributions observed by Pandora #117. The bias between the two ground-based datasets is about -0.230 x $10^{16}$ molecules/cm$^2$ (-24%). We analyzed the differences between SkySpec-2D and Pandora $NO_2$ total VCDs also as a function of the hour of the day, the solar zenith angle and solar azimuth angle. Since we used only the SkySpec-2D zenith-sky observations, the only instrument that changes its observation geometry (directly pointing to the Sun) is the Pandora#117. We did not observe any evident dependency on these three quantities.

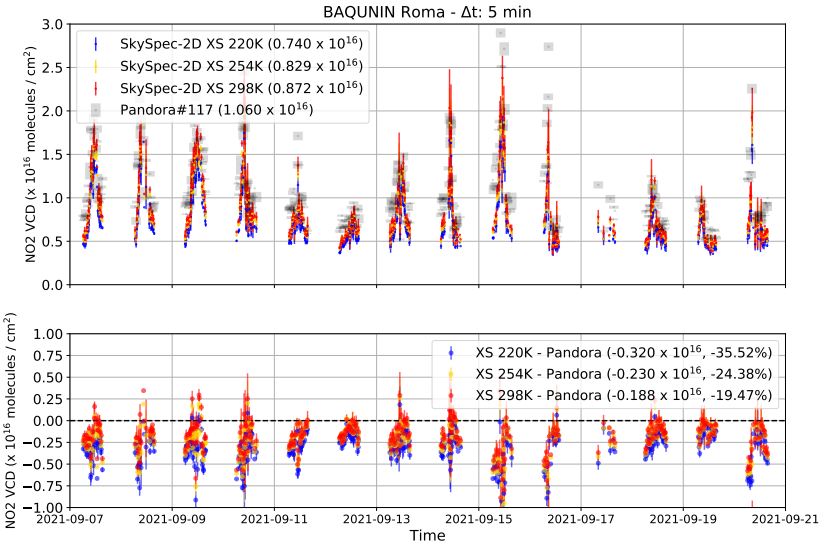


Figure 5.10: $NO_2$ total VCDs retrieved from SkySpec-2D with $NO_2$ cross-sections at different temperatures (220 K in blue, 254.5 K in yellow, 298 K in red) and Pandora#117 (grey shadow) during the BAQUNIN inter-comparison campaign, results and absolute differences. Data are averaged in 5 min intervals.

As already stated, for this campaign, we used $NO_2$ cross-sections for an equivalent temperature of 254.5 K. However, in order to evaluate the impact and the uncertainty introduced by not-representative cross-sections, we computed the SkySpec-2D total VCDs considering also the cross-sections at 220 K and 298 K, and we compared the different products with respect to the Pandora#117 total VCDs, see Figure 5.10. Generally, we observed that different cross-sections work as an offset, and that they do not introduce any evident dependency from the SZA. We also observed that the uncertainty introduced using a not-representative cross section is up to 10%, as reported in [77]. We observed the best agreement using the $NO_2$ cross-section at 298 K (-19% difference).

Different considerations on the biases must be made for the comparison with the Pandora#117 instrument, since the processing is performed by the PGN central facility and the instrument has a different measurement configuration (direct radiance measurements). For this reason, the bias is not only related to the uncertainties in the reference contributions, but also to the errors in the AMFs. Considering that we have a bias of -24% with cross-section at 254.5 K and of -19% at 298 K, we can evince that using a cross-section at 270 K, which is not present in literature and which represents the effective temperature for the Pandora#117 data (see Section 5.3.1), the bias would

be of the order of -20%.

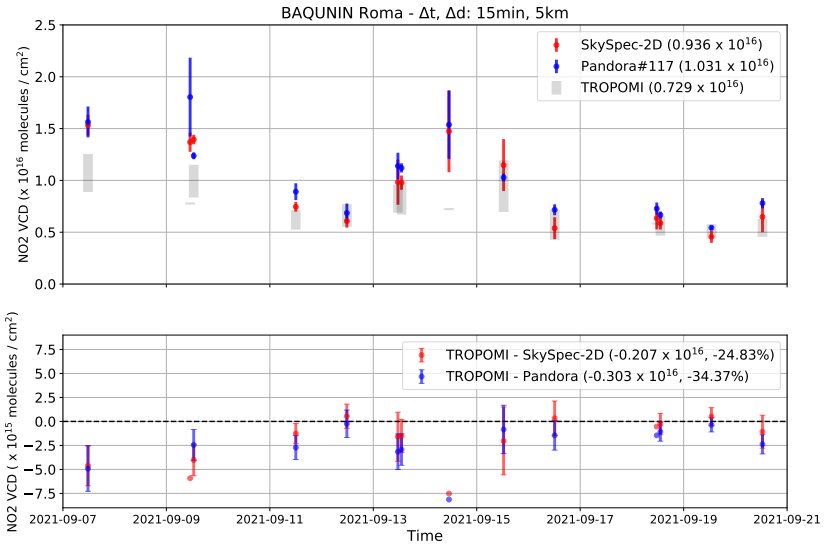


Figure 5.11: $NO_2$ total VCDs, averaged in 15 min intervals, retrieved from SkySpec-2D (in red) and Pandora#117 (in blue), and $NO_2$ VCDs measured by TROPOMI (grey shadow) during the BAQUNIN inter-comparison campaign. The TROPOMI shadows represent the mean values within the 5 km radius with standard deviations.

As last step, we evaluated the agreement between the ground-based instruments and the satellite datasets, exploiting the S-5P and EOS-Aura overpasses during the measurement campaign. In Figure 5.11, we report the observations averaged around the TROPOMI overpasses and the differences between ground-based and the TROPOMI observations. Generally, we observed that both Pandora#117 and SkySpec-2D $NO_2$ total VCDs overestimated the satellite $NO_2$ total VCDs. We observed a bias of -25% for SkySpec-2D and -34% for Pandora#117 against S-5P TROPOMI, and of -60% for SkySpec-2D and -73% for Pandora#117 with respect to EOS-Aura OMI (not shown, coincidence criteria: 15 min, 20 km).

We can observe that SkySpec-2D and Pandora#117 have more similar biases (-25% and -34%, respectively) against TROPOMI than the bias found in the comparison between SkySpec-2D and Pandora#117 (-24%). This implies that the two instruments are affected by a lower bias near the satellite overpass time. This can be mainly due to the fact that near 1 PM, the position of the Sun determines a more similar viewing geometry between the two instruments than at other hours of the day, thus reducing possible differences due to errors in the AMFs.

Table 5.3 summarizes all the found biases between SkySpec-2D and the ground-based instruments during the two measurement campaigns.

Table 5.3: Relative bias and spread in $NO_2$ total VCDs retrieved from SkySpec-2D versus ground-based instruments for different locations.

| **Site (Month)** | **TROPOGAS** | **Ground-Based Pandora#117** |
|---|---|---|
| **Bologna (August)** | 9. ± 19% | |
| **BAQUNIN-La Sapienza (September)** | | -24. ± 23% at 254.5 K; -19. ± 21% at 298 K |

### 5.4.3 Routine measurements of SkySpec-2D at San Pietro Capofiume

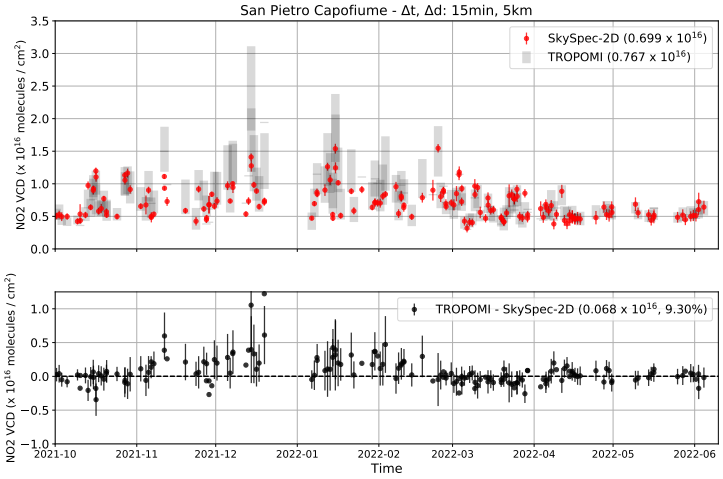


Figure 5.12: $NO_2$ total VCDs retrieved from SkySpec-2D (in red) and TROPOMI (grey shadows) at the "Giorgio Fea" observatory in SPC. SkySpec-2D data are averaged in 15 min around the S-5P overpass time. The TROPOMI shadows represent the mean values within the 5 km radius with standard deviations.

After the two inter-comparison campaigns, the SkySpec-2D system was installed in its final location, the "Giorgio Fea" observatory at SPC, on 1 October 2021. The "Giorgio Fea" meteorological station (Lat: 44.65° N, Lon: 11.62° E, Altitude: 11 m a.s.l., Figure 5.1) owned by the Agenzia regionale per la prevenzione, l'ambiente e l'energia dell'Emilia-Romagna (ARPAE) is a historic base founded in the early 1980s. The observatory, classified as rural

background, hosts one of the two meteorological ARPAE radars and is part of the Aerosol, Clouds and Trace Gases Research Infrastructure (ACTRIS) Italy network. Several measurement activities, such as micro-meteorological and project campaigns, are performed at the center.

In this work, the SkySpec-2D retrieved $NO_2$ total VCDs from the 1 October 2021 to the 4 June 2022 are considered. Since, according to [71], the effective temperatures representing the $NO_2$ total column is estimated to be about 270-280 K in polluted European regions, the cross-section at 298 K was used. Apart from the 14 November 2021, the period from the end of December 2021 to 4 January 2022 and some days during May 2022 (interruptions due to technical issues), the Skyspec-2D operated continuously. The average $NO_2$ total VCD is 0.70 x $10^{16}$ molecules/cm$^2$.

The comparison between TROPOMI data (averaged in a radius of 5 km around the "Giorgio Fea" observatory) and SkySpec-2D $NO_2$ total VCDs (averaged in a time interval of 15 min around the TROPOMI overpass time) is shown in Figure 5.12. As can be seen, the satellite and ground-based retrieved total VCDs behave similarly. The average difference between satellite and ground-based results is of the order of 9%.

Table 5.4: Relative bias and spread in $NO_2$ total VCDs retrieved from satellites versus ground-based instruments for different locations. The radius used for spatial coincidence is 5 km around the station for TROPOMI and 20 km for OMI, while the time interval is 15 or 60 min depending on instruments.

| **Site** | | **TROPOMI** | | | **OMI** | |
|---|---|---|---|---|---|---|
| **(Month)** | **TROPOGAS** | **Pandora#117** | **SkySpec-2D** | **TROPOGAS** | **Pandora#117** | **SkySpec-2D** |
| **Time Coinc.** | **60 min** | **15 min** | **15 min** | **60 min** | **15 min** | **15 min** |
| **Bologna** | | | | | | |
| **(August)** | -3. ± 29% | | -15. ± 17% | -12. ± 36% | | -22. ± 12% |
| **BAQUNIN-La Sapienza** | | | | | | |
| **(September)** | | -34. ± 32% | -25. ± 29% | | -73. ± 57% | -60. ± 57% |
| **SPC** | | | | | | |
| **(October-June)** | | | 9. ± 26% | | | |

Table 5.4 summarizes all the results of the comparison of satellite and ground-based retrieved $NO_2$ total VCDs for different locations, instruments and months. In general, the satellite data underestimate the $NO_2$ total VCDs with respect to the ground-based instruments in all locations for August, September, and October 2021. These differences are consistent with the well-known biases reported in the literature between $NO_2$ total VCDs derived from satellite and ground-based instruments. In [64], the comparison between TROPOMI and Pandora instruments reveals that TROPOMI underestimates the $NO_2$ total VCDs, mainly in polluted areas, by up to 40%. A similar bias affects OMI measurements in highly polluted conditions, by up to 50% [65]. Indeed, we found higher biases, in absolute values, in Rome,

where the pollution conditions are worse than in Bologna. Our results also reveal that the bias for OMI is, in absolute values, higher than for TROPOMI, mainly at La Sapienza (Rome). This is probably due to the low capability of OMI, due to its low spatial resolution, to properly detect polluted hot spots like Rome.

The only case where the satellite $NO_2$ total VCDs are higher than the corresponding SkySpec-2D ones is for the whole period from November to February in SPC, as can be seen from Figure 5.12. This is mainly related to the fact that our AMFs, simulated with $NO_2$ input profiles which contain low tropospheric amounts, differ a lot from the real AMFs, mainly during winter. Indeed, the Po Valley is known to be heavily polluted, mainly during the winter season, when thermal inversion conditions are usually present.

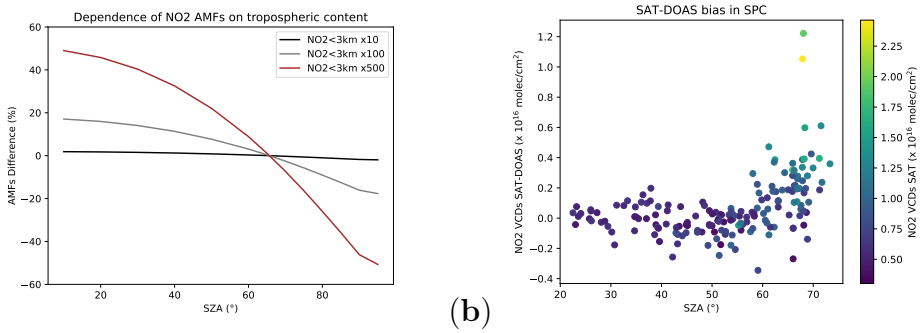


(a) (b)

Figure 5.13: (a) Percentage differences between $NO_2$ AMFs computed with increased $NO_2$ tropospheric content and not-perturbed profile. (b) Differences between $NO_2$ total VCDs measured by TROPOMI and SkySpec-2D in SPC as a function of the SZA and the $NO_2$ total VCDs measured by TROPOMI.

In Figure 5.13a, we recall the impact that high $NO_2$ concentrations in the lower troposphere have on the $NO_2$ AMFs, as already shown in Figure 4.5a. As we can see, the AMFs are biased in different ways depending on the SZA. In particular, the AMFs used for estimating the $NO_2$ total VCDs would be underestimated for low SZAs and overestimated for high SZAs in highly polluted conditions. Consequently, this would lead to an overestimation of the $NO_2$ total VCDs for low SZAs and an underestimation for high SZAs. In Figure 5.13b, we can see that the bias between TROPOMI and DOAS $NO_2$ total VCDs seems to agree with the previous considerations on the AMFs. Indeed, the bias increases with the SZAs and becomes large, mainly in highly polluted conditions. For low SZAs, the expected underestimation is less detectable because, as we can see, the $NO_2$ content is low. This observed

dependence of the $NO_2$ total VCDs on the SZAs is due to the fact that the TROPOMI overpass occurs almost at the same time, which corresponds to high SZAs during December and January and low SZAs in October and after March.

Another reason for the observed discrepancies during winter may be linked to the important spatial inhomogeneities in the $NO_2$ total VCDs observed by TROPOMI only during winter (see TROPOMI standard deviations in Figure 5.12). These spatial inhomogeneities may be related to the atmospheric conditions in the Po Valley that, during winter, are affected by low vertical and horizontal mixing, due to the presence of thermal inversion and low wind conditions. Indeed, SkySpec-2D, being located in a rural area far from streets and other local pollution sources, may be representative of a very local low-pollution condition.

# Chapter 6

# Retrieval of aerosol extinction and $NO_2$ vertical profiles in the Po Valley

After assessing the SkySpec-2D's performances through the two measurement campaigns described in Chapter 5, my colleagues and I installed the instrument at the "Giorgio Fea" observatory in SPC (see Figure 5.1) to acquire MAX-DOAS spectra. Although the $NO_2$ total VCDs retrieved in SPC from zenith spectra were already shown (see Figure 5.12), here the $NO_2$ vertical profiles from MAX-DOAS measurements will be retrieved for the first time in this thesis. Most of this work was performed during my period abroad at the Institute of Environmental Physics (IUP) of the University of Bremen, where I exploited their retrieval algorithm Bremen Optimal estimation REtrieval for Aerosols and trace gaseS (BOREAS) [78] for the retrieval of the vertical profiles. BOREAS is an important algorithm, indeed it was used to analyze the MAX-DOAS data acquired during the Cabaw Intercomparison of Nitrogen Dioxide measuring Instruments - 2 (CINDI-2) campaign [79].

## 6.1 MAX-DOAS measurement strategy

SkySpec-2D is continuously acquiring MAX-DOAS measurements at the "Giorgio Fea" observatory in SPC since the 1 October 2021. During all these months, its measurement strategy has remained unchanged except for the measurement azimuth directions. Indeed, my colleagues and I decided to modify them because the telescope, on the 23 March 2022, was moved and installed in its permanent position (a few meters away from the previous one) and the previously chosen viewing directions were not free from obsta-

cles anymore. The SkySpec-2D was permanently installed on the roof of the shelter containing the PC and spectrometers, as can be seen in Figure 5.1.

According to the settings chosen in the acquisition software MS-DOAS, fully compliant with the FRM4DOAS guidelines, SkySpec-2D performs three different kinds of measurements every day: calibration spectra, atmospheric spectra and horizon scans.

Table 6.1: Technical parameters for the calibration measurements during nighttime.

| | **Offset** | **Dark current** | **Hg** | **Hg* (only VIS)** |
|---|---|---|---|---|
| **Total integration time (s)** | 60 | 60 | 60 | 60 |
| **Exposure time (s)** | 0.01 | 10 | 0.28 (VIS), 0.36 (UV) | 10 |
| **Coadded spectra** | 6000 | 6 | 210 (VIS), 160 (UV) | 6 |

- The **calibration spectra** are automatically measured during the night, precisely when the SZA, directly computed by the MS-DOAS software, becomes higher than 100° (when the sun is 10° below the horizon). Once acquired, SkySpec-2D stops to measure until the SZA does not reach the chosen value to start the atmospheric acquisition (94°). The calibration spectra are important to correct the atmospheric spectra properly, as described in section 3.1.3, and consist of offset, dark current and emission lines of a Hg lamp mounted inside the instrument. All the Hg emission spectra are measured with a total integration time of 1 min. It is important to remember that every acquired spectrum is the sum of several single spectra, with the purpose of increasing the SNR. Every Hg spectrum is acquired with an exposure time of 0.28 s (0.36 s) in the VIS (UV) to obtain well defined emission peaks and prevent the CCD sensor's saturation. The different exposure times in VIS and UV are due to the different emission lines intensities in the two spectral ranges. As a consequence of these measurement times, a Hg spectrum in the VIS (UV) is the sum of about 210 (160) single spectra. However, as already explained in Section 3.1.3, we need to measure an additional VIS Hg spectrum with a higher exposure time of 10 s (only six co-added spectra). This allows to measure a third less intense emission line. The offset and dark current are needed to correct the counts in the acquired atmospheric spectra (see section 3.1.3). Since the offset is a constant signal automatically added to the spectra during the acquisition, we measure it using a total integration time of 1 min and a very low exposure time of 0.01 s (6000 co-added spectra). The dark current signal must be removed from the atmospheric spectra as well; we measure it with a total integration time of 60 s and an expo-

sure time of 10 s (6 co-added spectra). Information on the calibration measurements is summarized in Table 6.1.

Table 6.2: Technical parameters for the atmospheric measurements during daytime.

| | **Zenith acquisition** | **MAX-DOAS acquisition** |
|---|---|---|
| **SZA range (°)** | 94-85 | < 85 |
| **Total integration time (s)** | 50 (92° <SZA<94°)<br>40 (90° <SZA<92°)<br>30 (85° <SZA<90°) | 30 (80° <SZA<85°)<br>20 (SZA<80°) |
| **Exposure time (s)** | automatic | automatic |
| **Coadded spectra** | automatic | automatic |
| **Azimuth directions (°) (period)** | / | 120, 225, 300<br>(1/10/2021 - 23/03/2022)<br>135, 250, 315<br>(23/03/2022 - now) |
| **Elevation angles (°)** | 90 | 1,2,3,5,10,30,90 |

- The **atmospheric spectra** start to be acquired every morning when the SZA becomes lower than 94° (the sun is 4° below the horizon). At the beginning, the SkySpec-2D starts to acquire only zenith-sky spectra. When the SZA becomes lower than 85°, SkySpec-2D starts to perform MAX-DOAS measurements. During MAX-DOAS acquisitions, SkySpec-2D measures in three different azimuth directions: 120°, 225° and 300° from the 1 October 2021 to the 23 March 2022, and 135°, 250° and 315° afterwards. For each azimuth direction, spectra are acquired at the following elevation angles with respect to the horizon: 1°, 2°, 3°, 5°, 10°, 30° and 90°. The acquisition system automatically avoids measuring when the instrument viewing direction is close to the sun position (less than 5°). Each spectrum is acquired with a total integration time that depends on the SZA. I chose 50 s in the SZA range between 94° and 92°, 40 s between 92° and 90°, 30 s between 90° and 80°, and 20 s when SZA is lower than 80°. The purpose of increasing the total integration time at high SZAs is to increase the SNR of the measurements. Indeed, at high SZAs, the exposure time, automatically set in order to prevent the CCD sensor saturation, increases (less light) and the number of the co-added single spectra to sum up decreases, leading to a lower SNR.

  All the information is summarized in Table 6.2.

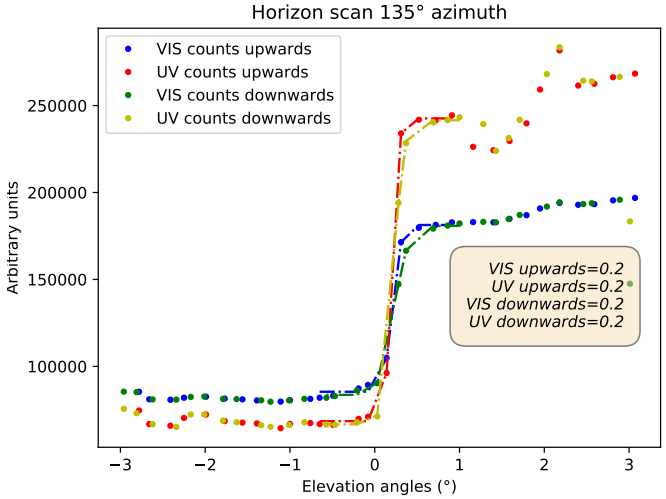


Figure 6.1: Mean values of the spectra (dots) for the four different datasets acquired during a horizon scan at 135° azimuth direction, during the day 2 April 2022. The dashed lines represent the theoretical "error functions" used to fit the data. The values in the legend represent the horizon positions, estimated as the centers of the theoretical functions, for the four datasets.

- **Horizon scans**. In the observation strategy, I implemented the horizon scans to be performed daily around noon. Since the true horizon positions in the three different azimuth angles do not change in time, horizon scans allow to assess the pointing stability of the SkySpec-2D, which is very important for reliable MAX-DOAS measurements. At this scope, for each of the three azimuth directions, VIS and UV spectra are acquired within the elevation angles range of ±3°, with a step of 0.2°, a fixed total integration time of about 1 s and 100 co-added spectra. This measurement strategy is applied twice for each azimuth direction, the first from -3° to +3° (upwards) and the second from +3° to -3° (downwards), in order to assess if systematic differences in the telescope movements occur between upwards and downwards scans. At the end of this process, four sets of data are available for each azimuth direction: two scans, upwards and downwards, each containing two other datasets, one in the UV and the other in the VIS. The spectra obtained every day during these scans are used to estimate the horizon position, according to the SkySpec-2D, exploiting the same strategy already used in Section 3.2.2 for the assessment of the TROPOGAS FOV. Low spectra values are expected to occur when the SkySpec-2D FOV is

completely covering the ground (low elevation angles), and higher values when the telescope is fully observing the sky. The transition region occurs at elevation angles where the instrument FOV partially covers the sky and the ground. Figure 6.1 shows an example of this procedure for the day 2 April 2022. Each dot represents the mean value of a specific spectrum with respect to the elevation angle. Each set of dots is fitted by an "error function" (the Gaussian integral function) around the maximum slope region that is assumed to represent the horizon position. I estimate the center of the fitted error function (equivalent to the center of the derivative Gaussian function), which is one of the fitted parameters, as the horizon position. As we can see in Figure 6.1, this method states that the horizon position on 2 April 2022 at 135° azimuth direction is 0.2° for all the four different datasets.

The acquired spectra are then calibrated and converted into NetCDF files as described in section 3.1.3.

## 6.2 Processing method

### 6.2.1 SCDs fit

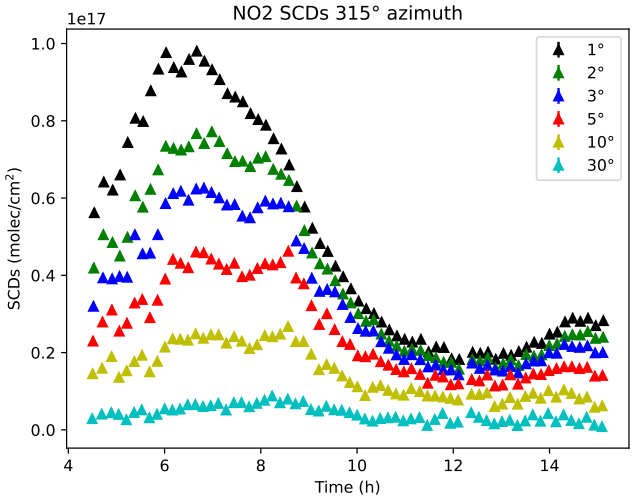


Figure 6.2: $NO_2$ SCDs estimated by the QDOAS software from spectra acquired on 16 May 2022, at 315° azimuth and all the elevation angles. The reported time is UTC.

As discussed in Section 2.5, even though the final target is represented by the $NO_2$ vertical profiles, the $O_4$ SCDs are important because they give information on the aerosol extinction profiles which heavily affect the BOX-AMFs. All the spectra were processed with the QDOAS software to retrieve the $NO_2$ and $O_4$ SCDs. The QDOAS analysis method is slightly different compared to the one used in Chapters 4 and 5, indeed all the spectra of each scan are analyzed with respect to the zenith-sky spectrum of the same scan, instead of a fix reference spectrum. This strategy allows to make negligible the stratospheric contribution because all the off-axis measurements (analyzed spectra) and the zenith-sky spectrum (reference spectrum) contain the same stratospheric absorption. Indeed, the stratospheric path does not depend on the measurement elevation angle and moreover, the analyzed and reference spectra are very close in time (within 2 minutes). Apart from this difference, all the parameters of the QDOAS fit are identical to the ones used for the SkySpec-2D during the measurement campaign in Bologna against TROPOGAS (see Table 5.2). An example of $NO_2$ SCDs fitted during the day 16 May 2022 from measurements in SPC is reported in Figure 6.2.

### 6.2.2 Retrieval with BOREAS

The retrieval of the $NO_2$ and aerosol extinction profiles was performed with BOREAS [78], the algorithm developed at the IUP institute of the University of Bremen, exploiting the fitted $NO_2$ and $O_4$ SCDs. As a first step, all the SCDs files were converted into the BOREAS format. In general, the retrieval strategy of BOREAS is very similar to the one described in Section 2.5. First, the aerosol extinction profile is retrieved exploiting the Optimal Estimation (OE) method [80] through the convergence between measured and simulated $O_4$ SCDs, starting from an a-priori profile. Then, the BOX-AMFs are directly computed by the SCIATRAN RTM and are used in the following step, together with the $NO_2$ SCDs, when the OE method is exploited again to retrieve the $NO_2$ vertical profile from an a-priori one. The chosen aerosol extinction and $NO_2$ a-priori profiles decrease exponentially with altitude. However, since the tropospheric conditions can present high variabilities, the used a-priori profiles are not fixed. In particular, for the aerosol extinction, the retrieval divides into two steps: a first retrieval is performed with a fixed a-priori profile that decreases exponentially with altitude; then, the fixed a-priori profile is scaled to the aerosol optical thickness (aerosol extinction profile integrated along the vertical) retrieved in the first step and is used as a-priori profile for a second retrieval. On the other hand, the retrieval of the $NO_2$ vertical profile is performed in one step and the fixed exponentially decreasing a-priori profile is scaled to the $NO_2$ SCD measured at the elevation

angle of 30°. An example of the a-priori profiles used for the retrieval on 16 May 2022 is provided in Figure 6.3.

The BOREAS algorithm was used to process the whole period between 1 October 2021 and 13 June 2022. A vertical grid of 100 m steps between 0 and 4 km and a constant surface albedo of 0.06 were used.

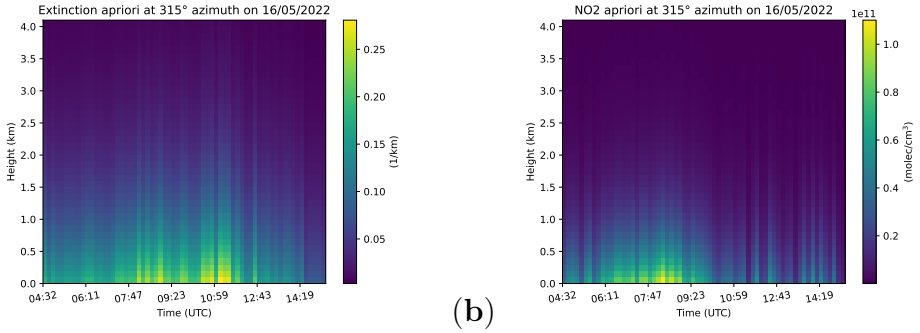


(a) (b)

Figure 6.3: Aerosol extinction (a) and $NO_2$ (b) a-priori profiles used for the BOREAS retrieval on 16 May 2022 in the azimuth direction of 315°.

### 6.2.3 AKs

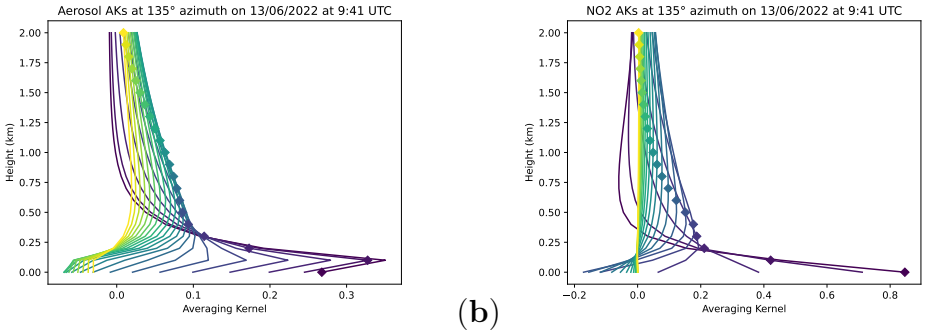


(a) (b)

Figure 6.4: Averaging kernels of the aerosol extinction (a) and $NO_2$ (b) vertical profiles retrieved with BOREAS from a MAX-DOAS scan acquired by SkySpec-2D in SPC on 13 June 2022 at 9:41 UTC. Each diamond represents the retrieval vertical point associated to the AK.

The Averaging Kernels (AKs) matrix represents a measure of the sensitivity of the retrieved state vector to the true state of the atmosphere. Within an ideal retrieval, the AKs matrix would be the identity matrix because the retrieval in a certain layer would depend only on the true state of that

layer. However, a real retrieval is different because each measurement is sensitive to several atmospheric layers. In particular, the broadness of the AKs represents the vertical resolution of the retrieval while the peak is the vertical layer where most of the information comes from. In Figure 6.4, an example of the AKs for the retrieval of aerosol extinction (a) and $NO_2$ (b) vertical profiles on 13 June 2022 is shown for altitudes lower than 2 km. Each line represents the AK relative to a specific retrieval vertical point (indicated by the diamond symbol). The plot shows that the AKs are very broad, mainly at high altitudes, where the retrieval sensitivity is low. At low altitudes, the AKs are sharper with peaks of 0.3 and 0.8 for the retrieval of aerosol extinction and $NO_2$ vertical profiles, respectively.

The trace of the AKs matrix represents the number of the Degrees Of Freedom (DOFs) that are the independent pieces of information contained in one retrieved vertical profile. In this case, the DOFs assume values of about 1.7 and 2.8 for aerosol extinction and $NO_2$ vertical profiles, respectively, as shown in the example in Figure 6.5.

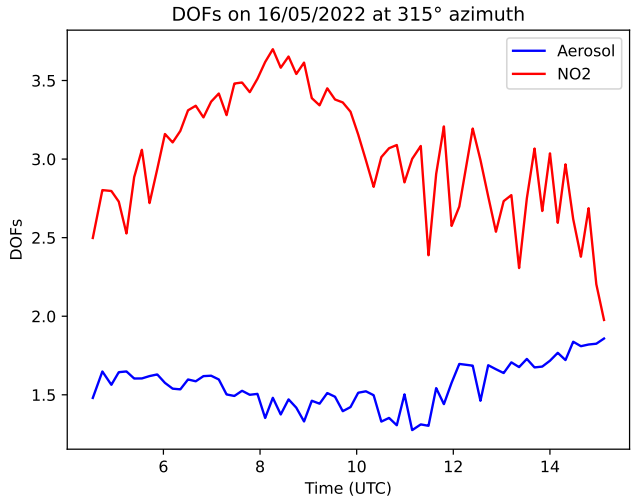


Figure 6.5: DOFs in the retrieved Aerosol extinction (blue) and $NO_2$ (red) profiles computed by BOREAS as a function of time. Example of 16 May 2022 at 315° azimuth.

### 6.2.4 Aerosol extinction and $NO_2$ vertical profiles

In Figure 6.6, the aerosol extinction (a) and $NO_2$ (b) vertical profiles retrieved by BOREAS from SkySpec-2D MAX-DOAS measurements acquired during the day 16 May 2022 in the azimuth direction at 315°, are reported. The

errors estimated by BOREAS, as explained in [78], are shown in the plots (a) and (b) of Figure 6.7.

For each day of measurements, these quantities are retrieved also in the other two azimuth directions (see Table 6.2) scanned by the SkySpec-2D. The quality of these results has been tested through comparisons with both in-situ and satellite data, as will be reported in the following two sections.

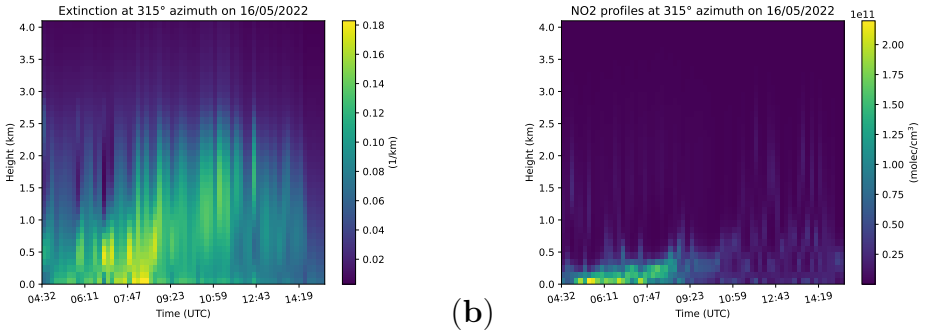


(a) (b)

Figure 6.6: Aerosol extinction (a) and $NO_2$ (b) vertical profiles retrieved by BOREAS during the day 16 May 2022 in the azimuth direction of 315°.

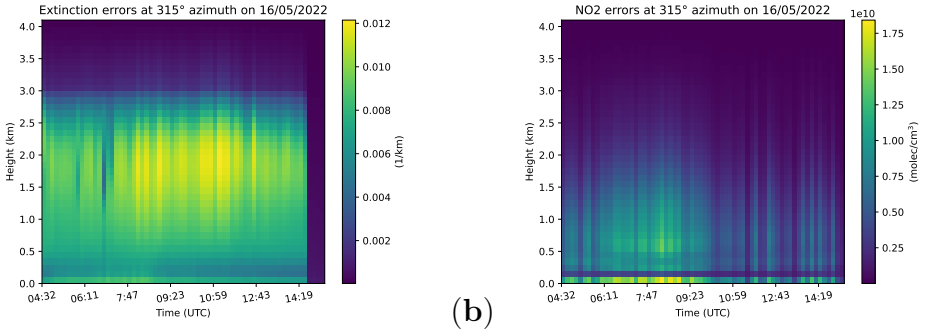


(a) (b)

Figure 6.7: Errors in aerosol extinction (a) and $NO_2$ (b) vertical profiles retrieved by BOREAS during the day 16 May 2022 in the azimuth direction of 315°.

## 6.3 Comparison with in-situ data

The lowest points of the retrieved $NO_2$ vertical profiles were compared to the in-situ $NO_2$ concentrations measured by the ARPAE in SPC, a few meters far from the SkySpec-2D. ARPAE data have been freely downloaded from `https://sdati-test.datamb.it/arex/`.

Since the $NO_2$ in-situ concentrations are provided as hourly averages, the lowest points of the vertical profiles are averaged in the same time grid, for each of the three azimuth directions scanned by SkySpec-2D.

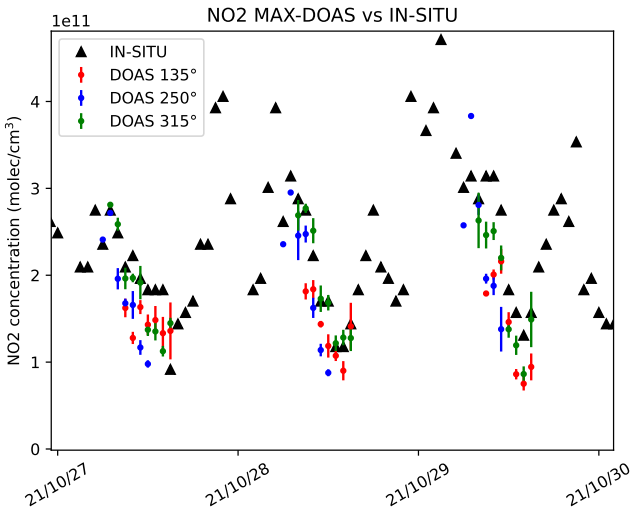


Figure 6.8: Timeseries of in-situ (black triangles) and MAX-DOAS $NO_2$ concentrations in the three azimuth directions (colored dots) during three days of October 2021. The error bars represent the standard deviations of the mean values.

Figure 6.8 shows the $NO_2$ in-situ concentrations measured by ARPAE and retrieved from SkySpec-2D measurements, in the three azimuth directions, for the days 27, 28 and 29 October 2021. A general good agreement exists between the different data both in values and behavior. Indeed, both datasets see the $NO_2$ concentrations decreasing during the day and increasing in the afternoon. As already highlighted in Section 1.4, MAX-DOAS data are missing during nighttime due to the lack of VIS and UV radiation.

The scatterplots between the ARPAE and MAX-DOAS $NO_2$ concentrations measured from 1 October 2021 to 13 June 2022, are reported in Figure 6.9 for the three SkySpec-2D's measurement azimuth angles. Although the nature of the two measurement methods is completely different, the plots show a general good agreement, with correlation coefficients of almost 0.8 in the directions 135° and 315°. In particular, the best correlation is found at 135°, which represents the measurement direction closest to the in-situ instrument position. On the other hand, worst results occur around the direction at 250° with a correlation of 0.58.

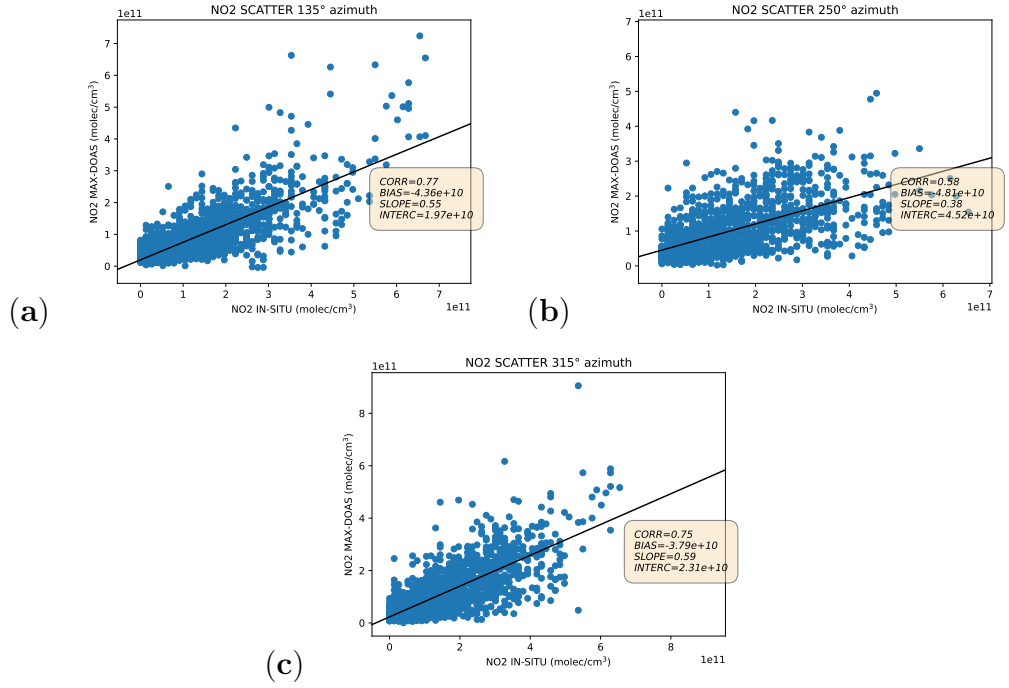


Figure 6.9: Scatterplots between in-situ and MAX-DOAS $NO_2$ concentrations retrieved from the three scanned azimuth directions within the retrieval period from 1 October 2021 to 13 June 2022. The fitting correlation line is reported in black. Even though the indicated azimuth agles are 135°, 250° and 315°, we remind that they were slightly different before 23 March 2022, as reported in Table 6.2.

The found biases are of the order of -4x$10^{10}$ molecules/$cm^3$, with the MAX-DOAS data underestimating the ground concentrations, mainly for high values. The lowest bias, in absolute value, is found at 315° azimuth.

The negative bias and the data scattering, present in all the three directions, is mainly due to the differences in the two measurement techniques that do not allow to sound the same portion of the air. Indeed, while in-situ measurements provide punctual information around the instrument, the MAX-DOAS $NO_2$ concentrations represent a wider region both in the horizontal and vertical directions. In particular, focusing in the vertical direction, the AK relative to the lowest retrieved point in Figure 6.4b shows that, although it is peaked at the ground, with a value higher than 0.8, it is not a delta function and presents not negative values up to about 300 m. This means that the retrieved ground value does not represent only the concentration at the ground level but also the average value in a vertical interval of few hundred meters, where $NO_2$ concentration is usually lower. This is

the reason why the MAX-DOAS $NO_2$ concentrations at the ground are, on average, underestimated with respect to the in-situ measurements.

## 6.4 Comparison with TROPOMI data

In this comparison exercise, the $NO_2$ tropospheric VCDs were computed from the MAX-DOAS retrieved vertical profiles and compared with the $NO_2$ tropospheric VCDs derived from TROPOMI satellite measurements. The TROPOMI data already described in Section 5.3.2 were used. For the comparison, all the satellite data within a radius of 20 km around the SkySpec-2D position (Giorgio Fea observatory in SPC) were averaged and, for each azimuth direction, all the MAX-DOAS tropospheric VCDs whitin a time range of $\pm$ 5 min around the satellite overpass time were averaged.

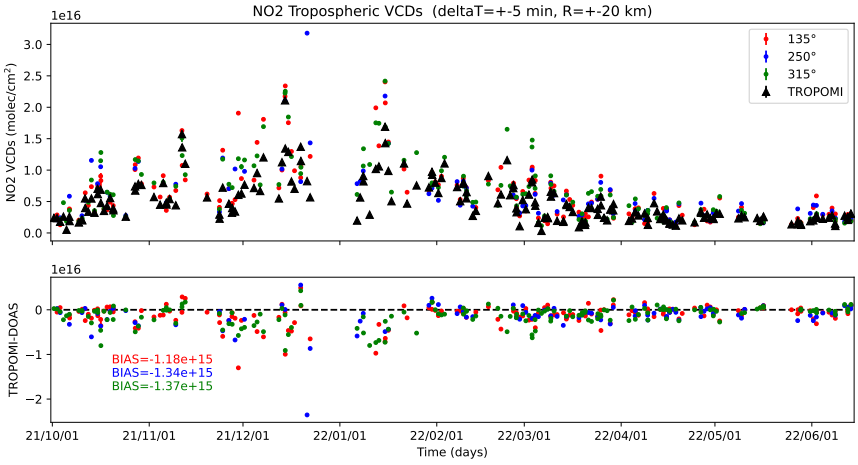


Figure 6.10: Timeseries of $NO_2$ tropospheric VCDs measured by TROPOMI (black triangles) and computed from the retrieved MAX-DOAS vertical profiles in the three azimuth directions (colored dots) for the whole retrieval period. Even though the indicated azimuth agles are 135°, 250° and 315°, we remind that they were slightly different before 23 March 2022, as reported in Table 6.2. Differences between TROPOMI and MAX-DOAS, for each azimuth direction, are shown in the bottom panel with the symbols of the same colors.

The timeseries of the TROPOMI and MAX-DOAS $NO_2$ tropospheric VCDs for the whole retrieval period is shown in Figure 6.10. The two datasets

present a good agreement, mainly for low $NO_2$ tropospheric VCDs (the first days of October 2021 and after March 2022). Both instruments see a $NO_2$ concentration increase during the winter period, when the Po Valley experiences a high number of stable and foggy days. However, in this period, larger biases, in absolute value, are present, with TROPOMI underestimating the $NO_2$ tropospheric VCDs. The biases for the whole dataset are of the order of -$10^{15}$ molecules/cm$^2$ with the best and worst results in the azimuth directions at 135° and 315°, respectively.

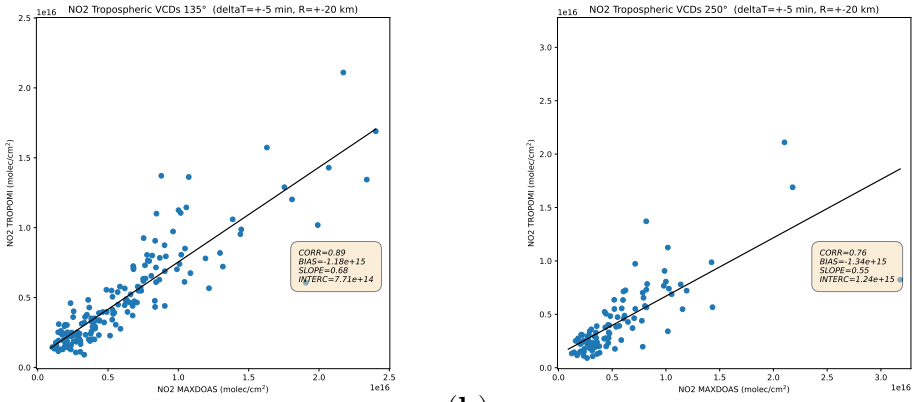


(**a**) (**b**)

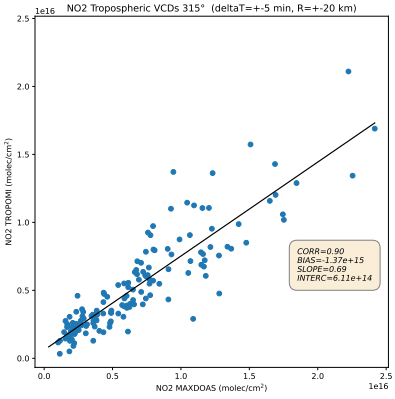


(**c**)

Figure 6.11: Scatterplots between $NO_2$ tropospheric VCDs measured by TROPOMI and the ones computed from the retrieved MAX-DOAS vertical profiles in the three scanned azimuth directions for the whole retrieval period. Even though the indicated azimuth agles are 135°, 250° and 315°, we remind that they were slightly different before 23 March 2022, as reported in Table 6.2.

Figure 6.11 shows the scatterplots between the same TROPOMI and MAX-DOAS averaged data for the three azimuth directions. Even though the scatterplots present high correlations, of the order of 0.9, they show again that TROPOMI tends to underestimate high $NO_2$ tropospheric VCDs.

A possible source of bias could be the different a-priori profiles used in the two analyses. TROPOMI uses profiles computed by the Chemical Transport Model (CTM) Tracer Model version 5 - Massively Parallel (TM5-MP) [81], while we use the a-priori profiles described in Section 6.2.2. To make the performed comparison independent from them, the AKs of the TROPOMI retrieval, available whitin the products, can be exploited because they allow to correct the TROPOMI data replacing the a-priori profiles used for the retrieval with our profiles. Therefore, in order to remove the dependence of the comparison on the a-priori profiles, I decided to replace them with the MAX-DOAS retrieved $NO_2$ vertical profiles, as performed also in [82].

According to [83, 74], the TROPOMI $NO_2$ tropospheric VCDs can be corrected with the following formula:

$$VCD_{corr} = \frac{AMF_{tropo}}{AMF_{tropo}^{'}} VCD \tag{6.1}$$

where $AMF_{tropo}$ is the tropospheric AMF, directly provided in the TROPOMI data and computed from the TM5-MP a-priori profiles, while $AMF_{tropo}^{'}$ is the tropospheric AMF according to the new a-priori profiles. This quantity can be computed from the tropospheric AKs ($AK_{tropo}$), the tropospheric AMFs ($AMF_{tropo}$) relative to the TM5-MP a-priori profiles, and the new vertical profiles ($x^{'}$) (see [74]) as:

$$AMF_{tropo}^{'} = AMF_{tropo} \frac{\sum_l AK_{tropo,l} x_l^{'}}{\sum_l x_l^{'}} \tag{6.2}$$

where the sums are performed over all the vertical points and $AK_{tropo}$ is not null below the tropopause and is computed as:

$$AK_{tropo} = \frac{AMF_{tot}}{AMF_{tropo}} AK_{tot} \tag{6.3}$$

In particular, for each satellite overpass time and for each azimuth direction, I computed the MAX-DOAS $NO_2$ mean vertical profile within the $\pm 5$ min range. I used it to correct all the TROPOMI $NO_2$ tropospheric VCDs within the 20 km radius and then I computed the satellite mean value to compare with the MAX-DOAS tropospheric column estimated from the vertical profile.

Figure 6.12 shows the scatterplots between the MAX-DOAS $NO_2$ tropospheric VCDs and the ones measured by TROPOMI, corrected for the a-priori profiles as described above. It is evident that the TM5-MP a-priori profiles assumed for TROPOMI have an impact on the negative biases found in Figure 6.11. However, even though the biases decreased, in absolute values, they changed sign becoming of the order of $8x10^{14}$ molecules/cm$^2$. It must be also mentioned that all the three correlation coefficients have slightly decreased with respect to the results obtained with the original TROPOMI data.

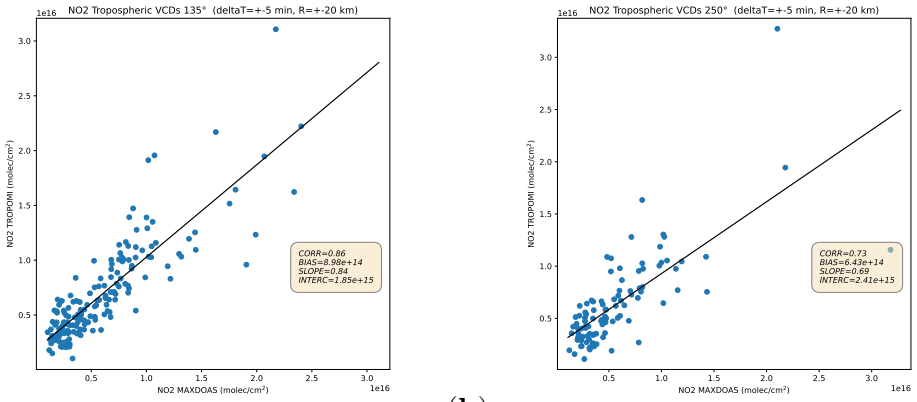


(**a**)




(**b**)

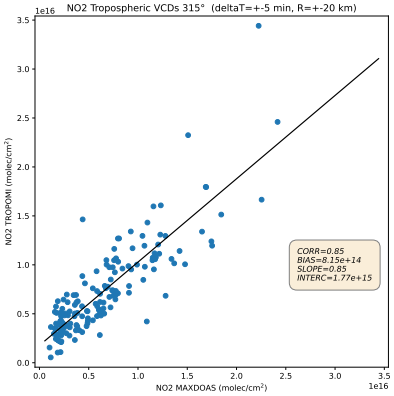


(**c**)

Figure 6.12: Scatterplots between TROPOMI $NO_2$ tropospheric VCDs, corrected for the a-priori profiles, and the ones computed from the retrieved MAX-DOAS vertical profiles in the three scanned azimuth directions for the whole retrieval period. Even though the indicated azimuth agles are 135°, 250° and 315°, we remind that they were slightly different before 23 March 2022, as reported in Table 6.2.

# Chapter 7

# Conclusions

The main target of this PhD thesis is the retrieval of atmospheric minor trace species exploiting ground-based measurements of VIS and UV atmospheric spectra. This is possible through the DOAS technique, widely used from the last years of the nineteenth century, when the first studies on stratospheric ozone were performed. These ground-based DOAS measurements are important because they provide alternative information on the trace gases concentrations compared to in-situ and satellite data. The retrieved trace gases total VCDs and vertical profiles from ground-based spectra are indeed suitable to perform studies that require the vertical structure of the concentrations to be resolved and data with a high temporal resolution (about few minutes).

In chapter 2, I illustrated the DOAS technique. In particular, I mentioned that it is based on the differential molecular absorption, which is divided from all the other broad-band contributions to the optical paths (Section 2.1). Moreover, we saw all the mathematical assumptions and approximations that allow to fit the SCDs from the measured spectra (Section 2.2), the software QDOAS used in this thesis to fit the SCDs (Section 2.3) and the procedures to retrieve total VCDs and vertical profiles from zenith-sky (Section 2.4) and MAX-DOAS measurements (Section 2.5), respectively.

In Chapter 3, I described the three ground-based MAX-DOAS instruments that have been used during this PhD: SkySpec-2D (Section 3.1), TROPOGAS (Section 3.2) and GASCOD/NG4 (Section 3.3). TROPOGAS and GASCOD/NG4 are two custom-built instruments, developed in the 90s at the CNR-ISAC. Although they provide reliable atmospheric spectra, their data were not fully exploited in the last years, consequence of a decrease of interest for the DOAS field at the CNR-ISAC and in general in Italy, differently from other parts of Europe (mainly Germany and Belgium), where the research in this topic has continued to play an important role, leading to

innovations in the DOAS measurement strategies and processing methods. For this reason, we decided to start from the Italian DOAS heritage for the future development and exploitation of this research field in Italy. For this purpose, I characterized the TROPOGAS performances in terms of SNR and FOV and I changed its measurement strategy in order to meet as much as possible the international standards provided by the FRM4DOAS community (Section 3.2.2). The results showed that TROPOGAS is able to meet all the FRM4DOAS requirements except the FOV which is too wide (3.6° against the required 1.5°).

Since SkySpec-2D, bought by the CNR-ISAC in May 2021, is a new FRM4DOAS-compliant MAX-DOAS instrument, we decided to exploit it to create the first Italian MAX-DOAS measurement site compliant to the standard requirements. For this instrument, I developed an automatic processing chain that calibrates its measured spectra and writes them into NetCDF files, as required by the FRM4DOAS community (Section 3.1.3). This approach, that has been subsequently applied also to TROPOGAS and GASCOD/NG4, is important because allows us to deliver the SkySpec-2D's processed spectra to the FRM4DOAS community for their central processing and for being officially included in their satellite validation network.

One of the main works that I performed during the PhD is the characterization, in terms of $NO_2$ and $O_3$ total VCDs, of the ECO observatory at the CNR-ISAC in Lecce, from the zenith-sky spectra measured by GASCOD/NG4 (Chapter 4). After the retrieval of the $NO_2$ and $O_3$ total VCDs, described in Section 4.1, I realized that their diurnal variabilities were affected by important systematic effects due to errors in the estimated SCDs in the reference spectra, and mainly to errors in the simulated AMFs used to convert the SCDs into total VCDs, as shown in Section 4.1.4. For this reason, I avoided to make considerations, in terms of absolute values and behavior, on the $NO_2$ and $O_3$ total VCDs. However, comparing their diurnal behaviors in different days, we can understand if a real day-to-day variability exists. In particular, I found out that, although two different days (14 and 22 July 2018) present very similar $O_3$ total VCDs diurnal behaviors, the $NO_2$ total VCDs are characterized by very different trends and high temporal variability (see Section 4.2.1). This result suggests that, while the $O_3$ total VCDs are dominated by the stratospheric content, where the $O_3$ concentration is maximum and the variability is lower, the $NO_2$ total VCDs contain an important tropospheric signal, consequence of the anthropogenic activity. Despite the presence of important systematic errors, conclusions on differences between the total VCDs measured in the afternoon and morning can be drawn. Considering only data acquired when the SZA is between 60° and 90° (the same SZA range in the morning and afternoon mitigates the

systematic errors that heavily depend on the SZA), we obtain a $O_3$ total VCDs diurnal decrease of -7.5x$10^{17}$ molecules/cm$^2$, on average, and a $NO_2$ total VCDs diurnal increase of 5.1x$10^{14}$ molecules/cm$^2$, on average, with this positive trend probably related to the diurnal photolysis of the stratospheric $N_2O_5$.

The important presence of tropospheric content in the $NO_2$ total VCDs is further demonstrated through an analysis with respect to the different days of the week (see Section 4.2.2). In particular, I computed a daily total VCDs anomaly for each day of measurements, as the mean diurnal total VCD minus the 7-days running mean total VCD. This analysis shows that Sundays, characterized by a general lower traffic around the ECO observatory, present a significant mean $NO_2$ total VCDs anomaly of about -6x$10^{14}$ molecules/cm$^2$. The same analysis performed with the in-situ $NO_2$ concentrations, measured by a gas analyzer, confirmed this result. On the other hand, the same analysis performed for the $O_3$ total VCDs and in-situ concentrations shows less clear and significant results.

The same anomalies are analyzed in relation to the wind measured at the ECO observatory at an altitude of 20 m (see Section 4.2.3). While no significant result is found for the $O_3$ total VCDs, confirming again the lack of tropospheric signal in the $O_3$ columns, the $NO_2$ total VCDs anomalies show a decreasing trend with the wind speed, confirmed by the in-situ measurements, suggesting the presence of $NO_2$ local production. However, a transport component from Lecce in the $NO_2$ total VCDs is also present. This is highlighted by the significant positive anomaly peak present in corrispondence of the NE wind direction, where Lecce is located with respect to the ECO observatory. However, this transport direction is not confirmed by the in-situ $NO_2$ concentrations, that are sensitive to more local emissions.

The $NO_2$ and $O_3$ total VCDs monthly averages show values between 3.5x$10^{15}$ and 7x$10^{15}$ and between 7.5x$10^{18}$ and 1x$10^{19}$ molecules/cm$^2$, respectively, with peaks reached during Summer, for the $NO_2$, and Spring, for the $O_3$.

As last step, to assess the quality of the retrieved $NO_2$ and $O_3$ total VCDs, I compared them with the ones measured by OMI and TROPOMI satellite instruments (see Section 4.3). In particular, I considered all satellite data within a 20 km radius around the ECO observatory, in order to improve the statistical significance. I found out that, in agreement with other studies in literature, satellites underestimate the $NO_2$ total VCDs of about 30% with respect to ground-based data, with a more evident underestimation for the high values. Such agreement with literature studies is also present for the $O_3$ total VCDs that are underestimated by the satellites of about 3/4%. I have also verified the robustness of these results, that do not significantly

change when the radius, used to discriminate the satellite data around ECO, is decreased to 10 and 5 km. However, a more detailed analysis revealed that the found biases present a seasonal dependence, probably partially due to the systematic errors in the simulated AMFs.

This study, related to the ECO observatory, provided a detailed characterization of the site in terms of the retrieved $NO_2$ and $O_3$ total VCDs and showed its potential to become important for satellite validation purposes.

The other important work of this PhD has been performed in the frame of an ESA project, with the purpose to create the first Italian FRM4DOAS-compliant MAX-DOAS site in the Po Valley (see Chapter 5). To achieve our goal, we decided to exploit the instrument SkySpec-2D, whose performances have been assessed through two measurement campaigns: the first one against TROPOGAS, on the roof of the CNR-ISAC in Bologna, and the second one against the Pandora#117, in the BAQUNIN supersite located on the roof of the La Sapienza University in Rome. In particular, we compared the $NO_2$ total VCDs retrieved from their measurements, as explained in Section 5.2. The campaign taken place in Bologna showed that, during the campaign period (August 2021), the SkySpec-2D $NO_2$ total VCDs were higher than the TROPOGAS ones of about $0.57 \text{x} 10^{15}$ molecules/cm$^2$ (9%), with a correlation coefficient of 0.77 (see Section 5.4.1). The found bias is fully consistent with the systematic errors coming from the retrieval procedure and the not-perfect correlation is consequence of instrumental differences (different FOVs and measurement integration times). In agreement with literature, satellites (OMI and TROPOMI) underestimate the $NO_2$ total VCDs. In particular TROPOMI results are 15% and 3% lower than the SkySpec-2D's and TROPOGAS's ones, respectively. The underestimations increase, in absolute value, to 22% and 12%, for the comparison with OMI which has a coarser spatial resolution.

The second campaign in Rome, against the Pandora#117, showed a very high correlation (0.9) between the SkySpec-2D and Pandora#117 retrieved $NO_2$ total VCDs (see Section 5.4.2). However, in this case, I found a higher bias, in absolute value, than the one found in the other campaign, with SkySpec-2D underestimating the $NO_2$ columns, compared to Pandora#117, of about 20%. The reason is that, in addition to the instrumental differences present also in the other campaign, SkySpec-2D and Pandora#117 adopt two different measurement geometries, leading to not-negligible errors due to the simulated AMFs. Indeed, while the SkySpec-2D measures zenith-sky spectra, Pandora#117 acquires the direct solar light. It is important to say that the mentioned bias was found with similar temperatures of the $NO_2$ cross-sections used for the SkySpec-2D and Pandora#117 analyses because I found out that the cross-section temperature heavily affects the final results.

Also in this case, the satellite data underestimate the $NO_2$ total VCDs. In particular, TROPOMI (OMI) values are lower than the SkySpec-2D's and Pandora#117's ones of about 25% (60%) and 34% (73%), respectively. Since Rome has higher levels of pollution than Bologna, the satellite underestimation is more important in this second campaign, in agreement with the literature.

Assessed its performances, we installed the SkySpec-2D in its final position at the Giorgio Fea observatory in SPC, where it is measuring MAX-DOAS spectra since the 1 October 2021. This instrument represents the first FRM4DOAS-compliant MAX-DOAS system in Italy. The $NO_2$ total VCDs, retrieved from its zenith-sky spectra, show a good agreement with the TROPOMI data. However, differently from what reported in literature and from the results of the two measurement campaigns, SkySpec-2D underestimates the $NO_2$ total columns of about 9%, on average, with respect to TROPOMI. The underestimation is more pronounced during winter, due to the AMFs systematic errors.

In Chapter 6, I exploited the SkySpec-2D's MAX-DOAS spectra to retrieve the aerosol extinction and $NO_2$ vertical profiles in SPC. Since, we do not have a such retrieval algorithm yet, I performed this work during my period abroad at the IUP institute of the University of Bremen, exploiting their algorithm BOREAS (see Section 6.2). To assess the retrieval quality, I compared the lowest points of the $NO_2$ vertical profiles with the $NO_2$ in-situ concentrations measured at SPC by ARPAE (see Section 6.3). The results present a good agreement with correlation coefficients of 0.77, 0.58 and 0.75 for the three MAX-DOAS measurement azimuth directions of 135°, 250° and 315°, respectively. However, the MAX-DOAS concentrations are underestimated of $4x10^{10}$ molecules/$cm^3$, on average, and mainly when the ground concentrations are high, due to the coarse vertical resolution of the MAX-DOAS retrieval. The $NO_2$ vertical profiles are then used to compute the tropospheric VCDs, that I compared with the TROPOMI ones (see Section 6.4). Even though I found high correlations of about 0.9, TROPOMI underestimates the $NO_2$ tropospheric columns of about $10^{15}$ molecules/$cm^2$. Correcting the TROPOMI data, replacing the a-priori profiles used for the TROPOMI retrieval with the ones retrieved from the MAX-DOAS measurements, I made the comparison independent on the TROPOMI a-priori assumptions, verifying that they played a not-negligible role in the found negative biases.

In the future, the $NO_2$ and $O_3$ total VCDs over Bologna (from TROPOGAS) and over the ECO site in Lecce (from GASCOD/NG4), routinely retrieved thanks to this PhD work, can be further exploited for scientific studies on air quality. The same is true for the $NO_2$ vertical profiles retrieved in

the Po Valley. In particular, the preliminary retrieved profiles suggest that SPC does not seem to be affected by local emission hot spots like cities or industries, making the site very important for satellite validation and for representing the general pollution situation in the Po Valley. At the moment my colleagues and I are developing our own vertical profiles retrieval algorithm, that will allow us to investigate deeper the $NO_2$ situation in the Po Valley and to extend the retrieval also to other pollutants.

Moreover, we installed another SkySpec-2D instrument at the CNR-ISAC in Tor Vergata (Rome) during Autumn 2021. Exploiting my tools, its data will be processed in the future, in the same way shown in SPC.

# List of Figures

# List of Tables

# Bibliography


[1] D. W. Kweku, O. Bismark, A. Maxwell, K. A. Desmond, K. B. Danso, E. A. Oti-Mensah, A. T. Quachie, and B. B. Adormaa. Greenhouse effect: greenhouse gases and their impact on global warming. *Journal of Scientific research and reports*, 17(6):1–9, 2018.

[2] D. A. Lashof and D. R. Ahuja. Relative contributions of greenhouse gas emissions to global warming. *Nature*, 344(6266):529–531, 1990.

[3] J. M. Wallace and P. V. Hobbs. *Atmospheric science: an introductory survey*, volume 92. Elsevier, 2006.

[4] K. O. Yoro and M. O. Daramola. Co2 emission sources, greenhouse gases, and the global warming effect. In *Advances in carbon capture*, pages 3–28. Elsevier, 2020.

[5] H. S. Baker, R. J. Millar, D. J. Karoly, U. Beyerle, B. P. Guillod, D. Mitchell, H. Shiogama, S. Sparrow, T. Woollings, and M. R. Allen. Higher co2 concentrations increase extreme event risk in a 1.5 c world. *Nature Climate Change*, 8(7):604–608, 2018.

[6] J. C. Farman, B. G. Gardiner, and J. D. Shanklin. Large losses of total ozone in antarctica reveal seasonal clox/nox interaction. *Nature*, 315(6016):207–210, 1985.

[7] Montreal Protocol et al. Montreal protocol on substances that deplete the ozone layer. *Washington, DC: US Government Printing Office*, 26:128–136, 1987.

[8] J. A. Mäder, J. Staehelin, T. Peter, D. Brunner, H. E. Rieder, and W. A. Stahel. Evidence for the effectiveness of the montreal protocol to protect the ozone layer. *Atmospheric Chemistry and Physics*, 10(24):12161–12171, 2010.

[9] A. S. Lefohn, C. S. Malley, L. Smith, B. Wells, M. Hazucha, H. Simon, V. Naik, G. Mills, M. G. Schultz, E. Paoletti, A. De Marco, X. Xu, L. Zhang, T. Wang, H. S. Neufeld, R. C. Musselman, D. Tarasick, M. Brauer, Z. Feng, H. Tang, K. Kobayashi, P. Sicard, S. Solberg, and G. Gerosa. Tropospheric ozone assessment report: Global ozone metrics for climate change, human health, and crop/ecosystem research. *Elementa: Science of the Anthropocene*, 6, 2018.

[10] A. Chaloulakou, I. Mavroidis, and I. Gavriil. Compliance with the annual no2 air quality standard in athens. required nox levels and expected health implications. *Atmospheric Environment*, 42(3):454–465, 2008.

[11] J. Schwartz. Particulate air pollution and daily mortality in detroit. *Environmental Research*, 56(2):204–213, 1991.

[12] A. A. Lacis, D. J. Wuebbles, and J. A. Logan. Radiative forcing of climate by changes in the vertical distribution of ozone. *Journal of Geophysical Research: Atmospheres*, 95(D7):9971–9981, 1990.

[13] P. M. de F. Forster and K. P. Shine. Radiative forcing and temperature trends from stratospheric ozone changes. *Journal of Geophysical Research: Atmospheres*, 102(D9):10841–10855, 1997.

[14] V. A. Mohnen, W. Goldstein, and W.-C. Wang. Tropospheric ozone and climate change. *Air & Waste*, 43(10):1332–1334, 1993.

[15] P. J. Crutzen. Tropospheric ozone: An overview. *Tropospheric ozone*, pages 3–32, 1988.

[16] J. F. Noxon. Tropospheric no2. *Journal of Geophysical Research: Oceans*, 83(C6):3051–3057, 1978.

[17] D. W. Bond, R. Zhang, X. Tie, G. Brasseur, G. Huffines, R. E. Orville, and D. J. Boccippio. Nox production by lightning over the continental united states. *Journal of Geophysical Research: Atmospheres*, 106(D21):27701–27710, 2001.

[18] R. Zhang, X. Tie, and D. W. Bond. Impacts of anthropogenic and natural nox sources over the us on tropospheric chemistry. *Proceedings of the National Academy of Sciences*, 100(4):1505–1509, 2003.

[19] P. J. Crutzen. The influence of nitrogen oxides on the atmospheric ozone content. *Quarterly Journal of the Royal Meteorological Society*, 96(408):320–325, 1970.

[20] M. Jang and R. M. Kamens. Atmospheric secondary aerosol formation by heterogeneous reactions of aldehydes in the presence of a sulfuric acid aerosol catalyst. *Environmental Science & Technology*, 35(24):4758–4766, 2001.

[21] T. M. Lillesand and R. W. Kiefer. Remote sensing and image interpretation. *Remote sensing and image interpretation.*, (Ed. 3), 1994.

[22] U. Platt and J. Stutz. *Differential Optical Absorption Spectroscopy*. Springer, 2008.

[23] A.-M. Blechschmidt, J. Arteta, A. Coman, L. Curier, H. Eskes, G. Foret, C. Gielen, F. Hendrick, V. Marécal, F. Meleux, J. Parmentier, E. Peters, G. Pinardi, A. J. M. Piters, M. Plu, A. Richter, A. Segers, M. Sofiev, A. M. Valdebenito, M. Van Roozendael, J. Vira, T. Vlemmix, and J. P. Burrows. Comparison of tropospheric no 2 columns from max-doas retrievals and regional air quality model simulations. *Atmospheric Chemistry and Physics*, 20(5):2795–2823, 2020.

[24] T. Wagner, C. Otten, K. Pfeilsticker, I. Pundt, and U. Platt. Doas moonlight observation of atmospheric no3 in the arctic winter. *Geophysical research letters*, 27(21):3441–3444, 2000.

[25] C. Fabry and H. Buisson. L'absorption de l'ultra-violet par l'ozone et la limite du spectre solaire. *Journal de Physique Théorique et Appliquée*, 3(1):196–206, 1913.

[26] D. Bortoli, G. Giovanelli, F. Ravegnani, I. Kostadinov, and A. Petritoli. Stratospheric nitrogen dioxide in the antarctic. *International Journal of Remote Sensing*, 26(16):3395–3412, 2005.

[27] J. P. Veefkind, J. F. de Haan, E. J. Brinksma, M. Kroon, and P. F. Levelt. Total ozone from the ozone monitoring instrument (omi) using the doas technique. *IEEE transactions on geoscience and remote sensing*, 44(5):1239–1244, 2006.

[28] M. M. Friedrich, C. Rivera, W. Stremme, Z. Ojeda, J. Arellano, A. Bezanilla, J. A. García-Reynoso, and M. Grutter. No 2 vertical profiles and column densities from max-doas measurements in mexico city. *Atmospheric Measurement Techniques*, 12(4):2545–2565, 2019.

[29] M. Bauwens, S. Compernolle, T. Stavrakou, J.-F. Müller, J. Van Gent, H. Eskes, P. F. Levelt, R. Van Der A, J. P. Veefkind, J. Vlietinck,

H. Yu, and C. Zehner. Impact of coronavirus outbreak on no2 pollution assessed using tropomi and omi observations. *Geophysical Research Letters*, 47(11):e2020GL087978, 2020.

[30] A. Schönhardt, P. Altube, K. Gerilowski, S. Krautwurst, J. Hartmann, A. C. Meier, A. Richter, and J. P. Burrows. A wide field-of-view imaging doas instrument for two-dimensional trace gas mapping from aircraft. *Atmospheric Measurement Techniques*, 8(12):5113–5131, 2015.

[31] G. Hönninger, H. Leser, O. Sebastian, and U. Platt. Ground-based measurements of halogen oxides at the hudson bay by active longpath doas and passive max-doas. *Geophysical research letters*, 31(4), 2004.

[32] Q. Hong, C. Liu, K. L. Chan, Q. Hu, Z. Xie, H. Liu, F. Si, and J. Liu. Ship-based max-doas measurements of tropospheric no 2, so 2, and hcho distribution along the yangtze river. *Atmospheric Chemistry and Physics*, 18(8):5931–5951, 2018.

[33] S. F. Schreier, A. Richter, and J. P. Burrows. Near-surface and path-averaged mixing ratios of no 2 derived from car doas zenith-sky and tower doas off-axis measurements in vienna: a case study. *Atmospheric Chemistry and Physics*, 19(9):5853–5879, 2019.

[34] S. Masieri, D. Bortoli, A. Petritoli, I. Kostadinov, M. Premuda, F. Ravegnani, C. Carnevale, E. Pisoni, M. Volta, and G. Giovanelli. Tropospheric profile of no2 over the po valley measured with scan doas spectrometer. In *Remote Sensing for Environmental Monitoring, GIS Applications, and Geology IX*, volume 7478, pages 657–666. SPIE, 2009.

[35] G. Kuhlmann, A. Hueni, A. Damm, and D. Brunner. An algorithm for in-flight spectral calibration of imaging spectrometers. *Remote Sensing*, 8(12), 2016.

[36] U. Platt, L. Marquard, T. Wagner, and D. Perner. Corrections for zenith scattered light doas. *Geophysical Research Letters*, 24(14):1759–1762, 1997.

[37] S. R. Aliwell, M. Van Roozendael, P. V. Johnston, A. Richter, T. Wagner, D. W. Arlander, J. P. Burrows, D. J. Fish, R. L. Jones, K. K. Trnkvist, J. C. Lambert, K. Pfeilsticker, and I. Pundt. Analysis for bro in zenith-sky spectra: An intercomparison exercise for analysis improvement. *Journal of Geophysical Research: Atmospheres*, 107(D14):ACH 10–1–ACH 10–20, 2002.

[38] D. W. Marquardt. An algorithm for least-squares estimation of nonlinear parameters. *Journal of the Society for Industrial and Applied Mathematics*, 11(2):431–441, 1963.

[39] J. F. Grainger and J. Ring. Anomalous fraunhofer line profiles. *Nature*, 193(4817):762–762, 1962.

[40] K. V. Chance and R. J. D. Spurr. Ring effect studies: Rayleigh scattering, including molecular parameters for rotational raman scattering, and the fraunhofer spectrum. *Applied optics*, 36(21):5224–5230, 1997.

[41] T. Wagner. *Satellite observations of atmospheric halogen oxides*. Mensch & Buch, 1999.

[42] K. Chance and R. L. Kurucz. An improved high-resolution solar reference spectrum for earth's atmosphere measurements in the ultraviolet, visible, and near infrared. *Journal of quantitative spectroscopy and radiative transfer*, 111(9):1289–1295, 2010.

[43] V. Rozanov, A. Rozanov, A. A. Kokhanovsky, and J. P. Burrows. Radiative transfer through terrestrial atmosphere and ocean: Software package sciatran. *Journal of Quantitative Spectroscopy and Radiative Transfer*, 133:13–71, 2014.

[44] T. Wagner, J. P. Burrows, T. Deutschmann, B. Dix, C. Von Friedeburg, U. Frieß, F. Hendrick, K. P. Heue, H. Irie, H. Iwabuchi, Y. Kanaya, J. Keller, C. A. McLinden, H. Oetjen, E. Palazzi, A. Petritoli, U. Platt, O. Postylyakov, J. Pukite, A. Richter, M. Van Roozendael, A. Rozanov, V. Rozanov, R. Sinreich, S. Sanghavi, and F. Wittrock. Comparison of box-air-mass-factors and radiances for multiple-axis differential optical absorption spectroscopy (max-doas) geometries calculated from different uv/visible radiative transfer models. *Atmospheric Chemistry and Physics*, 7(7):1809–1833, 2007.

[45] F. Hendrick, M. Van Roozendael, A. Kylling, A. Petritoli, A. Rozanov, S. Sanghavi, R. Schofield, C. Von Friedeburg, T. Wagner, F. Wittrock, D. Fonteyn, and M. De Maziere. Intercomparison exercise between different radiative transfer models used for the interpretation of ground-based zenith-sky and multi-axis doas observations. *Atmospheric Chemistry and Physics*, 6(1):93–108, 2006.

[46] T. Wagner, B. Dix, C. Friedeburg, U. Frieß, S. Sanghavi, R. Sinreich, and U. Platt. Max-doas o4 measurements: A new technique to derive

information on atmospheric aerosolsprinciples and information content. *Journal of Geophysical Research: Atmospheres*, 109(D22), 2004.

[47] M. Premuda, S. Masieri, D. Bortoli, I. Kostadinov, A. Petritoli, and G. Giovanelli. Evaluation of vessel emissions in a lagoon area with ground based multi axis doas measurements. *Atmospheric Environment*, 45(29):5212–5219, 2011.

[48] D. Bortoli, F. Ravegnani, G. Giovanelli, I. Kostadinov, A. Petritoli, S. Masieri, M. Premuda, H. T. Martins, and A. M. Silva. Ozone and nitrogen dioxide total columns and vertical distributions at the italian antarctic station during 1996-2008. In *Remote Sensing of Clouds and the Atmosphere XIV*, volume 7475, pages 416–426. SPIE, 2009.

[49] D. Bortoli, A. M. Silva, and G. Giovanelli. A new multipurpose uv-vis spectrometer for air quality monitoring and climatic studies. *International Journal of Remote Sensing*, 31(3):705–725, 2010.

[50] A. Donateo, M. Conte, F. M. Grasso, and D. Contini. Seasonal and diurnal behaviour of size segregated particles fluxes in a suburban area. *Atmospheric Environment*, 219:117052, 2019.

[51] A. Donateo, T. Lo Feudo, A. Marinoni, C. R. Calidonna, D. Contini, and P. Bonasoni. Long-term observations of aerosol optical properties at three gaw regional sites in the central mediterranean. *Atmospheric Research*, 241:104976, 2020.

[52] P. Cristofanelli, M. Busetto, F. Calzolari, I. Ammoscato, D. Gullì, A. Dinoi, C. R. Calidonna, D. Contini, D. Sferlazzo, T. Di Iorio, S. Piacentino, A. Marinoni, M. Maione, and P. Bonasoni. Investigation of reactive gases and methane variability in the coastal boundary layer of the central mediterranean basin. *Elementa: Science of the Anthropocene*, 5, 2017.

[53] A. C. Vandaele, C. Hermans, P. C. Simon, M. Carleer, R. Colin, S. Fally, M. F. Merienne, A. Jenouvrier, and B. Coquart. Measurements of the no2 absorption cross-section from 42 000 cm- 1 to 10 000 cm- 1 (238–1000 nm) at 220 k and 294 k. *Journal of Quantitative Spectroscopy and Radiative Transfer*, 59(3-5):171–184, 1998.

[54] K. Bogumil, J. Orphal, T. Homann, S. Voigt, P. Spietz, O. C. Fleischmann, A. Vogel, M. Hartmann, H. Kromminga, H. Bovensmann, J. Frerick, and J. P. Burrows. Measurements of molecular absorption

spectra with the sciamachy pre-flight model: instrument characterization and reference data for atmospheric remote-sensing in the 230–2380 nm region. *Journal of Photochemistry and Photobiology A: Chemistry*, 157(2-3):167–184, 2003.

[55] C. Hermans, A. C. Vandaele, M. Carleer, S. Fally, R. Colin, A. Jenouvrier, B. Coquart, and M. F. Mérienne. Absorption cross-sections of atmospheric constituents: No2, o2, and h2o. *Environmental Science and Pollution Research*, 6(3):151–158, 1999.

[56] E. Spinei, A. Cede, J. Herman, G. H. Mount, E. Eloranta, B. Morley, S. Baidar, B. Dix, I. Ortega, T. Koenig, and R. Volkamer. Ground-based direct-sun doas and airborne max-doas measurements of the collision-induced oxygen complex, o 2 o 2, absorption with significant pressure and temperature differences. *Atmospheric Measurement Techniques*, 8(2):793–809, 2015.

[57] K. F. Li, R. Khoury, T. J. Pongetti, S. P. Sander, F. P. Mills, and Y. L. Yung. Diurnal variability of stratospheric column no 2 measured using direct solar and lunar spectra over table mountain, california (34.38 n). *Atmospheric Measurement Techniques*, 14(12):7495–7510, 2021.

[58] R. Sussmann, W. Stremme, J. P. Burrows, A. Richter, W. Seiler, and M. Rettinger. Stratospheric and tropospheric no 2 variability on the diurnal and annual scale: a combined retrieval from envisat/sciamachy and solar ftir at the permanent ground-truthing facility zugspitze/garmisch. *Atmospheric Chemistry and Physics*, 5(10):2657–2677, 2005.

[59] I. Mavroidis and A. Chaloulakou. Long-term trends of primary and secondary no2 production in the athens area. variation of the no2/nox ratio. *Atmospheric environment*, 45(38):6872–6879, 2011.

[60] Y. Chen, D. Wang, A. ElAmraoui, H. Guo, and X. Ke. The effectiveness of traffic and production restrictions on urban air quality: a rare opportunity for investigation. *Journal of the Air & Waste Management Association*, (just-accepted), 2022.

[61] R. J. Dirksen, K. F. Boersma, H. J. Eskes, D. V. Ionov, E. J. Bucsela, P. F. Levelt, and H. M. Kelder. Evaluation of stratospheric no2 retrieved from the ozone monitoring instrument: Intercomparison, diurnal cycle, and trending. *Journal of Geophysical Research: Atmospheres*, 116(D8), 2011.

[62] N. A. Krotkov, L. N. Lamsal, E. A. Celarier, W. H. Swartz, S. V. Marchenko, E. J. Bucsela, K. L. Chan, M. Wenig, and M. Zara. The version 3 omi no 2 standard product. *Atmospheric Measurement Techniques*, 10(9):3133–3149, 2017.

[63] J. Van Geffen, K. F. Boersma, H. Eskes, M. Sneep, M. Ter Linden, M. Zara, and J. P. Veefkind. S5p tropomi no 2 slant column retrieval: Method, stability, uncertainties and comparisons with omi. *Atmospheric Measurement Techniques*, 13(3):1315–1335, 2020.

[64] T. Verhoelst, S. Compernolle, G. Pinardi, J. C. Lambert, H. J. Eskes, K. U. Eichmann, A. M. Fjæraa, J. Granville, S. Niemeijer, A. Cede, M. Tiefengraber, F. Hendrick, A. Pazmio, A. Bais, A. Bazureau, K. F. Boersma, K. Bognar, A. Dehn, S. Donner, A. Elokhov, M. Gebetsberger, F. Goutail, M. G. de la Mora, A. Gruzdev, M. Gratsea, G. H. Hansen, H. Irie, N. Jepsen, Y. Kanaya, D. Karagkiozidis, R. Kivi, K. Kreher, P. F. Levelt, C. Liu, M. Mller, M. N. Comas, A. J. M. Piters, J. P. Pommereau, T. Portafaix, C. Prados-Roman, O. Puentedura, R. Querel, J. Remmers, A. Richter, J. Rimmer, C. R. Crdenas, L. S. de Miguel, V. P. Sinyakov, W. Stremme, K. Strong, M. Van Roozendael, J. P. Veefkind, T. Wagner, F. Wittrock, M. Y. Gonzlez, and C. Zehner. Ground-based validation of the copernicus sentinel-5p tropomi no 2 measurements with the ndacc zsl-doas, max-doas and pandonia global networks. *Atmospheric Measurement Techniques*, 14(1):481–510, 2021.

[65] C. Wang, T. Wang, P. Wang, and V. Rakitin. Comparison and validation of tropomi and omi no2 observations over china. *Atmosphere*, 11(6):636, 2020.

[66] R. McPeters, M. Kroon, G. Labow, E. Brinksma, D. Balis, I. Petropavlovskikh, J. P. Veefkind, P. K. Bhartia, and P. F. Levelt. Validation of the aura ozone monitoring instrument total column ozone product. *Journal of Geophysical Research: Atmospheres*, 113(D15), 2008.

[67] K. Garane, M. E. Koukouli, T. Verhoelst, C. Lerot, K. P. Heue, V. Fioletov, D. Balis, A. Bais, A. Bazureau, A. Dehn, F. Goutail, J. Granville, D. Griffin, D. Hubert, A. Keppens, J. C. Lambert, D. Loyola, C. McLinden, A. Pazmino, J. P. Pommereau, A. Redondas, F. Romahn, P. Valks, M. Van Roozendael, J. Xu, C. Zehner, C. Zerefos, and W. Zimmer. Tropomi/s5p total ozone column data: global ground-based validation and consistency with other satellite missions. *Atmospheric Measurement Techniques*, 12(10):5263–5287, 2019.

[68] A. Heckel, A. Richter, T. Tarsu, F. Wittrock, C. Hak, I. Pundt, W. Junkermann, and J. P. Burrows. Max-doas measurements of formaldehyde in the po-valley. *Atmospheric Chemistry and Physics*, 5(4):909–918, 2005.

[69] S. Masieri, A. Petritoli, I. Kostadinov, D. Bortoli, M. Premuda, F. Ravegnani, and G. Giovanelli. Vertical profiles of pollutant gases measured with passive doas in the po valley devoted to satellite and chemical model data comparison. In *EGU General Assembly Conference Abstracts*, page 7888, 2009.

[70] A. M. Iannarelli, A. Di Bernardino, S. Casadio, C. Bassani, M. Cacciani, M. Campanelli, G. Casasanta, E. Cadau, H. Diémoz, G. Mevi, A. M. Siani, M. Cardaci, A. Dehn, and P. Goryl. The boundary layer air quality-analysis using network of instruments (baqunin) supersite for atmospheric research and satellite validation over rome area. *Bulletin of the American Meteorological Society*, 103(2):E599–E618, 2022.

[71] E. Spinei, A. Cede, W. H. Swartz, J. Herman, and G. H. Mount. The use of no 2 absorption cross section temperature sensitivity to derive no 2 profile temperature and stratospheric–tropospheric column partitioning from visible direct-sun doas measurements. *Atmospheric Measurement Techniques*, 7(12):4299–4316, 2014.

[72] A. Cede. *Manual for Blick Software Suite 1.7*, december 2019, issue 1, luftblick og, mutters, austria, version 11, available at: `https://www.pandonia-global-network.org/wp-content/uploads/2019/11/BlickSoftwareSuite_Manual_v1-7.pdf` (accessed on 22 november 2021) edition.

[73] D. Loyola, R. Lutz, A. Argyrouli, and R. Spurr. S5p/tropomi atbd cloud products. *German Aerospace Center*, 2020.

[74] H. Eskes, J. van Geffen, F. Boersma, K. U. Eichmann, A. Apituley, M. Pedergnana, M. Sneep, J. P. Veefkind, and D. Loyola. Sentinel-5 precursor/tropomi level 2 product user manual nitrogendioxide. Technical report, 2021. S5P-KNMI-L2-0021-MA, Koninklijk Nederlands Meteorologisch Instituut (KNMI), CI-7570-PUM, issue 4.0.2, `https://sentinels.copernicus.eu/documents/247904/2474726/Sentinel-5P-Level-2-Product-User-Manual-Nitrogen-Dioxide.pdf/ad25ea4c-3a9a-3067-0d1c-aaa56eb1746b?t=1637071405160` (accessed on 05 April 2022).

[75] N. L. Lamsal, A. K. Nickolay, V. M. Sergey, J. Joanna, O. Luke, V. Alexander, F. Bradford, Q. Wenhan, Y. Eun-Su, F. Zachary, C. Sungyeon, L. Peter, and D. Haffner. Omi/aura no2 tropospheric, stratospheric fff total columns minds 1-orbit l2 swath 13 km x 24 km. nasa goddard space flight center, goddard earth sciences data and information services center (ges disc) `https://disc.gsfc.nasa.gov/datasets/OMI_MINDS_NO2_1/summary` (accessed on 05 april 2022). Technical report, 2020.

[76] H. Wang, A. H. Souri, A. G. González, X. Liu, and K. Chance. Ozone monitoring instrument (omi) total column water vapor version 4 validation and applications. *Atmospheric Measurement Techniques*, 12(9):5183–5199, 2019.

[77] J.-C. Lambert, S. Compernolle, K.-U. Eichmann, M. de Graaf, D. Hubert, A. Keppens, Q. Kleipool, B. Langerock, M. Sha, T. Verhoelst, T. Wagner, C. Ahn, A. Argyrouli, D. Balis, K. Chan, I. De Smedt, H. Eskes, A. Fjraa, K. Garane, J. Gleason, F. Goutail, J. Granville, P. Hedelt, K.-P. Heue, G. Jaross, M. Koukouli, J. Landgraf, R. Lutz, S. Nanda, S. Niemeijer, A. Pazmio, G. Pinardi, J.-P. Pommereau, A. Richter, N. Rozemeijer, M. Sneep, D. Stein Zweers, N. Theys, G. Tilstra, O. Torres, P. Valks, J. van Geffen, C. Vigouroux, P. Wang, and M. Weber. Quarterly validation report of the copernicus sentinel-5 precursor operational data products #12: April 2018 september 2021. s5p mpc routine operations consolidated validation report series. version 12.01.00. Technical report, 2021.

[78] T. Bösch, V. Rozanov, A. Richter, E. Peters, A. Rozanov, F. Wittrock, A. Merlaud, J. Lampel, S. Schmitt, M. de Haij, S. Berkhout, B. Henzing, A. Apituley, M. den Hoed, J. Vonk, M. Tiefengraber, M. Müller, and J. P. Burrows. Boreas – a new max-doas profile retrieval algorithm for aerosols and trace gases. *Atmospheric Measurement Techniques*, 11(12):6833–6859, 2018.

[79] J.-L. Tirpitz, U. Frieß, F. Hendrick, C. Alberti, M. Allaart, A. Apituley, A. Bais, S. Beirle, S. Berkhout, K. Bognar, T. Bösch, I. Bruchkouski, A. Cede, K. L. Chan, M. den Hoed, S. Donner, T. Drosoglou, C. Fayt, M. M. Friedrich, A. Frumau, L. Gast, C. Gielen, L. Gomez-Martín, N. Hao, A. Hensen, B. Henzing, C. Hermans, J. Jin, K. Kreher, J. Kuhn, J. Lampel, A. Li, C. Liu, H. Liu, J. Ma, A. Merlaud, E. Peters, G. Pinardi, A. Piters, U. Platt, O. Puentedura, A. Richter, S. Schmitt,

E. Spinei, D. Stein Zweers, K. Strong, D. Swart, F. Tack, M. Tiefengraber, R. van der Hoff, M. van Roozendael, T. Vlemmix, J. Vonk, T. Wagner, Y. Wang, Z. Wang, M. Wenig, M. Wiegner, F. Wittrock, P. Xie, C. Xing, J. Xu, M. Yela, C. Zhang, and X. Zhao. Intercomparison of max-doas vertical profile retrieval algorithms: studies on field data from the cindi-2 campaign. *Atmospheric Measurement Techniques*, 14(1):1–35, 2021.

[80] C. D. Rodgers. *Inverse methods for atmospheric sounding: theory and practice*, volume 2. World scientific, 2000.

[81] J. E. Williams, K. F. Boersma, P. Le Sager, and W. W. Verstraeten. The high-resolution version of tm5-mp for optimized satellite retrievals: description and validation. *Geoscientific Model Development*, 10(2):721–750, 2017.

[82] E. Dimitropoulou, F. Hendrick, G. Pinardi, M. M. Friedrich, A. Merlaud, F. Tack, H. De Longueville, C. Fayt, C. Hermans, Q. Laffineur, F. Fierens, and M. Van Roozendael. Validation of tropomi tropospheric no 2 columns using dual-scan multi-axis differential optical absorption spectroscopy (max-doas) measurements in uccle, brussels. *Atmospheric Measurement Techniques*, 13(10):5165–5191, 2020.

[83] H. J. Eskes and K. F. Boersma. Averaging kernels for doas total-column satellite retrievals. *Atmospheric Chemistry and Physics*, 3(5):1285–1291, 2003.